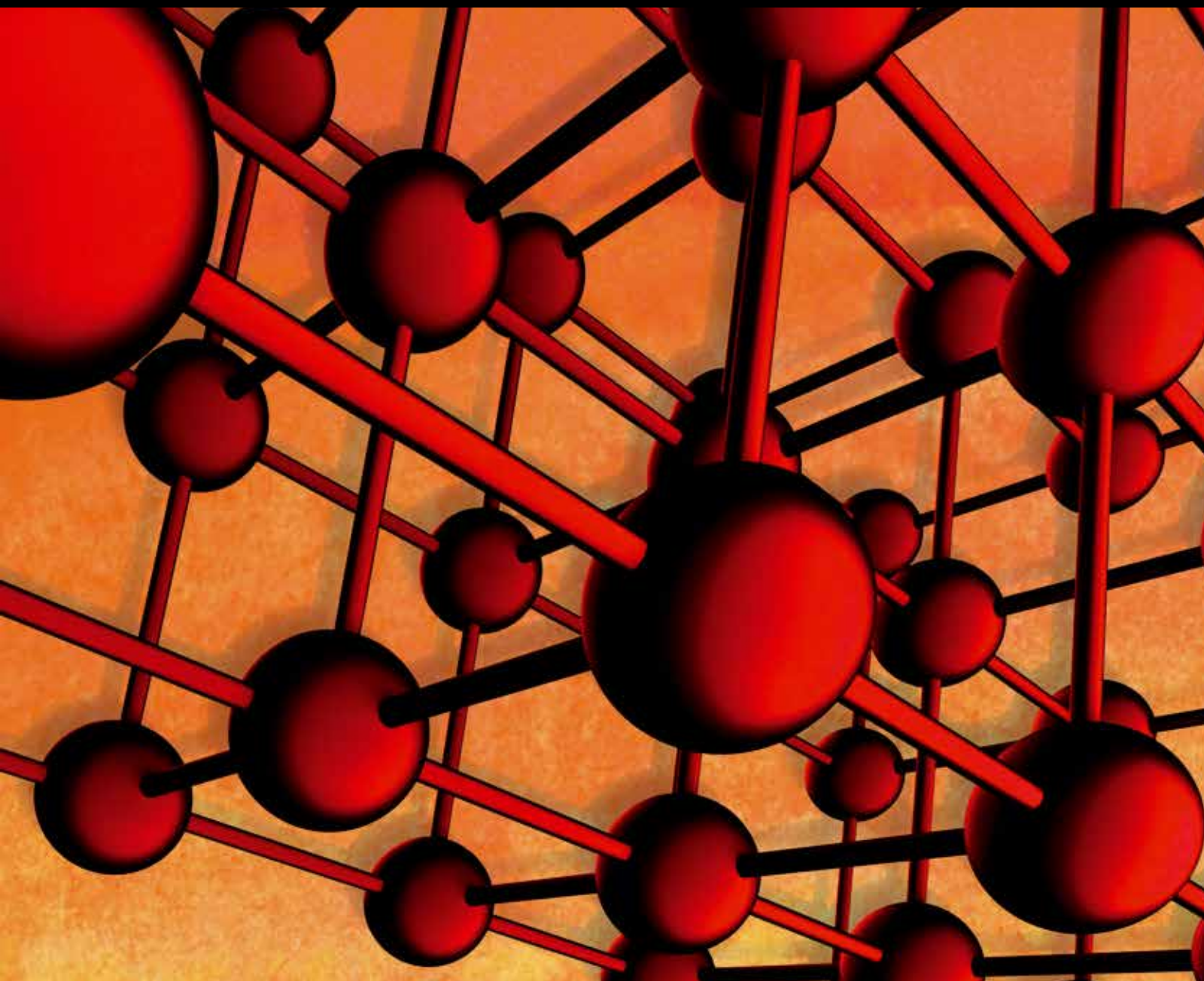


Advances in Materials Science and Engineering

# Nano, Ceramic, and Metallic Materials for Energy Application

Guest Editors: Ching-Song Jwo, Ho Chang, Hong-Ming Lin, Teobald Kupka,  
and Wen-An Chiou





---

# **Nano, Ceramic, and Metallic Materials for Energy Application**

Advances in Materials Science and Engineering

---

## **Nano, Ceramic, and Metallic Materials for Energy Application**

Guest Editors: Ching-Song Jwo, Ho Chang, Hong-Ming Lin,  
Teobald Kupka, and Wen-An Chiou



---

Copyright © 2014 Hindawi Publishing Corporation. All rights reserved.

This is a special issue published in “Advances in Materials Science and Engineering.” All articles are open access articles distributed under the Creative Commons Attribution License, which permits unrestricted use, distribution, and reproduction in any medium, provided the original work is properly cited.

## Editorial Board

K. G. Anthymidis, Greece  
Robert S. Averbach, USA  
Amit Bandyopadhyay, USA  
Zoe Barber, UK  
Yucel Birol, Turkey  
Susmita Bose, USA  
Steve Bull, UK  
Peter Chang, Canada  
Daolun Chen, Canada  
Manish U. Chhowalla, USA  
S. Chinnappanadar, India  
Jie Dai, Singapore  
Chapal K. Das, India  
J. Paulo Davim, Portugal  
Seshu B. Desu, USA  
Yong Ding, USA  
Wei Feng, China  
Sergi Gallego, Spain  
Lian Gao, China  
Hiroki Habazaki, Japan  
Richard Hennig, USA  
Dachamir Hotza, Brazil  
Chun-Hway Hsueh, Taiwan  
Shyh-Chin Huang, Taiwan  
Rui Huang, USA  
Wei Huang, China  
Baibiao Huang, China  
Jacques Huot, Canada  
Jae-Ho Kim, Korea  
Jaehwan Kim, Korea  
Sridhar Komarneni, USA  
Hongchao Kou, China  
Prashant Kumta, USA  
Jui-Yang Lai, Taiwan  
Pavel Lejcek, Czech Republic

Markku Leskela, Finland  
Bin Li, China  
Feng Li, China  
Ying Li, USA  
Hai Lin, China  
Yuanhua Lin, China  
Zhimin Liu, China  
Ying Liu, USA  
Yuan Liu, China  
Gang Liu, China  
Tao Liu, China  
Jun Liu, China  
Meilin Liu, Georgia  
Wei Liu, France  
Yunqi Liu, China  
Maria A. Loi, The Netherlands  
Hai Lu, China  
Peter Majewski, Australia  
Shuichi Miyazaki, Japan  
Hossein Moayed, Malaysia  
Paul Munroe, Australia  
Ali Nazari, Iran  
Luigi Nicolais, Italy  
Tsutomu Ohzuku, Japan  
Xiaoqing Pan, USA  
G. Ramanath, USA  
Raju V. Ramanujan, Singapore  
Manijeh Razeghi, USA  
M. Sapuan Salit, Malaysia  
Jainagesh A. Sekhar, USA  
Jiangbo Sha, China  
Liyuan Sheng, China  
You Song, China  
Aloysius Soon, Korea  
Charles C. Sorrell, Australia

Steven L. Suib, USA  
Sam-Shajing Sun, USA  
Weihua Tang, China  
Somchai Thongtem, Thailand  
Achim Trampert, Germany  
Vladimir Tsukruk, USA  
Krystyn Van Vliet, USA  
Rui Vilar, Portugal  
Min Wang, China  
Hao Wang, China  
Rui. WANG, China  
Rong Wang, USA  
Qiang Wang, China  
Lu Wei, China  
Jörg M K Wieszorek, USA  
Wei Wu, USA  
Gongnan Xie, China  
Aiguo Xu, China  
Hemmige S. Yathirajan, India  
Jianqiao Ye, UK  
Wenbin Yi, China  
Jinghuai Zhang, China  
Jing Zhang, China  
Li Zhang, China  
Tao Zhang, China  
Bin Zhang, China  
Jian Zhang, Singapore  
Jun Zhang, China  
Yufeng Zhang, China  
Kai Zhang, China  
Kai Zhang, China  
Rui Zhang, China  
Ming-Xing Zhang, Australia  
Wei Zhou, China

**Nano, Ceramic, and Metallic Materials for Energy Application**, Ching-Song Jwo, Ho Chang, Hong-Ming Lin, Teobald Kupka, and Wen-An Chiou  
Volume 2014, Article ID 367263, 2 pages

**Analysis of Heat Transfer Mechanism for Shelf Vacuum Freeze-Drying Equipment**, Hong-Ping Cheng, Chin-Chi Cheng, and Shian-Min Tsai  
Volume 2014, Article ID 515180, 7 pages

**Effects of Surface Modification of Nanodiamond Particles for Nucleation Enhancement during Its Film Growth by Microwave Plasma Jet Chemical Vapour Deposition Technique**, Chii-Ruey Lin, Da-Hua Wei, Minh-Khoa BenDao, Hong-Ming Chang, Wei-En Chen, and Jen-Ai Lee  
Volume 2014, Article ID 937159, 5 pages

**Synthesis and Characterization of SiO<sub>2</sub> Nanoparticles and Their Efficacy in Chemical Mechanical Polishing Steel Substrate**, M. J. Kao, F. C. Hsu, and D. X. Peng  
Volume 2014, Article ID 691967, 8 pages

**Novel Method for Floating Synthesizing Heavy Metal Particles as Flowing Anode of Zinc-Air Fuel Cell**, Chen Yang Wu, Kuohsiu David Huang, and Horng Yi Tang  
Volume 2014, Article ID 615391, 7 pages

**Effect of Polarization Fatigue on Harvesting Energy Using Pyroelectric Materials**, Saber Mohammadi  
Volume 2014, Article ID 913817, 4 pages

**The Photocatalytic Reduction of Hexavalent Chromium by Controllable Mesoporous Anatase TiO<sub>2</sub> Nanoparticles**, Vorrada Loryuenyong, Natnapin Jarunsak, Thirawich Chuangchai, and Achanai Buasri  
Volume 2014, Article ID 348427, 8 pages

**Performance Analysis of Al<sub>2</sub>O<sub>3</sub>/Water Nanofluid with Cationic Chitosan Dispersant**, T. Y. Chen, H. P. Cho, C. S. Jwo, and L. Y. Jeng  
Volume 2013, Article ID 686409, 8 pages

**Pool Boiling of Micro-/Nanoparticles Modified Aluminum Surface**, Chin-Ting Yang and Chia-Cheng Yu  
Volume 2013, Article ID 258241, 6 pages

**Multifunction of Ni/Ag Nanocompound Fluid**, Mu-Jung Kao  
Volume 2013, Article ID 872587, 4 pages

**Defect Study of MgO-CaO Material Doped with CeO<sub>2</sub>**, Han Zhang, Huizhong Zhao, Jinfeng Chen, Jingjie Li, Jun Yu, and Jianhua Nie  
Volume 2013, Article ID 673786, 5 pages

## Editorial

# Nano, Ceramic, and Metallic Materials for Energy Application

**Ching-Song Jwo,<sup>1</sup> Ho Chang,<sup>2</sup> Hong-Ming Lin,<sup>3</sup> Teobald Kupka,<sup>4</sup> and Wen-An Chiou<sup>5</sup>**

<sup>1</sup> Emission Reduction & Energy Conservation Center, National Taipei University of Technology, No. 1, Section 3, Chung-hsiao East Road, Taipei 10608, Taiwan

<sup>2</sup> Graduate Institute of Manufacturing Technology, National Taipei University of Technology, No. 1, Section 3, Chung-hsiao East Road, Taipei 10608, Taiwan

<sup>3</sup> Department of Materials Engineering, Tatung University, No. 40, Section 3, Zhongshan N. Road, Zhongshan District, Taipei City 104, Taiwan

<sup>4</sup> Department of Physical Chemistry and Molecular Modeling, Faculty of Chemistry, University of Opole, Oleska 48, 45-052 Opole, Poland

<sup>5</sup> Center for Nanoscscopy and Nanoanalysis, University of Maryland, 1234 Jeong H. Kim Building, College Park, MD 20742-2831, USA

Correspondence should be addressed to Ching-Song Jwo; frankjwo@ntut.edu.tw

Received 18 March 2014; Accepted 18 March 2014; Published 15 May 2014

Copyright © 2014 Ching-Song Jwo et al. This is an open access article distributed under the Creative Commons Attribution License, which permits unrestricted use, distribution, and reproduction in any medium, provided the original work is properly cited.

Scientists and engineers are interested in comprehending and improving the physical and chemical properties performance of nano-, ceramic, and metallic materials for their applications. This special issue compiles 9 exciting manuscripts, most of which are using nanoparticles and functional nanofluids to improve the performance and efficiency of engineering technology and applications.

The modification of nanoparticles synthesized approaches and applications between multiple engineering technology is addressed in four manuscripts. One interesting topic of nanoparticles in chemical mechanical polishing (CMP) technology to improve the efficacy of polishing steel substrate is addressed by M. J. kao et al. A nanopowder of SiO<sub>2</sub> was compounded into polishing slurry for the CMP of steel substrate. Their results indicated the roughness of the steel substrate strongly depends on the size of the abrasive, and the surface roughness decreases as the abrasive size declines. The paper by C. Y. Wu et al. provided a new approach for synthesized centrally hollow microspheres of zinc and employed the permanent floating of zinc particles as flowing anode of zinc-air fuel cell. Their paper provides a detailed performance test of this novel zinc-air fuel cell. V. Loryuonyong et al. described the method to produce titania (TiO<sub>2</sub>) and controlled the porosity and particle size of TiO<sub>2</sub> nanoparticles with different quantities of activated

carbon. Their results showed that the specific surface area of TiO<sub>2</sub> is increased with increasing activated carbon content. Meanwhile, the photocatalytic activity of porous TiO<sub>2</sub> and its reduction efficiency are determined by hexavalent chromium (Cr<sup>6+</sup>) reduction rate and optimized ultraviolet illumination, respectively. The paper by H. Zhang et al. studied the effect of CeO<sub>2</sub> powders on the defect of MgO-CaO refractories. Their results showed the addition of CeO<sub>2</sub> increased the lattice constant of CaO, and the bulk density of the samples increased while apparent porosity decreased.

Three of the manuscripts dealing with the ceramics materials, nanoparticles, and numerical stimulation for the energy-savings performance and efficacy are addressed. Enhancing the pool boiling heat transfer efficiency is one of the important methods to solve the high power density system's cooling problems. Since the bubble formation and particle size are two factors related to surface wettability, C.-T. Yang and C.-C. Yu deal with the issues with modified aluminum surface with micro/nanoparticles. Vacuum freeze-drying technology is applicable to the process of high heat-sensitive products. The uniformity and efficiency of heat transfer fluid temperature in shelf are critical concerning improving the quality of high heat-sensitive products. The paper by H.-p. Cheng et al. addressed the issues with the three-dimensional numerical stimulation of the shelf vacuum

freeze-drying process. The influences of different inlet and outlet positions for shelves on the uniformity of the flow rate and temperature were discussed. Meanwhile, the impacts on the temperature gradient of shelves after heat exchange of different flow rates and low temperature materials are well explored in great depth. The paper by S. Mohammadi explores the phenomenon of polarization fatigue in ferroelectric materials and measures the effect of this phenomenon using PZN-4.5PT single crystal.

Last, two manuscripts addressed the nanofluids applications. M.-J. Kao proposed and developed an arc-submerged nanoparticle synthesis system (ASNSS) for fabricating Ni/Ag nanocompound fluid. The detailed properties analysis of the nanocompound fluid was provided. The experiment results showed that the Ni/Ag nanofluid not only preserves the magnetic character of the nickel and the ability of silver to absorb visible light but also enhances the thermal conductivity. The paper by T. Y. Chen et al. described the effect of the cationic chitosan dispersant on the thermal conductivity, dispersion, and suspension of 15 nm  $\text{Al}_2\text{O}_3$ /water nanofluid. The cationic chitosan dispersant was shown to improve the dispersion and suspension of nanofluid. A better performance of thermal conductivity was found when compared with nanofluid when adding cationic chitosan dispersant.

By compiling these papers, we hope to enrich our readers and researchers with respect to these exciting, insightful observations of nano-, ceramic, and metallic materials applications on various engineering. We hope that this special issue would attract major attention of the peers.

## **Acknowledgments**

We would like to express our appreciation to all the authors and reviewers for their great support to make this special issue possible.

*Ching-Song Jwo  
Ho Chang  
Hong-Ming Lin  
Teobald Kupka  
Wen-An Chiou*

## Research Article

# Analysis of Heat Transfer Mechanism for Shelf Vacuum Freeze-Drying Equipment

**Hong-Ping Cheng, Chin-Chi Cheng, and Shian-Min Tsai**

*Department of Energy and Refrigerating Air-Conditioning Engineering, National Taipei University of Technology, Taipei City 10608, Taiwan*

Correspondence should be addressed to Shian-Min Tsai; [simon884031@yahoo.com.tw](mailto:simon884031@yahoo.com.tw)

Received 10 September 2013; Revised 8 February 2014; Accepted 25 February 2014; Published 14 May 2014

Academic Editor: Ching-Song Jwo

Copyright © 2014 Hong-Ping Cheng et al. This is an open access article distributed under the Creative Commons Attribution License, which permits unrestricted use, distribution, and reproduction in any medium, provided the original work is properly cited.

Vacuum freeze-drying technology is applicable to the process of high heat-sensitive products. Due to the long drying period and extremely low processing temperature and pressure, the uniform and efficiency of heat transfer fluid temperature in shelf are critical for product quality. Therefore, in this study, the commercial computer fluid dynamics (CFD) software, FLUENT, was utilized for three-dimension numerical simulation of the shelf vacuum freeze-drying process. The influences of different inlet and outlet positions for shelves on the uniformity of the flow rate and temperature were discussed. Moreover, it explored the impacts on the temperature gradient of shelves after heat exchange of different flow rates and low temperature materials. In order to reduce the developing time and optimize the design, the various secondary refrigerants in different plies of shelves were investigated. According to the effect of heat exchange between different flow rates and low temperature layer material shelves on the temperature gradient of shelves surface, the minimum temperature gradient was 20 L/min, and the maximum was 2.5 L/min.

## 1. Introduction

Vacuum freeze-drying technology is widely used for manufacturing pharmaceuticals. The requirements of this technology are process optimization and long-term storage stability. There are three stages in the complete vacuum freeze-drying process, such as freezing, primary drying, and secondary drying. Most of the water is frozen to the ice during the freezing stage, and then the ice is removed by sublimation during the primary drying stage. During the secondary drying stage, the temperature is usually elevated to remove the residual water of the products [1, 2]. Due to the extremely rigor conditions of vacuum freeze-drying process, such as low temperature, high vacuum, and long processing period, the process stability and efficiency would be crucial for product quality.

In the vacuum freeze-drying process, before all the ice is removed from the product, increasing the shelf temperature into the secondary drying would likely cause collapse or eutectic melt of the products. Therefore, the controllability of the temperature of the heat-transfer fluid in the shelf

is very important for product quality during the freeze-drying process. Many studies would like to find out how the temperature of the heat-transfer fluid in the shelf affected the freeze-drying process. Liapis and Bruttini [3] constructed the operational control policies by the presented exergy expressions to minimize the irreversibilities occurring in a freeze-drying system and enhance the efficiency of energy utilization in lyophilization. Patel et al. [4] measured the temperature of 5% mannitol and 5% sucrose by thermocouple to determine the setting shelf temperature and understood the time of primary drying end by product temperature. Gieseler et al. [5] investigated the better drying parameters by measuring the total amount of removed water from the product of pure water and a 5% (w/w) mannitol at different pressure and shelf temperature settings, performed in both laboratory and pilot scale freeze dryers. For the pharmaceutical and protein formulations, the collapse temperature and the thermal transition were utilized to find out the optimal heat-transfer fluid temperature of shelf and chamber pressure settings required to achieve the target product temperature [6, 7]. For food products, Sablani and Rahman [8] indicated

that the heat-transfer temperature of shelf maintained in  $-45\sim-15^{\circ}\text{C}$  during primary drying process would result in the best quality of drying abalone, potato, and brown dates.

From the above literatures, one can see that the heat-transfer fluid temperature of shelf is one of the most important factors in drying process. Therefore, some technologies, such as manometric temperature measurement (MTM), had been used to determine the optimal shelf temperature, and the expert system was utilized to estimate the required shelf temperature for maintaining product temperature [9, 10]. In addition, some studies employed the finite element analysis for 2D simulation of sublimation and heat transfer [11, 12], discussing the contact heat transfer between shelf and glass bottle [13, 14] and investigating the temperature distribution between glass bottle and product during the drying cycle [15, 16]. However, the rare literature discussed the flow pattern of fluid inside shelves, design of shelves, and effect of fluid flow and temperature.

The objective of this paper is to investigate the heat transfer rate of the fluid in shelf by using CFD method. Several factors, such as the location of inlet and outlet of the fluid in shelf and mass flow rate, are also discussed in order to improve the efficiency of shelf for the laboratory scale vacuum freeze-drying system.

## 2. Operating Conditions

In this paper, a commercial CFD software, FLUENT, was adopted to simulate all heat transferring processes in the heat exchanger, in order to optimize the design. Shelf is one of the most important devices in the vacuum freeze-drying system, because of its capability to heat and cool the products. Therefore, several designs and their operating procedures will be investigated in the study. The efficient shelf is able to reduce the required energy of vacuum freeze-drying equipment during drying process and uplifting the quality of dried product. The 50% ethylene glycol solution flowing into the shelf served as the secondary refrigerant. Figure 1 shows the schematic drawing of the freeze-drying system, including (a) vacuum chamber, (b) shelf, (c) cold trap, (d) vacuum pump, (e) heat exchanger, (f) condensers, (g) expansion valve, and (h) compressors.

This study would focus on numerical simulation of the flow field and heat-transfer fluid properties conducted for internal flow channel of shelves, including different inlet positions and inlet velocities. The simulation included five cases, as shown in Figure 2 for the detail schematic drawings. Case 1 is the geometric shape of the shelves of vacuum freeze-drying machine. The inlet position is at the top, and the outlet position is at the bottom, as shown in Figure 2(a). For Case 2, the inlet position is at the bottom, and the outlet position is at the top, as shown in Figure 2(b). For Case 3, both the inlet and outlet are at the bottom, as shown in Figure 2(c). For Case 4, both the inlet and outlet are at the top, as shown in Figure 2(d). For Case 5, the increased part is at the bottom, and inlet and outlet are both at the bottom, as shown in Figure 2(e).

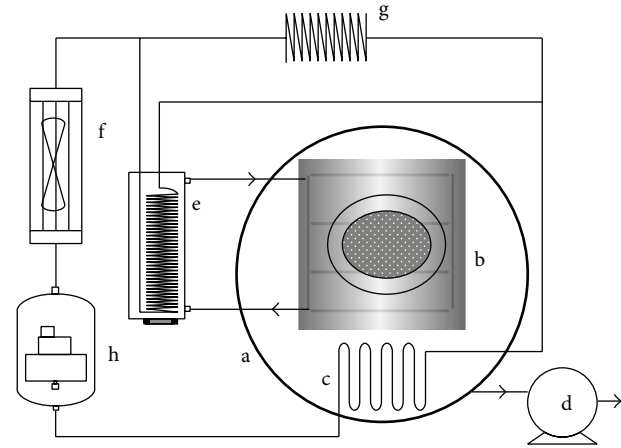


FIGURE 1: Schematic drawing of the freeze-drying system.

**2.1. Boundary Conditions.** A CFD software, FLUENT, was adopted to simulate the heat exchanging process. Several assumptions during the simulation were made as follows: (1) steady-state flow field; (2) the viscous model uses Laminar; (3) the pressure-velocity coupling uses Simple; (4) the convection-diffusion term uses First Order Upwind; (5) the material is maintained at a constant temperature of 233 K in the computational process.

The numbers of grids in Case 1 to Case 4 were 1304471 and that in Case 5 were 1308602. The computing range under hypothetical simulation conditions covered one inlet, one outlet, and liquid entering into shelves, while others were solid boundaries. The pipes through the shelves were set as square pipes after hydraulic diameter calculation, so that grids in GAMBIT were used as a hex map. The grids were 1 mm per unit in X-direction after grid testing, 2 mm per unit in Y-direction, and 2 mm per unit in Z-direction, as shown in Figure 3. The three-dimensional graphics of shelves and shelf flow channel as shown in Figure 3(a) and the grids exterior were shown in Figure 3(b) to Figure 3(d).

The boundary conditions of Cases 1 to 5 are as follows. (1) Inlet and outlet boundaries: the boundary condition of inlet is set as velocity inlet; the inlet velocities are 2.5 L/min, 5 L/min, 10 L/min, and 20 L/min, respectively; the inlet temperature was fixed at 253 K; the outlet boundary was set as outflow; (2) heat transfer fluid entering shelves: the fluid boundary condition settings adopt a 50% ethylene glycol solution; the fluid properties had density of  $1085\text{ kg/m}^3$ , specific heat of  $3490\text{ J/kg}\cdot\text{K}$ , heat transfer coefficient of  $0.42\text{ w/m}\cdot\text{k}$ , and viscosity coefficient of  $0.029\text{ kg/m}\cdot\text{s}$ ; (3) solid boundary: this solid boundary was set as a wall; the material was steel, and the wall surface was set as heat flux; it was assumed that the top contacts low temperature material was at a preset temperature of 233 K.

**2.2. Method of Analysis.** For simulating the freeze-drying process of heat transfer fluid in shelf, determination of flow patterns is the first step. Reynolds number is usually adopted

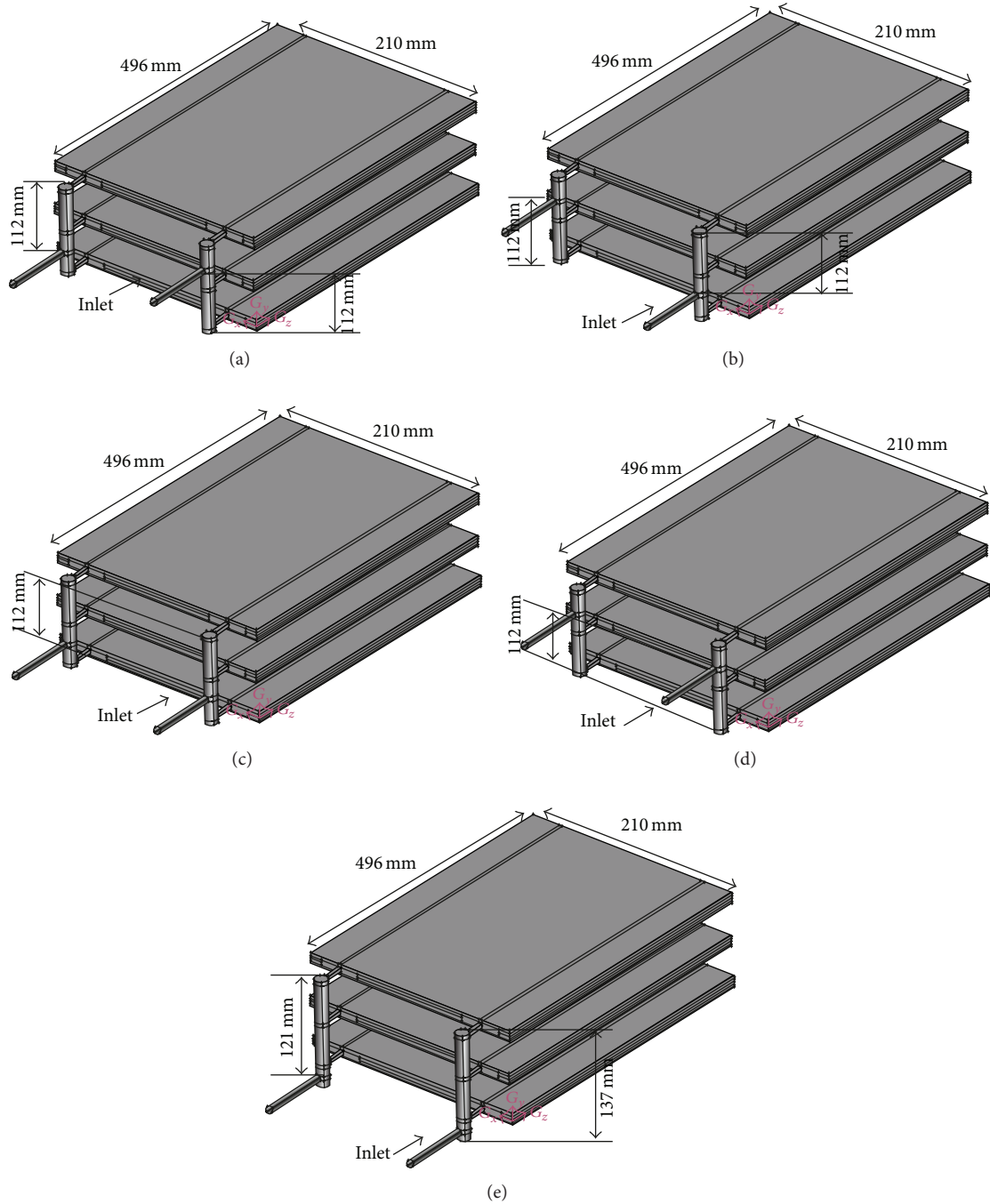


FIGURE 2: Geometric shapes of (a) Case 1, (b) Case 2, (c) Case 3, (d) Case 4, and (e) Case 5.

to predict the flow patterns in different flow situations. It can be calculated as

$$Re = \frac{\rho V d_i}{\mu}, \tag{1}$$

where  $\rho$  is the density ( $\text{kg/m}^3$ ),  $V$  is the average velocity ( $\text{m/s}$ ),  $d_i$  is the hydraulic diameter ( $\text{m}$ ), and  $\mu$  is the viscosity ( $\text{kg/m-s}$ ).

In this study, the heat transfer fluid in the shelf utilized ethylene glycol solution, with a concentration ratio of 50%. Its thermodynamic properties are  $\rho = 1089 \text{ kg/m}^3$ ,  $d_i = 7.92 \text{ mm}$ , and  $\mu = 0.0265 \text{ kg/m-s}$ . These thermodynamic properties varied with environmental temperature, according to the source of the thermodynamic properties of NIST (National Institute of Standards and Technology). The Reynolds number of the heat transfer fluid in the shelf can be calculated according to (1). The calculated Reynolds number

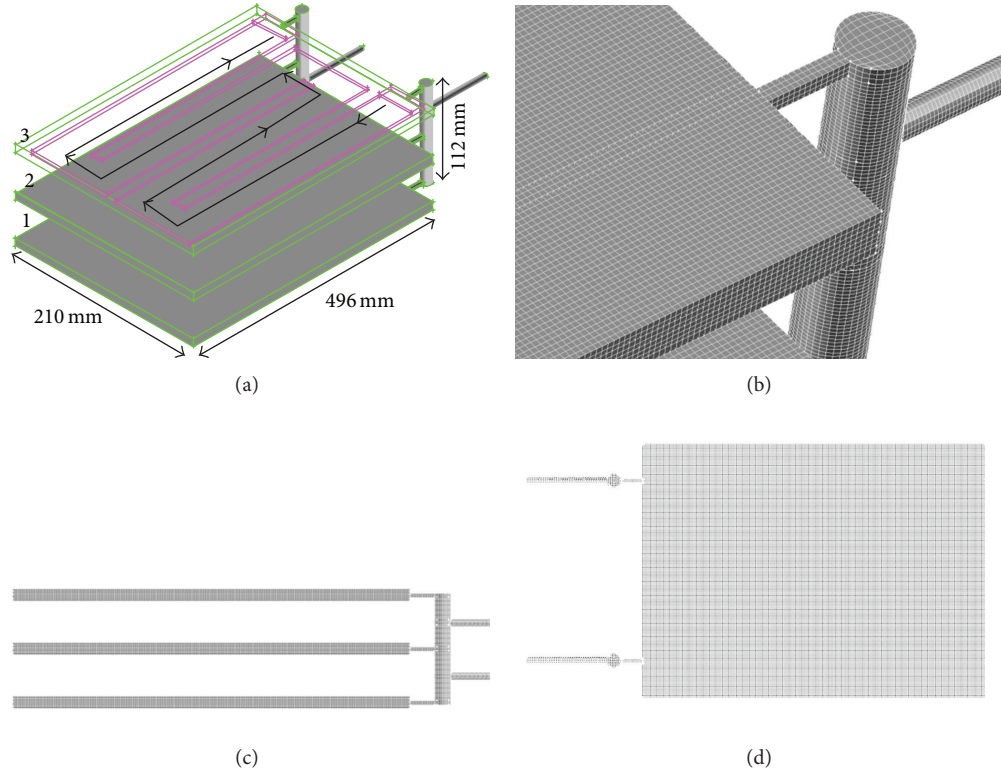


FIGURE 3: Three-dimensional graphics of shelves and shelf flow channel: (a) overall dimensions of shelves and flow channel structure; (b) local grid structure distribution; (c) side view of overall grid structure distribution; (d) top view of overall grid structure distribution.

was 12, which is less than 2300. According to the calculated Reynolds number, the inlet flow is decided as the laminar. Thus, the CFD simulation for all the cases was according to the laminar model.

**2.3. Heat Transfer Rate.** This study would focus on the heat-transfer fluid in shelf and heat exchange with freeze products. Therefore, the heat transfer rate was calculated as

$$Q_c = \bar{h}_c A_s (T_s - T_A), \quad (2)$$

where  $Q_c$  is the heat transfer rate,  $\bar{h}_c$  is convective heat transfer coefficient,  $A_s$  is the body surface area,  $T_s$  is the body wall surface temperature, and  $T_A$  is the ambient temperature.

For calculating  $Q_c$ , the Nusselt number was calculated first. It can be calculated as

$$Pr = \frac{C_p \mu}{k}, \quad (3)$$

where  $Pr$  is the Prandtl number,  $C_p$  is the specific heat (j/kg-k),  $\mu$  is the viscosity (kg/m-s), and  $k$  is the thermal conductivity (w/m-k). The Prandtl number was located in the range of  $0.48 < Pr < 16700$ .

The laminar Nusselt number equation is used for calculating  $\bar{h}_c$  as follows:

$$Nu = \frac{\bar{h}_c D}{k} = 1.86 \left( \frac{VD\rho}{\mu} \right)^{1/3} \left( \frac{C_p \mu}{k} \right)^{1/3} \left( \frac{D}{L} \right)^{1/3} \left( \frac{\mu}{\mu_w} \right), \quad (4)$$

where  $Nu$  is the Nusselt number,  $\bar{h}_c$  is the convective heat transfer coefficient ( $W/m^2-K$ ),  $D$  is the hydraulic diameter (m),  $k$  is the thermal conductivity (w/m-k),  $V$  is the velocity (m/s),  $\mu$  is the viscosity (kg/m-s),  $\mu_w$  is the wall viscosity (kg/m-s),  $\rho$  is the density ( $kg/m^3$ ),  $C_p$  is the specific heat (j/kg-k), and  $L$  is the characteristic length (m).

### 3. Results and Discussion

For the laboratory scale vacuum freeze-drying system, most of the process is carried out on the shelves. How to provide heat equally and efficiently on the shelves during the freeze-drying process would be crucial for product quality. Therefore, in five different types design of shelves, two problems are discussed: (1) the effect of different inlet and outlet positions on the same flow rate and temperature when the fluid flows into different plies of shelves; (2) the effects of different flow rates on the same temperature gradients of shelves after heat exchange between fluid in shelves and low temperature material.

In the application of a laboratory scale vacuum freeze-drying machine, only the first and second plies of shelves are used, the third ply is mostly idle. Therefore, only the temperature, velocity, and heat transfer rate distribution of the first and second plies are considered in this study. The results of the third ply are used as a reference.

The simulated results were shown in Figure 4. In Figure 4, the flow rate of the shelves was 2.5 L/min, In Case 1,

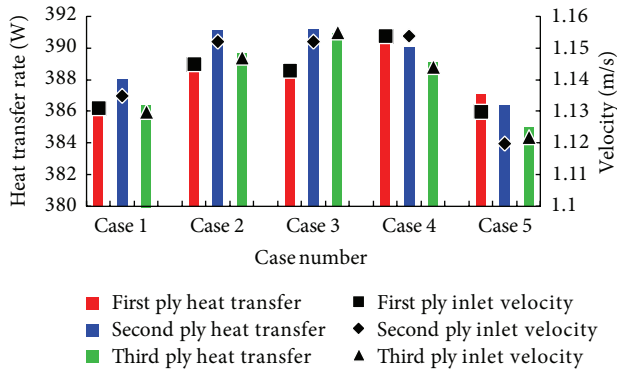


FIGURE 4: Variation of heat transfer rate with respect to inlet velocity at 2.5 L/min in various cases.

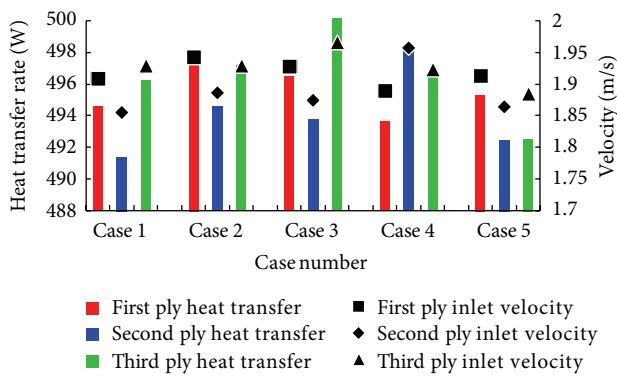


FIGURE 5: Variation of heat transfer rate with respect to inlet velocity at 5 L/min in various cases.

the difference of inlet velocity between the first ply and the third ply of the shelf is small. The performances of  $Q_c$  for the first and second plies were 386.689 W and 388.015 W, respectively. The difference between the first and second plies was 1.326 W. At the flow rate of 2.5 L/min in Case 4, the first and the second plies have the same inlet velocity of 1.154 m/s, and the inlet velocity of third ply was 1.144 m/s. The distribution of heat transfer rate  $Q_c$  for the first, second, and third plies was 390.728 W, 390.035 W, and 389.098 W, respectively. The difference of heat transfer rate  $Q_c$  between the first and second plies was 0.693 W, and the difference of the third ply is 1.63 W. The heat transfer rate of the three shelves in Case 4 was more uniform than other cases. Therefore, when the flow rate was 2.5 L/min, it was suggested to use the geometrical model of Case 4 as the reference design.

In Figure 5, the inlet flow rate was set as 5 L/min. The inlet velocities of the first, second, and third plies of shelf in Case 1 were 1.909 m/s, 1.855 m/s, and 1.929 m/s, respectively. In terms of performance in heat transfer rate  $Q_c$ , the heat transfer rate of the first, second, and third plies was 494.631 W, 491.430 W, and 496.265 W, respectively. The difference of heat transfer rates between the first and second plies was 4.551 W. In Case 3, the heat transfer rates  $Q_c$  of the first, second, and third plies were 496.524 W, 493.756 W, and 500.159 W, respectively. The difference between the first and second plies

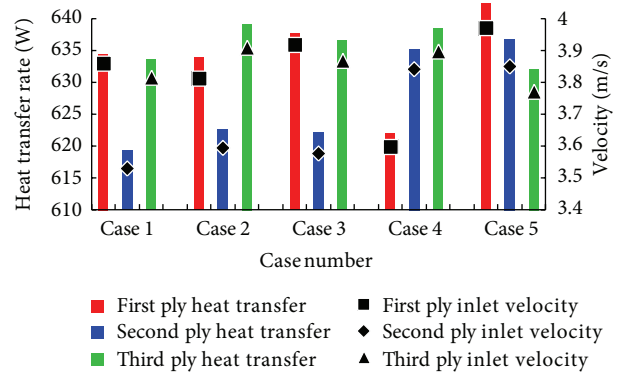


FIGURE 6: Variation of heat transfer rate with respect to inlet velocity at 10 L/min in various cases.

was 2.768 W, which was the smallest difference. In addition, the difference of heat transfer rate  $Q_c$  between the first and second plies of shelves in Case 5 was 2.839 W. Therefore, when the inlet flow rate was 5 L/min, Case 1 could be replaced by the geometric shape of Case 3.

In Figure 6, the inlet flow rate was set as 10 L/min. The simulating results of Case 1 show that the inlet velocity of the first, second, and third plies was 3.859 m/s, 3.531 m/s, and 3.816 m/s, respectively. The inlet velocity of the second ply was lower than that of the other two plies. In terms of distribution of heat transfer rate  $Q_c$ , the first, second, and third plies were 634.513 W, 619.403, and 633.628 W, respectively. The difference of  $Q_c$  between the first ply and the second ply was 14.228 W. In the other cases, the differences of  $Q_c$  between the first and second plies in Cases 2, 3, and 4 were 11.392 W, 15.535 W, and 13.258 W, respectively. The differences in these cases were above 10 W. However in Case 5, the difference of  $Q_c$  between the first and second plies was only 5.553 W, which was the smallest among all the cases. Therefore, when the flow rate was 10 L/min, the geometric shape of Case 5 could be used for the design.

In Figure 7, the inlet flow rate was set as 20 L/min. The shelf inlet velocities of the first and second plies were similar in Case 5. The inlet velocities of the first and second plies were 7.767 m/s and 7.678 m/s, respectively. Their difference was only 0.089 m/s, and the difference in other cases was above 0.357 m/s. For heat transfer rate  $Q_c$ , the difference was only 4.631 W in Case 5, and the difference in the other cases was 16.641 W~13.435 W. Therefore, when the flow rate was 20 L/min, the geometric shape of Case 5 was suggested.

The simulating results have a closer relationship between temperature gradient and heat flow rate in all the cases. Average results of all the cases were shown in Figure 8. In the flow rate range from 2.5 L/min to 20 L/min, the temperature gradient decreased from 0.062 to 0.018 K/cm monotonically, and the heat transfer rate increased from 388.7 to 775.5 W monotonically. The flow rate had an inverse linear relationship with the temperature gradient, however, a positive linear relationship with the heat transfer rate.

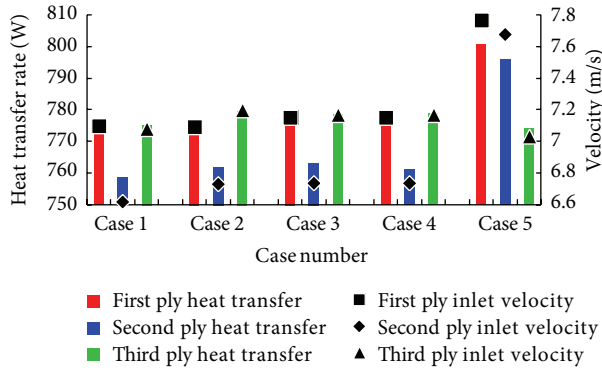


FIGURE 7: Variation of heat transfer rate with respect to inlet velocity at 20 L/min in various cases.

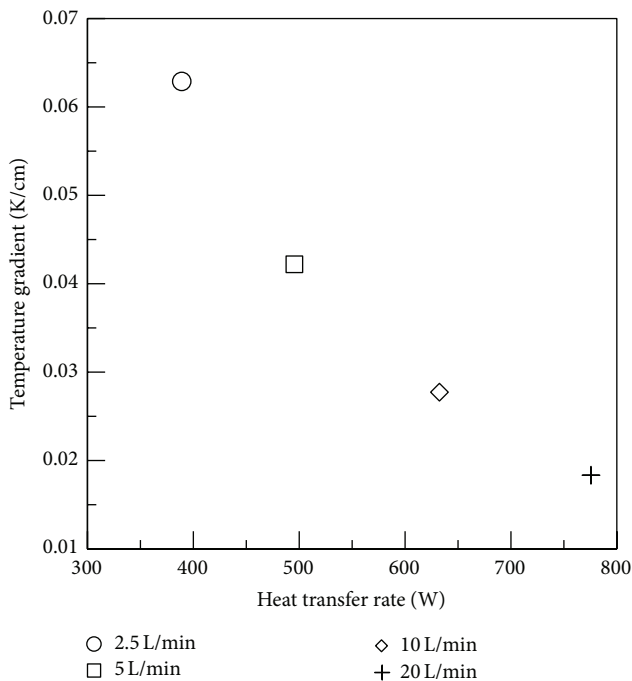


FIGURE 8: Temperature gradient with respect to heat transfer rate in various inlet velocities.

#### 4. Conclusions

Vacuum freeze-drying is a long-term process and has a close relation to temperature. This study discussed the effect of different inlet and outlet positions under the same flow rate and temperature of different plies of shelves and investigated the influences of different flow rates under the same temperature gradient of shelves after heat exchange between fluid and low temperature material in the shelves. The conclusions are as follows.

- (1) When the flow rate was 2.5 L/min, the inlet velocities of different plies of shelves are closest in Case 4. The difference of heat transfer rate  $Q_c$  between the first and second plies was only 0.693 W. This was the preferred design for the cases of lower flow rates, and

it may result in similar quality of materials even with different plies.

- (2) Although Case 1 was an actual case, when the flow rate was 5 L/min, the results show that Case 3 was more appropriate, and the difference between the first and second plies was 2.768 W.
- (3) Case 5 has a better heat transfer rate when the flow rates were 10 L/min and 20 L/min. The users can adopt the geometric shape of Case 5 when requiring the higher flow rates. In addition, the heat transfer rate in Case 5 was similar to that of Case 3, when the flow rate was 5 L/min. Therefore, the geometric shape of Case 5 allows a wide range of flow rates.
- (4) The temperature gradient and heat transfer rate had a close relationship with the flow rate. The flow rate had an inverse linear relationship with the temperature gradient, however, a positive linear relationship with the heat transfer rate.

The above results can serve as references for future studies on the geometric production of shelves and setting inlet flow rates for different flow rates.

#### Conflict of Interests

The authors declare that there is no conflict of interests regarding the publication of this paper.

#### Acknowledgment

This study was sponsored by the National Science Council, Taiwan, NSC (100-2221-E-027-074).

#### References

- [1] A. A. Barresi, R. Pisano, D. Fissore et al., "Monitoring of the primary drying of a lyophilization process in vials," *Chemical Engineering and Processing: Process Intensification*, vol. 48, no. 1, pp. 408–423, 2009.
- [2] M. J. Pikal, "Freeze-drying of proteins—part II: formulation selection," *BioPharm*, vol. 3, pp. 26–30, 1990.
- [3] A. I. Liapis and R. Bruttini, "Exergy analysis of freeze drying of pharmaceuticals in vials on trays," *International Journal of Heat and Mass Transfer*, vol. 51, no. 15-16, pp. 3854–3868, 2008.
- [4] S. M. Patel, T. Doen, and M. J. Pikal, "Determination of end point of primary drying in freeze-drying process control," *AAPS PharmSciTech*, vol. 11, no. 1, pp. 73–84, 2010.
- [5] H. Gieseler, W. J. Kessler, M. Finson et al., "Evaluation of tunable diode laser absorption spectroscopy for in-process water vapor mass flux measurements during freeze drying," *Journal of Pharmaceutical Sciences*, vol. 96, no. 7, pp. 1776–1793, 2007.
- [6] X. Tang and M. J. Pikal, "Design of freeze-drying processes for pharmaceuticals: practical advice," *Pharmaceutical Research*, vol. 21, no. 2, pp. 191–200, 2004.
- [7] R. Pisano, D. Fissore, and A. A. Barresi, "Freeze-drying cycle optimization using model predictive control techniques," *Industrial and Engineering Chemistry Research*, vol. 50, no. 12, pp. 7363–7379, 2011.

- [8] S. S. Sablani and M. S. Rahman, "Pore formation in selected foods as a function of shelf temperature during freeze drying," *Drying Technology*, vol. 20, no. 7, pp. 1379–1391, 2002.
- [9] X. Tang, S. L. Nail, and M. J. Pikal, "Freeze-drying process design by manometric temperature measurement: design of a smart freeze-dryer," *Pharmaceutical Research*, vol. 22, no. 4, pp. 685–700, 2005.
- [10] H. Gieseler, T. Kramer, and M. J. Pikal, "Use of manometric temperature measurement (MTM) and SMARTÛ freeze dryer technology for development of an optimized freeze-drying cycle," *Journal of Pharmaceutical Sciences*, vol. 96, no. 12, pp. 3402–3418, 2007.
- [11] W. J. Mascarenhas, H. U. Akay, and M. J. Pikal, "A computational model for finite element analysis of the freeze-drying process," *Computer Methods in Applied Mechanics and Engineering*, vol. 148, no. 1-2, pp. 105–124, 1997.
- [12] A. Hottot, R. Peczaliski, S. Vessot, and J. Andrieu, "Freeze-drying of pharmaceutical proteins in vials: modeling of freezing and sublimation steps," *Drying Technology*, vol. 24, no. 5, pp. 561–570, 2006.
- [13] Y.-Y. Kim and K.-S. Lee, "Comparative numerical study of freeze drying of solution and spray-frozen particles in trays and vials," *Numerical Heat Transfer A: Applications*, vol. 54, no. 4, pp. 406–425, 2008.
- [14] M. Brülls and A. Rasmuson, "Heat transfer in vial lyophilization," *International Journal of Pharmaceutics*, vol. 246, no. 1-2, pp. 1–16, 2002.
- [15] S. H. Bae, J. H. Nam, C. S. Song, and C.-J. Kim, "A numerical model for freeze drying processes with infrared radiation heating," *Numerical Heat Transfer A: Applications*, vol. 58, no. 5, pp. 333–355, 2010.
- [16] M. P. Schoen, B. K. Braxton, L. A. Gatlin, and R. P. Jefferis III, "A simulation model for the primary drying phase of the freeze-drying cycle," *International Journal of Pharmaceutics*, vol. 114, no. 2, pp. 159–170, 1995.

## Research Article

# Effects of Surface Modification of Nanodiamond Particles for Nucleation Enhancement during Its Film Growth by Microwave Plasma Jet Chemical Vapour Deposition Technique

Chii-Ruey Lin,<sup>1,2,3</sup> Da-Hua Wei,<sup>1,2,3</sup> Minh-Khoa BenDao,<sup>2,3</sup> Hong-Ming Chang,<sup>2,3</sup>  
Wei-En Chen,<sup>2,3</sup> and Jen-Ai Lee<sup>4</sup>

<sup>1</sup> Department of Mechanical Engineering and Institute of Manufacturing Technology, National Taipei University of Technology, Taipei 106, Taiwan

<sup>2</sup> Graduate Institute of Mechanical and Electrical Engineering, National Taipei University of Technology, Taipei 106, Taiwan

<sup>3</sup> Institute of Mechatronic Engineering, National Taipei University of Technology, Taipei 106, Taiwan

<sup>4</sup> School of Pharmacy, Taipei Medical University, Taipei 11031, Taiwan

Correspondence should be addressed to Chii-Ruey Lin; [crlin@ntut.edu.tw](mailto:crlin@ntut.edu.tw) and Jen-Ai Lee; [jenai@tmu.edu.tw](mailto:jenai@tmu.edu.tw)

Received 13 September 2013; Revised 12 January 2014; Accepted 13 January 2014; Published 5 May 2014

Academic Editor: Ching-Song Jwo

Copyright © 2014 Chii-Ruey Lin et al. This is an open access article distributed under the Creative Commons Attribution License, which permits unrestricted use, distribution, and reproduction in any medium, provided the original work is properly cited.

The seedings of the substrate with a suspension of nanodiamond particles (NDPs) were widely used as nucleation seeds to enhance the growth of nanostructured diamond films. The formation of agglomerates in the suspension of NDPs, however, may have adverse impact on the initial growth period. Therefore, this paper was aimed at the surface modification of the NDPs to enhance the diamond nucleation for the growth of nanocrystalline diamond films which could be used in photovoltaic applications. Hydrogen plasma, thermal, and surfactant treatment techniques were employed to improve the dispersion characteristics of detonation nanodiamond particles in aqueous media. The seeding of silicon substrate was then carried out with an optimized spin-coating method. The results of both Fourier transform infrared spectroscopy and dynamic light scattering measurements demonstrated that plasma treated diamond nanoparticles possessed polar surface functional groups and attained high dispersion in methanol. The nanocrystalline diamond films deposited by microwave plasma jet chemical vapour deposition exhibited extremely fine grain and high smooth surfaces (~6.4 nm rms) on the whole film. These results indeed open up a prospect of nanocrystalline diamond films in solar cell applications.

## 1. Introduction

Since chemical vapour deposition (CVD) diamond films possess many outstanding properties of diamond with low dimensional structure, they have increasingly attracted interests in the area of nanomanufacturing including semiconductor, optics, biomedical, and biosensor engineering [1–6]. Also, due to other important features including transparency over a wide spectral range, good thermal stability, and wear resistance, the films have been considered as promising candidates to replace silicon and metal in high performance devices which operate in harsh environments. High quality undoped CVD diamond films with n- and p-type characteristics have been successfully manufactured by the most

common techniques including microwave plasma-enhanced chemical vapour deposition (MPECVD) and hot filament chemical vapour deposition (HFCVD) [7–10].

The CVD-deposited diamond film normally consists of diamond grains and grain boundaries containing impurities as well as nondiamond carbon phase. The diamond grains and grain boundaries have significant effects on not only the electrical properties, but also the surface roughness of the diamond films. Obviously, high surface roughness may hinder the performance of the diamond-based devices such as MEMS, biosensor, and p-n junction-based device. In a typical diamond film grown by CVD techniques, the surface roughness is directly related to the diamond nucleation enhancement which is also known as “pretreatment”

procedure. Till now, the enhancement of the diamond nucleation density for nondiamond substrate can be carried out by various methods including spin-coating with a diamond slurry, plasma precarburization, scratching with  $\text{Al}_2\text{O}_3$  or diamond powders, ultrasonication with mixture of nanometal and nanodiamond particles (NDPs), and bias-enhance nucleation. Among these, the method of spin-coating with diamond slurry in air at room temperature is inexpensive, environment friendly, and relatively simple; thus it is appropriate for the growth of large-area diamond film, reduces the production cost, and is suitable for the commercial applications. It should be noted here that the size of particle used for spin-coating procedure also influences roughness of the diamond films, resulting in demand of a highly dispersed aqueous suspension of diamond particles with uniform and ultrafine particle size.

Commercial detonation NDPs with round shape are usually used for nucleation enhancement step in CVD diamond growth [11]. It is well known that the significant impurities from nondiamond carbon and metal existing in postsynthesized carbon soot include NDPs and, however, lead to serious aggregation phenomena of typical ND particles. In this study, we employed various surface modification techniques to improve the dispersion characteristics of NDPs in methanol solution, aiming at the diamond nucleation enhancement step in a typical CVD diamond growth process.

## 2. Experimental

Detonation diamond nanoparticles having 4–6 nm in mean diameter were purchased from Fact Diamond Company, a famous diamond manufacturing company. The NDPs were first purified by an acid treatment procedure using an acid mixture of  $\text{HNO}_3 : \text{H}_2\text{SO}_4 : \text{H}_2\text{O}_2 = 1 : 1 : 3$  in glass autoclave at  $100^\circ\text{C}$  for 1 h with ultrasonication enhancement. The purified powders were then rinsed in double-distilled water for several times until the disappearance of the dark-yellowish color of the suspension, followed by recovery procedures using centrifuged classification equipment and evaporation in room temperature. The acid-treated diamond nanoparticles are denoted as A-NDPs. The hydrogenation of A-NDPs was carried out using MPECVD system with hydrogen plasma excited at 600 W and 60 Torr of microwave power and working pressure, respectively. Thermal treatment process was conducted on the A-NDPs at  $550^\circ\text{C}$  under vacuum ambient for 3 h. Also, in other experiments of A-NDPs with surfactant, 50 mg of diamond particles was dispersed in 40 mL  $(\text{CH}_2)_4\text{O}$  (tetrahydrofuran (THF)) as dispersion media added by 30 wt% oleylamine (OLA). In all examinations of the dispersion of the diamond nanoparticles, the diamond suspension was obtained using 0.75 wt% NDPs in methanol. The as-received suspensions were then employed for the diamond nucleation enhancement using spin-coating technique. In this study, diamond films were deposited onto nucleated silicon substrate having size of  $20 \times 20 \times 1 \text{ mm}^3$  by microwave plasma jet chemical vapour deposition (MPJCVD) system at 35 Torr and with gas mixture of 8%  $\text{CH}_4 : 92\% \text{H}_2$  as precursors. The deposition time was 2 h.

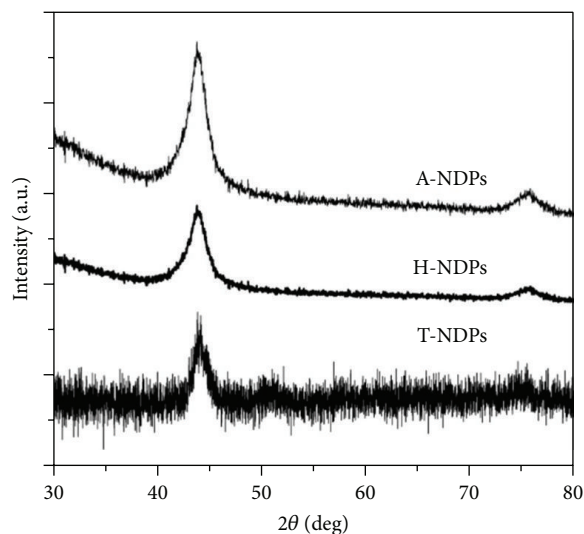


FIGURE 1: X-ray diffraction patterns for the diamond nanoparticles after different surface modification procedures using harsh acid (A-NDPs), hydrogen plasma (H-NDPs), and thermal (T-NDPs) treatments.

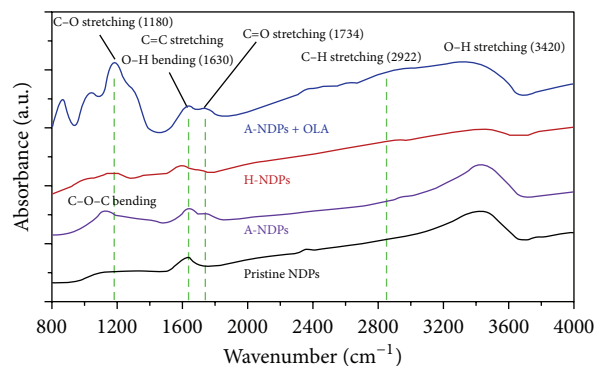


FIGURE 2: FT-IR spectra of pristine NDPs and the diamond particles treated by harsh acid (A-NDPs), hydrogen plasma (H-NDPs), and oleylamine solvent.

X-ray diffractometer (XRD) with  $\text{CuK}\alpha$  radiation ( $\lambda = 0.1542 \text{ nm}$ ) was employed to characterize the effect of the hydrogen plasma and thermal treatment procedures on the crystallinity of the NDPs. Dynamic light scattering (DLS) was used to investigate the dispersion of the NDPs in organic solution. Fourier transform infrared (FT-IR) was conducted with KBr method to analyze the surface functional groups of the as-prepared NDPs. Scanning electron microscope (SEM) and transmission electron microscope (TEM, JEOL JEM-2100F) were used to examine the characteristics of the nanodiamond particles.

## 3. Results and Discussion

The effects of the harsh acid treatment and surface modification procedures on the structural alteration of NDPs were investigated by X-ray diffraction. Figure 1 shows the XRD patterns of the diamond particle samples treated with

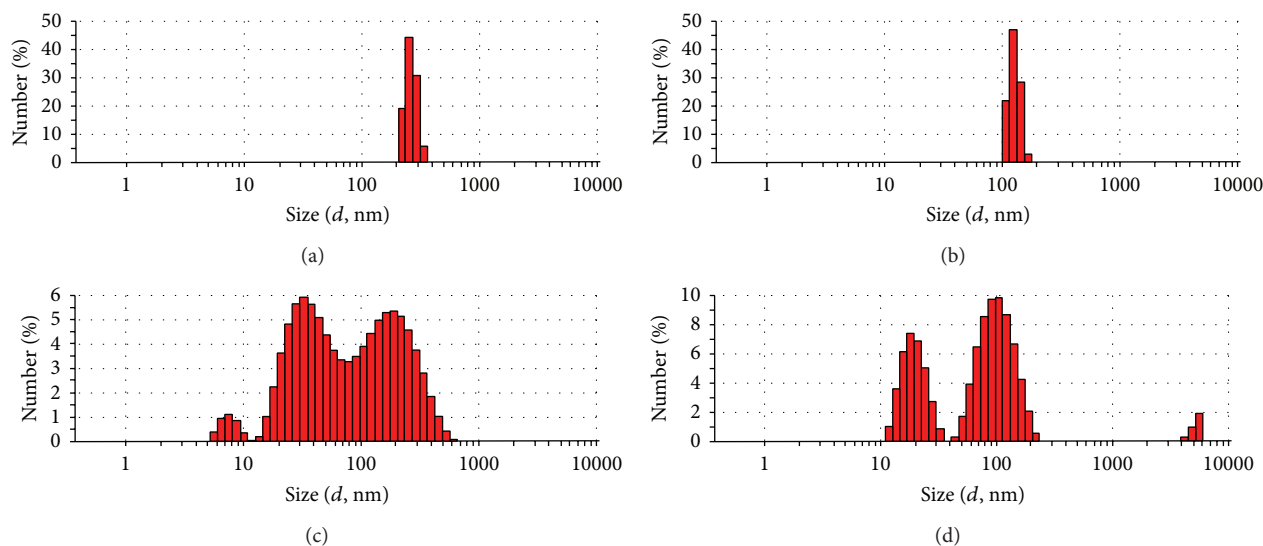


FIGURE 3: Size distribution of NDPs after treatment procedures using (a) harsh acid mixture, (b) vacuum annealing, (c) OLA surfactant, and (d) hydrogen plasma.

harsh acid (A-NDPs), hydrogen plasma (H-NDPs), and postannealing procedure (T-NDPs). All spectra show the characteristic peak of the (111) crystalline orientation of the diamond structure ( $2\theta = 43.935^\circ$ , JCPDS number 89-3441). The diffraction peak of the acid-treated NDPs with high intensity exhibits highly crystalline structure of the diamond particles. The XRD pattern of the A-NDPs also demonstrated that the heavy metal and nondiamond carbon impurities that existed in pristine diamond particle samples, on the whole, were thoroughly removed by the acid treatment procedures. After 1 h of hydrogenation process, the diffraction intensity of diamond peak turned to be weaker and broader due to the graphitization induced by microwave plasma; however, a further analysis to confirm this suggestion is needed. In both A-NDPs and H-NDPs, the crystallite size of the diamond particles was estimated through the full width at half maximum (FWHM) and in qualitative agreement with the characteristics of the commercial diamond nanoparticles synthesized by detonation method which have size range of 5–10 nm. In other words, the hydrogenation used had no remarkable effects on the size of the diamond core structure of the NDPs. The diffraction line of the sample annealed in vacuum ambient for 3 h at  $550^\circ\text{C}$  was relatively weak with higher intensity of the noise signals revealing the formed noncubic diamond and impurities component, exhibiting the surface graphitization as well as a harsh oxidation of diamond particles.

Figure 2 shows the FT-IR spectra of the pristine diamond particles and the obtained samples after acid treatment, hydrogenation, and surface modification using OLA solvent as surfactant. The spectra of pristine NDPs exhibited the main features related to C=C ( $1625\text{ cm}^{-1}$ ) and O-H stretching vibration ( $3450\text{ cm}^{-1}$ ). The apparent peak at  $1734\text{ cm}^{-1}$  in the spectra of the samples treated with harsh acid mixture indicates the induced C=O stretching as result of the conversions of original functional groups such as alcohols into carboxylic

acids. Also, the apparent C–O–C bending ( $1105\text{ cm}^{-1}$ ) reveals the formation of the carbonyl groups on the surface of the NDPs which may have resulted from the ether bonds between NDPs during the acid treatment procedure. This also can be observed in other oxidation processes. The FT-IR spectra of the hydrogenated NDPs show the significant blue shift and weakening of C=C stretching, indicating the hydrogen etching of graphite phase and nondiamond impurities ingredient in the NDPs samples. These results demonstrate that the hydrogenation using microwave plasma contributed to the elimination of hydrophobic surface functional groups such as carbonyl and carboxyl. For the A-NDPs modified with OLA solvent, the spectra show the added groups on the surface of diamond particle corresponding to C–O stretching ( $1180\text{ cm}^{-1}$ ) and the deformation O–H bending ( $1630\text{ cm}^{-1}$ ) which were assigned to the esters, alcohols, and aldehydes.

Figure 3 shows the dispersion characteristics of NDPs samples obtained after different surface modification in aqueous solution at pH 7. The acid-treated NDPs exhibit severe agglomeration with about 300 nm in dimension. After the annealing procedure in vacuum ambient at  $550^\circ\text{C}$ , the agglomeration size becomes smaller than 200 nm as over 45% of the particles have measured size range of 140 nm. The NDPs treated with OLA surfactant and hydrogen plasma possess higher dispersion in methanol solution which have wide particle size distribution and are consistent with the aforementioned surface characterization. The existent agglomeration of NDPs in solution may be led by the C–O–C bonding between adjacent particles which was observed in the FT-IR spectra.

Figures 4(a) and 4(b) show the TEM image of the NDPs treated with OLA surfactant and hydrogen plasma, which demonstrates that the prepared samples have highly dispersive property in the methanol solution. Moreover, the hydrogenated nanoparticles seem to have better dispersion while agglomeration can be observed in the OLA treated

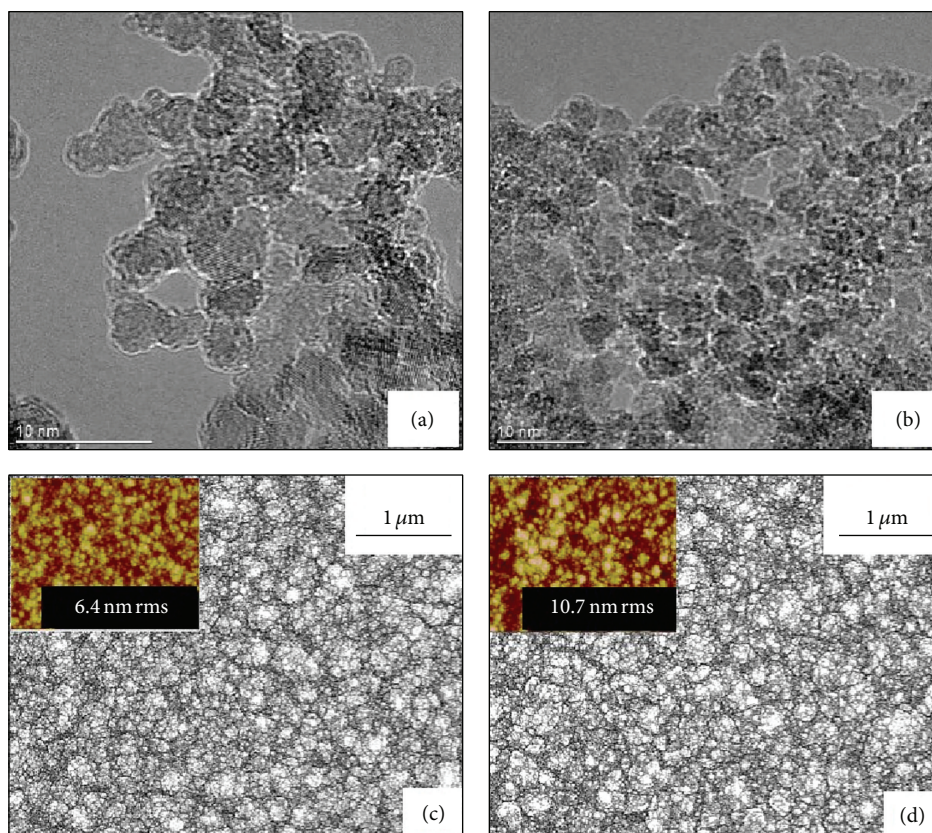


FIGURE 4: High resolution TEM image of NDPs treated by (a) hydrogen plasma and (b) OLA surfactant and the nanocrystalline diamond films grown with nucleation enhancement using suspension of (c) H-NDPs and (d) OLA treated NDPs.

diamond sample. The diamond nanoparticles suspension was further employed in diamond nucleation enhancement step for nanocrystalline diamond films growth using spin-coating technique. The morphology of the as-prepared diamond films is shown in plan-view SEM. As shown in Figure 4(c), the diamond films growth with the nucleation enhancement by H-NDPs suspension exhibits a smooth morphology with very fine grains less than 40 nm in size and without any grain cluster. The films growth from the nucleated substrate using OLA treated suspension possesses coarser diamond grain and higher surface roughness (10.7 nm), as shown in Figure 4(d). These above results confirm the aforementioned trends on the size distribution of the NDPs in methanol.

#### 4. Conclusion

In this study, various surface modification methods for commercial nanodiamond particles have been employed to improve their dispersion in aqueous solution, aiming at high performance diamond nucleation enhancement for nanocrystalline diamond films growth with low surface roughness. The hydrogen plasma was found to significantly improve the dispersive of the NDPs due to the elimination of the contained covalent bonds and hydrophobic functional groups, while OLA could be good surfactant for diamond suspension due to the added hydrophilic surface functional

groups. The hydrogenation also had no remarkable effects on the crystalline structure of the diamond particles but contributed to the etching of the existed nondiamond phases. The deposited diamond films with nucleation enhancement using the as-prepared diamond suspension exhibited highly smooth surface whose measured surface roughness was 7 nm below. The achieved results demonstrate an avenue to scale up the production of diamond films for solar cell applications.

#### Conflict of Interests

The authors declare that there is no conflict of interests regarding the publication of this paper.

#### Acknowledgments

This work was financially supported by the Main Research Project of the National Science Council of China under Grant no. NSC 102-2221-E-027-040-MY2 and the Co-operation Project of National Taipei University of Technology and Taipei Medical University under Grant no. NTUT-TMU-101-07.

#### References

- [1] D. R. Mumm, K. T. Faber, M. D. Drory, and C. F. Gardinier, "High-temperature hardness of chemically vapor-deposited

- diamond,” *Journal of the American Ceramic Society*, vol. 76, no. 1, pp. 238–240, 1993.
- [2] M. Akaishi, S. Yamaoka, J. Tanaka, T. Ohsawa, and O. Fukunaga, “Synthesis of sintered diamond with a high electrical resistivity and high hardness,” *Materials Science and Engineering*, vol. 105–106, no. 2, pp. 517–523, 1988.
- [3] D. M. Bhusari, J. R. Yang, T. Y. Wang, K. H. Chen, S. T. Lin, and L. C. Chen, “Effects of substrate pretreatment and methane fraction on the optical transparency of nanocrystalline diamond thin films,” *Journal of Materials Research*, vol. 13, no. 7, pp. 1769–1773, 1998.
- [4] H. Bai, N. Ma, J. Lang, C. Zhu, and Y. Ma, “Thermal conductivity of Cu/diamond composites prepared by a new pretreatment of diamond powder,” *Composites Part B: Engineering*, vol. 52, pp. 182–186, 2013.
- [5] C.-R. Lin, W.-H. Liao, D.-H. Wei, J.-S. Tsai, C.-K. Chang, and W.-C. Fang, “Formation of ultrananocrystalline diamond films with nitrogen addition,” *Diamond and Related Materials*, vol. 20, no. 3, pp. 380–384, 2011.
- [6] W. H. Liao, C. R. Lin, D. H. Wei et al., “Concurrent improvement in biocompatibility and bioinertness of diamond-like carbon films with nitrogen doping,” *Journal of Biomedical Materials Research A*, vol. 100, no. 11, pp. 3151–3156, 2012.
- [7] C. R. Lin, D. H. Wei, M. K. BenDao, R. J. Chung, and H. M. Chang, “Nanocrystalline diamond particles prepared by high-energy ball milling method,” *Applied Mechanics and Materials*, vol. 284–287, pp. 168–172, 2013.
- [8] Y. H. Dong, R. Q. Zhang, and Z. G. Ye, “Effect of diamond on the thermal conductivities of diamond-copper composites prepared by spark plasma sintering,” *Advanced Materials Research*, vol. 532–533, pp. 25–29, 2012.
- [9] H. Gomez, C. L. Frewin, A. Kumar, S. E. Sadow, and C. Locke, “Study of the adhesion and biocompatibility of nanocrystalline diamond (NCD) films on 3C-SiC substrates,” *Materials Research Society Symposium Proceedings*, vol. 1203, pp. 179–184, 2010.
- [10] M. Amaral, P. S. Gomes, M. A. Lopes, J. D. Santos, R. F. Silva, and M. H. Fernandes, “Nanocrystalline diamond as a coating for joint implants: cytotoxicity and biocompatibility assessment,” *Journal of Nanomaterials*, vol. 2008, Article ID 894352, 9 pages, 2008.
- [11] W. H. Liao, C. R. Lin, and D. H. Wei, “Effect of CH<sub>4</sub> concentration on the growth behavior, structure, and transparent properties of ultrananocrystalline diamond films synthesized by focused microwave Ar/CH<sub>4</sub>/H<sub>2</sub> plasma jets,” *Applied Surface Science*, vol. 270, pp. 324–330, 2013.

## Research Article

# Synthesis and Characterization of SiO<sub>2</sub> Nanoparticles and Their Efficacy in Chemical Mechanical Polishing Steel Substrate

M. J. Kao,<sup>1</sup> F. C. Hsu,<sup>2</sup> and D. X. Peng<sup>3</sup>

<sup>1</sup> Department of Vehicle Engineering, National Taipei University of Technology, 1, Sec. 3, Chung-Hsiao E. Road, Taipei 10643, Taiwan

<sup>2</sup> Graduate Institute of Mechanical and Electrical Engineering, National Taipei University of Technology, 1, Sec. 3, Chung-Hsiao E. Road, Taipei 10643, Taiwan

<sup>3</sup> Department of Vehicle Engineering, Army Academy, 750 Longdong Road, Taoyuan 32092, Taiwan

Correspondence should be addressed to F. C. Hsu; wagon0335rw@gmail.com

Received 12 September 2013; Revised 9 February 2014; Accepted 23 February 2014; Published 27 March 2014

Academic Editor: Ho Chang

Copyright © 2014 M. J. Kao et al. This is an open access article distributed under the Creative Commons Attribution License, which permits unrestricted use, distribution, and reproduction in any medium, provided the original work is properly cited.

Chemical mechanical polishing (CMP) technology is extensively used in the global planarization of highly value-added and large components in the aerospace industry. A nanopowder of SiO<sub>2</sub> was prepared by the sol-gel method and was compounded into polishing slurry for the CMP of steel substrate. The size of the SiO<sub>2</sub> abrasives was controlled by varying the sol-gel reaction conditions. The polishing efficacy of nano-SiO<sub>2</sub> was studied, and the CMP mechanism with nanosized abrasives was further investigated. The proposed methods can produce SiO<sub>2</sub> abrasives whose size can be controlled by varying the sol-gel reaction conditions. The size of the SiO<sub>2</sub> abrasives was controlled in the range from 58 to 684 nm. The roughness of the steel substrate strongly depends on the size of the abrasive, and the surface roughness decreases as the abrasive size declines. A super-smooth surface with a roughness of 8.4 nm is obtained with nanosized SiO<sub>2</sub>. Ideal CMP slurry can be used to produce material surfaces with low roughness, excellent global planarization, high selectivity, an excellent finish, and a low-defected rate.

## 1. Introduction

As the requirements for precise microcomponents have increased dramatically for the last few years, finishing techniques to improve the surfaces of microstructures have attracted more attention. For example, the surface quality of microlenses critically affects the performance of an optical system. To produce glass, ceramics, and semiconductors with surfaces of superior quality, abrasive polishing is commonly required as a finishing step [1]. Chemical mechanical polishing (CMP) is a suitable method for smoothing the surface. It is used in many industrial processes, including the manufacture of devices and materials. It has recently attracted much interest owing to its strong performance in terms of material removal rate (MRR) and surface quality.

Steel substrate could be applied to the surface grinding machine, slideway, air bearing, and so on. There were more and more ultraprecision machines with the use of CMP technique in order to produce steel substrate. During

the CMP process, the formation and removal of the oxide layer are done repeatedly. Thakurta et al. [2] used slurry hydrodynamics, mass transport, and reaction kinetics to predict the polishing rate of a steel film. These steps include (1) mass transport of the oxidizer to the steel surface; (2) reaction of the oxidizer with steel to form a reacted layer, and (3) subsequent removal of the reacted layer by mechanical abrasion [3]. In the CMP process, the extension of surface defect formation must be minimized while good planarity and optimal material removal rates are maintained. Removing materials from films' surfaces in the CMP process is typically performed by chemical reaction and mechanical abrasion. The major process parameters of CMP are slurry, polishing pressure, and polishing pad. In CMP, the abrasive critically affects the quality of the polished surface. Its properties, including type, size, shape, and concentration of particles, significantly affect CMP performance. Presently, alumina, silica, and ceria are extensively used in CMP slurries as traditional inorganic abrasives [4, 5].

One of the most critical problems is the high cost of consumables (COC), such as the pad and slurry, which are responsible for over 70% of cost of ownership (COO). Since enough slurry is required to yield a high removal rate and low nonuniformity, the purchase of slurry is responsible for approximately half of the COC for a typical CMP process. Silica ( $\text{SiO}_2$ ) is used in CMP slurry because it has relatively significant advantages. It can be easily prepared as monodispersed spheres by the sol-gel method and the preparation cost is low.

Nanoparticles have attracted much interest in recent years due to their excellent physical and chemical properties. They are different from conventional bulk materials in their extremely small size and larger specific area of surface. The preparation and applications of nanoparticles for adding in slurry have become important fields of research. Nanoparticles have been prepared by precipitation, solvothermal methods, radiolytic methods, electrochemical methods, chemical reduction, plasma, chemical vapor deposition, and the sol-gel method. Of these approaches, the sol-gel method is particularly useful. Its advantages are effective stoichiometric control and the production of ultrafine particles with a narrow size distribution in relatively short processing time at low temperatures.

$\text{SiO}_2$  nanoparticles have particular physical, chemical, and optical properties that have led to its wide use in many fields. They are used as functional materials, catalyst, plastics, rubbers paints, biomedicine, and semiconductive material. High-quality  $\text{SiO}_2$  nanoparticles cannot be produced by conventional methods. The sol-gel approach is one of the most important methods for preparing high-quality nano- $\text{SiO}_2$  powders [6].

The colloidal silica of monodispersed sizes is commonly synthesized by the Stöber et al. [7] process by hydrolysis and the condensation of TEOS precursors in an alcoholic medium, catalyzed by ammonia or acid. In this work,  $\text{SiO}_2$  particles of uniformly distributed sizes were synthesized by the sol-gel method. The obtained  $\text{SiO}_2$  particles have many advantages, including narrow size distribution and desirable characteristics, such as very small size, high chemical purity, and high chemical homogeneity. However, this method has rarely been applied to synthesize  $\text{SiO}_2$  abrasives for CMP slurry [8].

According to Seo and Lee [9], the polishing mechanism in the CMP process involves repeated passive layer formation by the oxidizer and abrasion by the abrasives in the slurry. However, balanced etching and passivation reactions are required to avoid a high etching rate and to ensure a high global surface planarity. Larsen-Basse and Liang [10] reviewed the fundamental mechanisms of the material removal in lapping and polishing processes and identified key areas where further work is required. Zhang and Lei [11] discussed material removal mechanisms in the finishing of advanced ceramics and glasses. To improve planarization in the CMP process, the nature of the contact between the abrasive and the oxide layer must be understood in detail, and the effect of the abrasive slurry studied. Understanding the effect of an oxidizer on the metal passivation film is important to increase the removal rate and achieve a very low

nonuniformity. Future optimization of CMP metal patterning will require a deeper understanding of the mechanisms of material removal during polishing [11, 12].

Xie and Bhushan [13] provided a theoretical model, based on the abrasion mechanism, to predict the effects of particle size, the polishing pad, and the contact pressure during the CMP process. Luo and Dornfeld [14] took a step toward determining the effect of the distribution of sizes of abrasives on the surface roughness of material in CMP. The main cause of microscratches is reportedly very large particles in the slurry. A CMP experiment conducted by Basim et al. [15] revealed that the frequency of microscratches increased with the size and the number of the largest abrasive particles. Zhong et al. [16] observed that the density of the microscratches increased with polishing pressure and their size increased with the abrasive particles. Mechanical abrasion by the sliding indentation of abrasive particles is believed to be the main cause of microscratching [1].

Presently, larger abrasives are typically used in the polishing of silicon wafers, commonly damaging their surfaces severely and causing CMP to create a polishing haze. The main problems in the final CMP processes include surface scoring, a polishing haze, and contamination by metal ions and residual particles. Smaller abrasions are usually recognized to produce surfaces with better finishes. No conclusive results have been obtained concerning the effect of the abrasive particle size on the roughness of CMP material. In this work, single crystalline  $\text{SiO}_2$  particles with various mean sizes were synthesized by the sol-gel method. Therefore, the effects of polishing on the average roughness (Ra) of the surface were studied in a steel substrate that had undergone CMP with the prepared  $\text{SiO}_2$  nanoparticles abrasives.

## 2. Experimental Procedure

**2.1. Materials.** The formation of  $\text{SiO}_2$  nanoparticles via sol-gel approaches was studied (Lindberg et al. [6]; Satoh et al. [17]; Zhao et al. [18]). A precursor solution was prepared from tetraethyl orthosilicate (TEOS:  $\text{Si}(\text{OC}_2\text{H}_5)_4$ , technical grade, 97%); ethanol (95%) was adopted as the solvent of the precursor. Ammonia ( $\text{NH}_3$ , 28%) solution was used to increase the pH to promote gelation.  $\text{H}_2\text{O}$  was distilled and underwent ion-exchange. All reagents were used without further purification. The workpieces were made of steel disk substrates (AISI 52100 steel; composition: 0.95–1.05% C, 0.15–0.35% Si, 0.2–0.4% Mn, <0.027% P, <0.020% S, 1.3–1.65% Cr, <0.3% Ni, and <0.25% Cu), containing surface hardness of 60–62 HRC. The surface average roughness (Ra) of disk substrates before polishing is around  $\text{Ra} = 0.1 \mu\text{m}$ . A commercial polishing pad was made by Sense Tek Co., Ltd. Taiwan; Table 1 presents its physical properties.

**2.2. Preparation of  $\text{SiO}_2$  Nanoparticles.** The  $\text{SiO}_2$  nanoparticles were prepared by the following procedure. Solution A was a mixture of TEOS (0.025–0.3 mol) and ethanol (0.25–1.5 mol). Solution B was a mixture of  $\text{NH}_3$  (0.1–0.75 mol),  $\text{H}_2\text{O}$  (0.25–2.0 mol), and ethanol (0.25–1.5 mol). Solutions A and B were then mixed together with vigorous stirring

TABLE 1: Physical properties of the pad supplier.

Thickness (mm)	1.2
Weight (g/m <sup>2</sup> )	350
Density (g/m <sup>3</sup> )	0.40
Compressibility (%)	8.5
Elasticity (%)	82
Pore size (μm)	40

for 30 min. The final mixture was dried at 80°C for 6 hours and calcined for 24 hours at 120°C. Finally, different sizes of SiO<sub>2</sub> nanoparticles were obtained. Figure 1 presents the procedure for synthesizing SiO<sub>2</sub> nanoparticle. The particle size distribution of the SiO<sub>2</sub> nanoparticles was measured by using a laser particle size analyzer.

**2.3. Preparation of Slurries for CMP.** To study the CMP performance of the synthesized SiO<sub>2</sub> abrasives, a polishing test was performed using six slurries with different sized abrasives. The polishing slurries were prepared with nanosized SiO<sub>2</sub> powder and DI water. SiO<sub>2</sub> particles were added to DI water in a container with continuous stirring. This mixed slurry was sufficiently dispersed by using a stirrer before polishing to prevent aging and the precipitation of the mixed slurry. H<sub>2</sub>O<sub>2</sub> as an oxidizer was used. Ultrasound was used to disperse the oxidizer in the slurry. After the pH value was adjusted to between three and four by adding NaOH, the mixture was milled for one hour in a vibrator that contained ZrO<sub>2</sub> balls. Then, the mixture was filtered with a 1 μm pore filter. The baseline slurry was used to compare the relative polishing performance of the slurries developed in this study.

**2.4. Polishing Tests.** Figure 2 schematically depicts a typical CMP process. Before polishing, the slurry was agitated continuously with a magnetic stirrer to maintain good dispersion. The slurry was constantly fed to the center of the platen [10]. Table 2 presents the ranges of the down force, down pressure, table speed, and slurry flow rate. The polishing time in the CMP process on the polishing performance was measured.

**2.5. Measurements of Polishing Material Surface Roughness.** The roughness of the steel substrate was measured before and after polishing with a surface profiler. The average roughness (Ra) of the polish surface was measured to evaluate the effects of polishing in various slurries. The abrasive particles and polished samples were studied via using SEM. All of the above factors served as incentives to develop the basic understanding and the necessary tools to control the CMP process closely.

### 3. Results and Discussion

**3.1. Characterization of SiO<sub>2</sub> Nanoparticles.** Figure 3 presents the FE-SEM micrograph and particle size distribution of the SiO<sub>2</sub> nanoparticles obtained under different sol-gel conditions. The photograph of the SiO<sub>2</sub> nanoparticles indicates

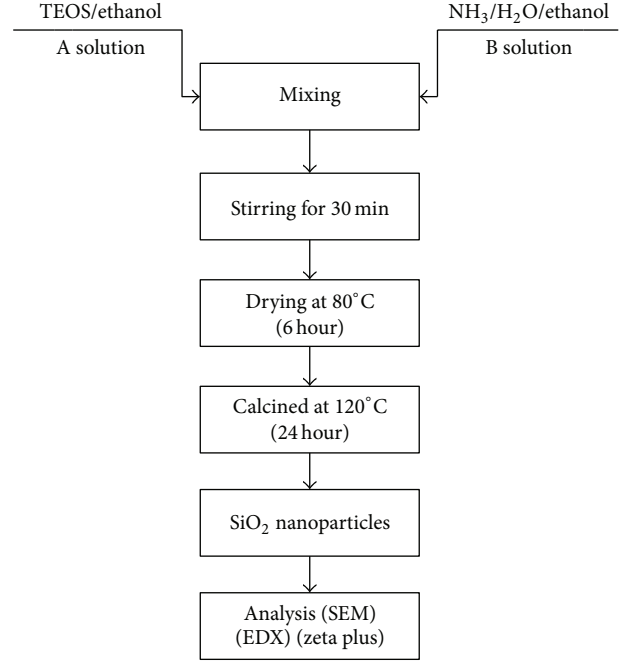
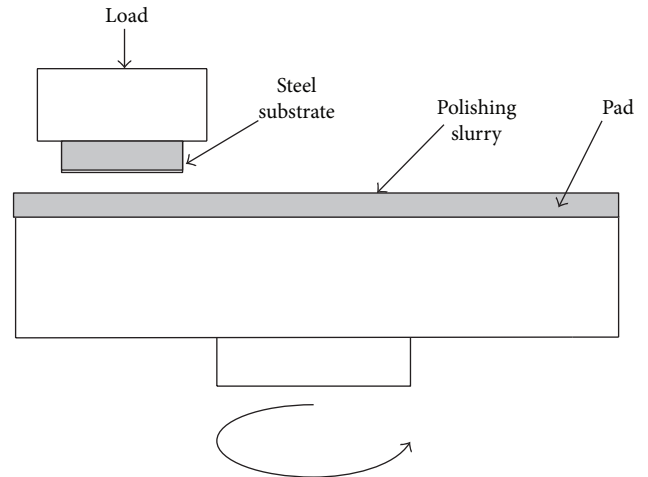
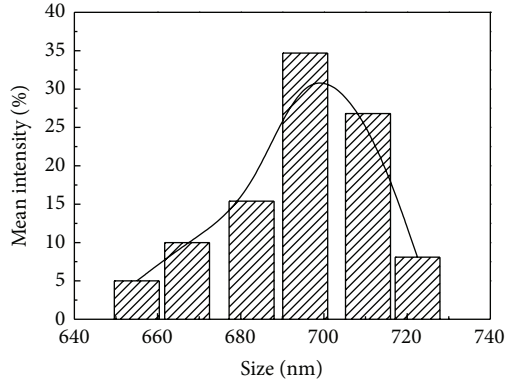
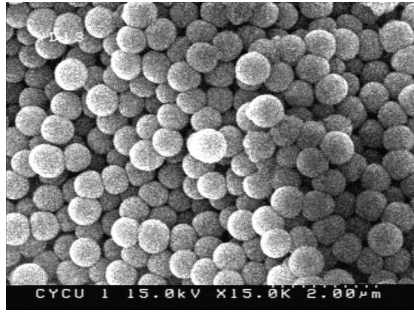
FIGURE 1: Experimental procedure for the synthesis of SiO<sub>2</sub> nanoparticles using sol-gel method.

FIGURE 2: Schematic representation of the CMP.

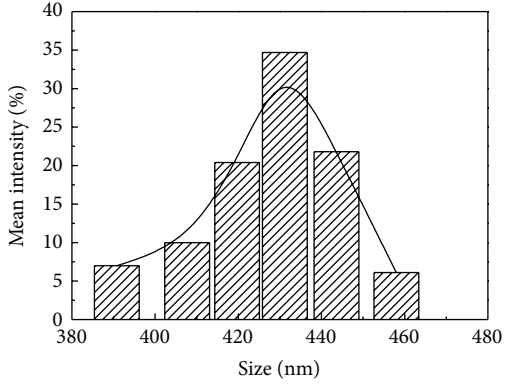
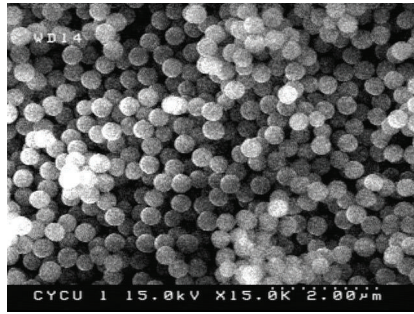
TABLE 2: CMP test conditions.

Down force (N)	20
Down pressure (N/cm <sup>2</sup> )	0.52
Table speed (rpm)	200
Polishing time (min)	20
Slurry flow rate (mL/min)	100

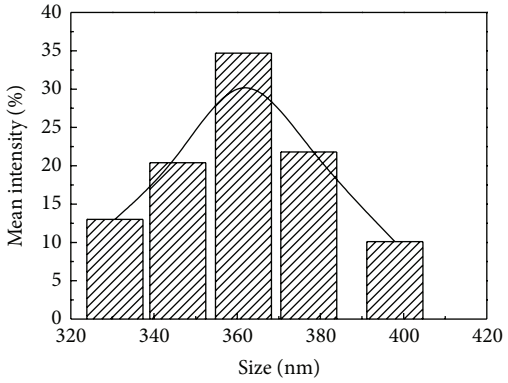
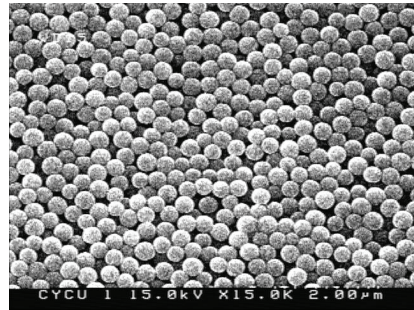
the uniform distribution of their sizes and their spherical shape. Figure 3 shows the distribution diagram, 684 nm, 420 nm, 362 nm, 215 nm, 140 nm, and 58 nm, which almost showed narrow size distribution. The composition of SiO<sub>2</sub> nanoparticles was qualitatively analyzed by EDS presented



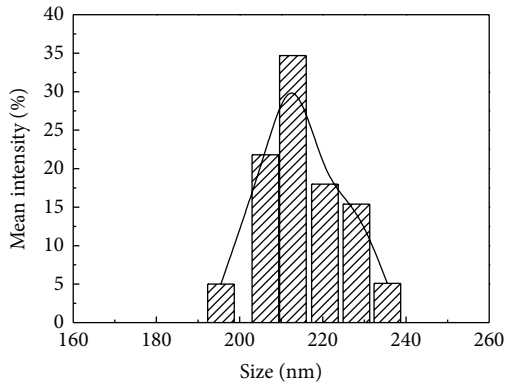
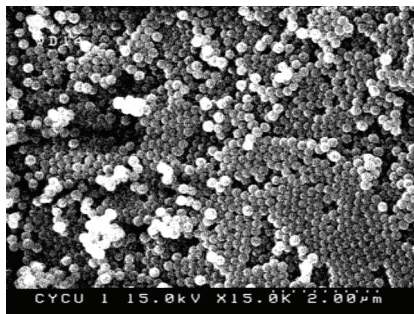
(a) 684 nm



(b) 420 nm



(c) 362 nm



(d) 215 nm

FIGURE 3: Continued.

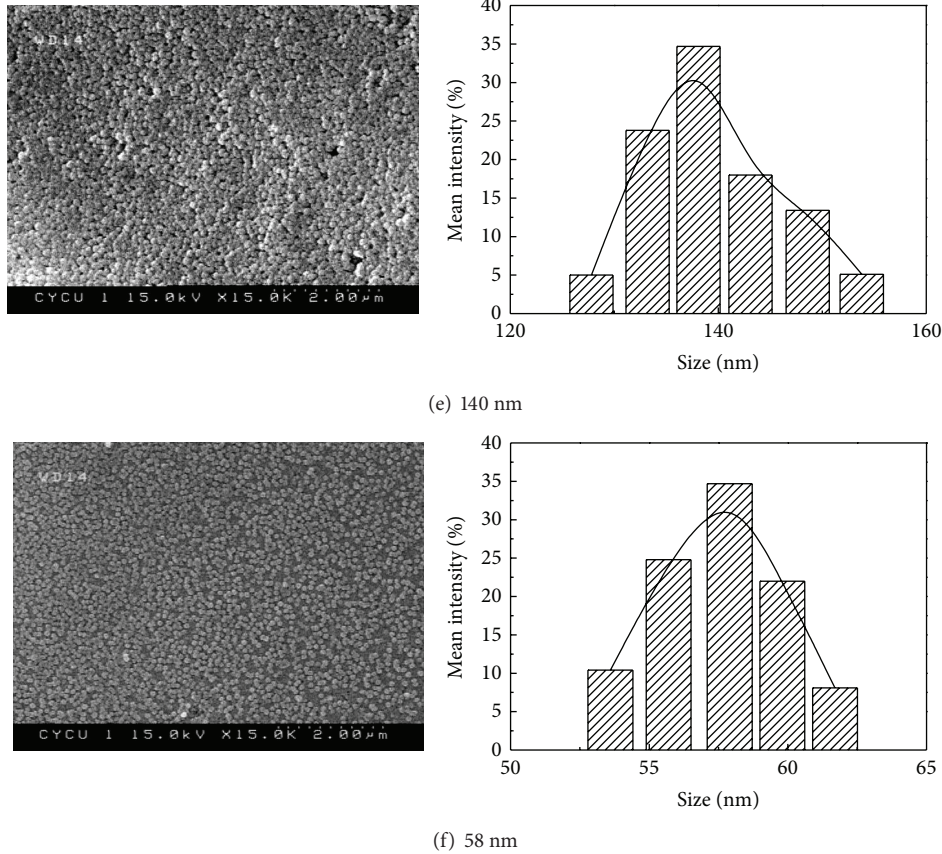


FIGURE 3: SEM micrographs and size distribution of SiO<sub>2</sub> nanoparticles.

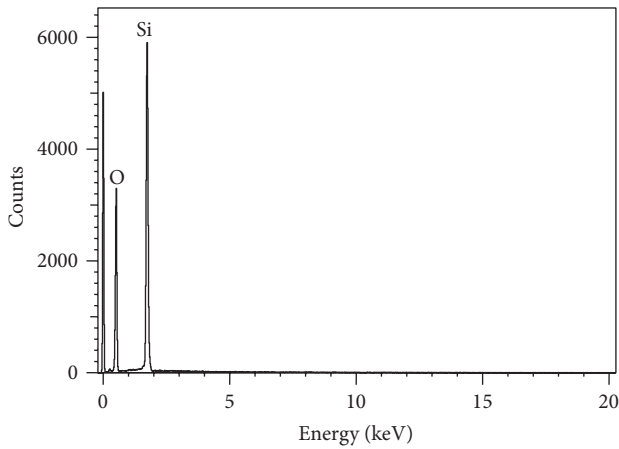


FIGURE 4: EDS spectrum of the SiO<sub>2</sub> nanoparticles.

in Figure 4. The nanoparticles are clearly composed of Si and O elements. No other elements were present in the SiO<sub>2</sub> nanoparticles. Therefore, SiO<sub>2</sub> nanoparticles can be effectively synthesized through the sol-gel method.

**3.2. Morphology and Roughness of Polished Steel Substrate Surface.** In chemical mechanical polishing of surfaces, abrasives are critical. As precisely controlled, stable distribution

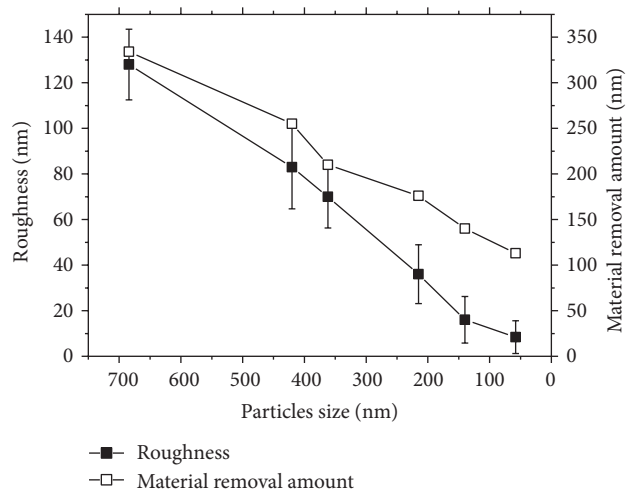
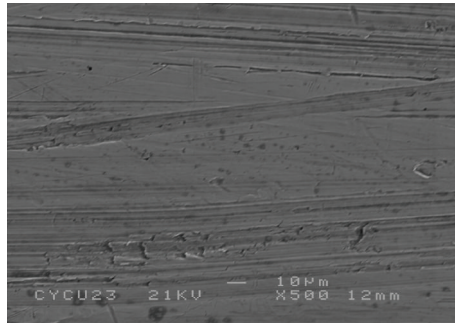
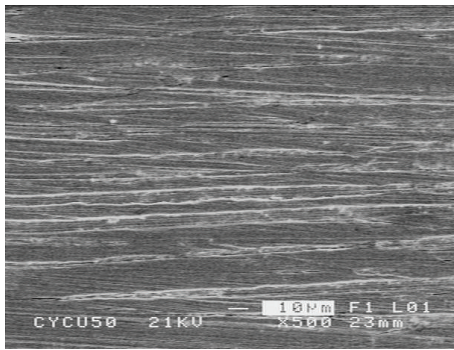


FIGURE 5: The roughness of steel substrates surfaces and the material removal amount with various sizes of slurries of silica particles.

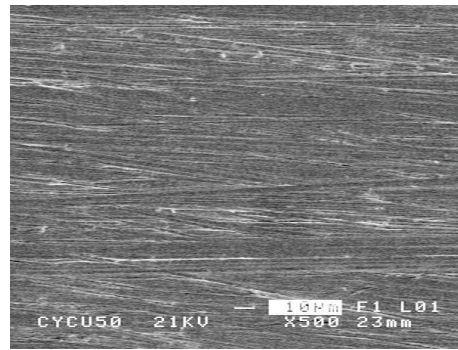
of particle sizes is a key contributor to maintaining low defect levels. Figure 5 presents the roughness of surfaces of steel substrates that were polished with slurries of silica particles of various sizes, dispersed in 2 wt.% H<sub>2</sub>O<sub>2</sub> and DI water. The effect of the particle size on the roughness of a polished



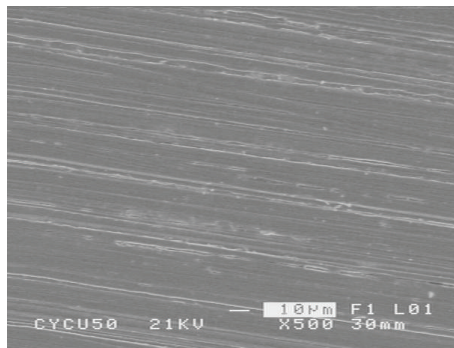
(a) Before polishing



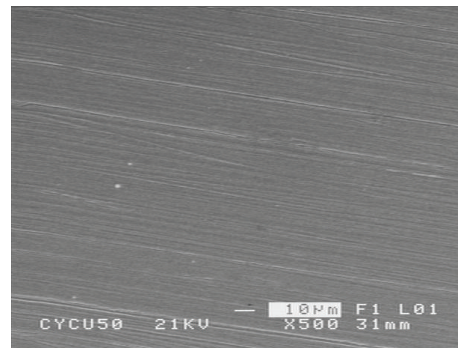
(b) 684 nm



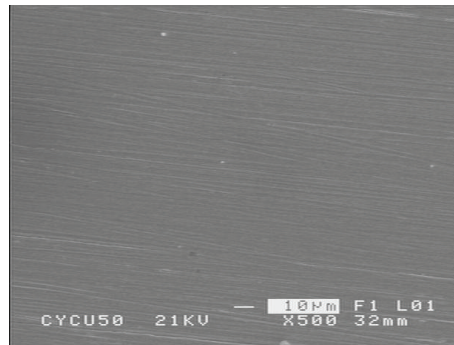
(c) 420 nm



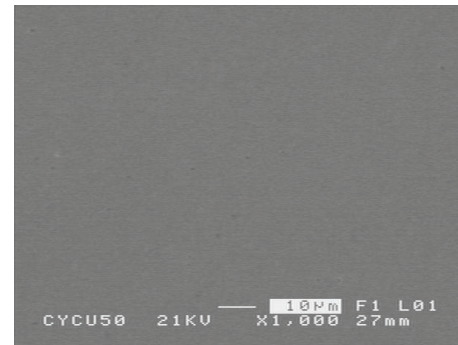
(d) 362 nm



(e) 215 nm



(f) 140 nm



(g) 58 nm

FIGURE 6: Surface profiles of steel substrates polished in different slurries.

steel substrate surface was evaluated through silica with a fixed solid content (2 wt.%) under the conditions that were specified above. Figure 5 shows that the surface roughness is 128 nm with the polished particles diameter of 684 nm and that it declined rapidly to 16 nm with 140 nm. In addition, it is 8.4 nm with up to 58 nm.

Figure 5 presents that the use of big SiO<sub>2</sub> particles made the roughness of steel substrate surface and the amount of removal material in CMP bigger. On the contrary, the use of small SiO<sub>2</sub> particles made the roughness of steel substrate surface and the amount of removal material in CMP smaller. The big SiO<sub>2</sub> particles possess more cutting. Cutting had a strong impact on bigger roughness of steel substrate surface as well as bigger amount of removal material. The amount of removal materials lowered down with the decreasing size of SiO<sub>2</sub> particle.

Large-sized SiO<sub>2</sub> causes larger cutting depth. The main mechanism is removal of material. Since the use of larger particles results in a more unequal distribution of the applied load on the surface of the steel substrate, it commonly results in the formation of defects. The reduction of nanosized SiO<sub>2</sub> particles made cutting depth decline rapidly. The reason why the material removed is plastic flowage. Finally, the smoothest surface with a roughness of 8.4 nm was obtained. [8].

The observed variation in the roughness of the polished material is attributed to two factors. (1) Indentation increases with particle size, increasing the roughness of the material, and (2) the number of particles per unit area between the substrate and the pad is reduced since the concentration is constant. Samples that are polished with slurries containing smaller particles are less rough because the indentations are shallower. Polishing with slurry that contains smaller abrasives effectively reduces microroughness and the thickness of the damaged layer that is formed by the abrasion.

**3.3. Observation of Polished Surface.** Figure 6 presents typical SEM images of the steel substrate surface before and after CMP. The surface before polishing is uneven and has many a large number of scratches (Figure 6(a)). The presence of larger particles in the CMP slurry increases the defect density and surface roughness of the polished steel substrate (Figures 6(b) and 6(c)). Polishing in the slurry with small abrasives (58 nm) makes the surface much smoother (Figure 6(g)) than an unpolished one (Figure 6(a)) with no observable scratches. The surface of the steel substrate becomes uniform and flat after it is polished for a long time, and the coarseness of the original surface is eliminated.

**3.4. CMP Process and Mechanism.** The CMP process involves a combination of chemical, mechanical, and hydrodynamic effects. Many models of material removal mechanisms during CMP have been proposed based on basic principles of polishing, contact mechanics, hydrodynamics, and abrasive wear mechanisms. Although there is a lack of a model of the entire CMP process, corrosion and abrasive wear may be agreed to be two basic effects of the material removal process [19].

Research reveals that CMP is a complex multiphased reaction process. It primarily involves the following two dynamics. First, the active component in the polishing slurry reacts with the atoms in the steel substrate; this step is an oxidation-reductive chemical reaction. Second, the new steel surface which is polished by slurry exposure after the resultant slowly separates from the surface. The abovementioned two steps determine the rate of material removal and completeness. Therefore, key means of influencing the two dynamic processes and related theory must be known before the degree of finishing and CMP can be effectively studied [20].

In this study, CMP reduced the uniformity of surface because the particles in the slurry that contained large abrasives had a wide size distribution. This result reveals that an optimal size of the abrasive in the slurry system that minimizes surface roughness exists. Based on the above process analysis, a new polishing mechanism that uses small abrasives, rapid reaction, and a rapid desorption is proposed. Polishing slurry with smaller abrasives yields a lower roughness and a thinner damaged layer. Therefore, control of the size of SiO<sub>2</sub> abrasive particles and the uniformity of the particle size distribution are important parameters in ensuring the uniformity of surfaces in the CMP process.

## 4. Conclusions

This study focuses on the effects of SiO<sub>2</sub> abrasives on polishing performance during CMP of a steel substrate. All in all, the polishing steel substrate was measured by CMP SiO<sub>2</sub> slurries. Their roughness reduced from 128 to 8.4 nm while the size of nanoparticles decreases from 684 to 58 nm. The material removal amount reduced from 334 to 113 nm as the size of nanoparticles decreases from 684 to 58 nm.

SiO<sub>2</sub> nanoparticles were prepared with the use of sol-gel method as CMP slurries. It could produce higher chemical purity and ultrafine particles with a narrow size distribution. SEM results reveal that CMP with these SiO<sub>2</sub> slurries yielded surfaces of high quality. Finally, the CMP mechanism of the steel substrate was determined.

## Conflict of Interests

The authors declare that there is no conflict of interests regarding the publication of this paper.

## References

- [1] Y. Ahn, J.-Y. Yoon, C.-W. Baek, and Y.-K. Kim, "Chemical mechanical polishing by colloidal silica-based slurry for micro-scratch reduction," *Wear*, vol. 257, no. 7-8, pp. 785-789, 2004.
- [2] D. G. Thakurta, S. Sundararajan, D. W. Schwendeman, S. P. Murarka, and W. N. Gill, "Two-dimensional wafer-scale chemical mechanical planarization models based on lubrication theory and mass transport," *Journal of the Electrochemical Society*, vol. 146, no. 2, pp. 761-766, 1999.
- [3] P. H. Chen, B. W. Huang, and H.-C. Shih, "A chemical kinetics model to explain the abrasive size effect on chemical mechanical polishing," *Thin Solid Films*, vol. 476, no. 1, pp. 130-136, 2005.

- [4] T. Y. Kwon, M. Ramachandran, and J. G. Park, "Scratch formation and its mechanism in chemical mechanical planarization (CMP)," *Friction*, vol. 1, no. 4, pp. 279–305, 2013.
- [5] D. W. Zhao and X. C. Lu, "Chemical mechanical polishing: theory and experiment," *Friction*, vol. 1, no. 4, pp. 306–326, 2013.
- [6] R. Lindberg, J. Sjöblom, and G. Sundholm, "Preparation of silica particles utilizing the sol-gel and the emulsion-gel processes," *Colloids and Surfaces A: Physicochemical and Engineering Aspects*, vol. 99, no. 1, pp. 79–88, 1995.
- [7] W. Stöber, A. Fink, and E. Bohn, "Controlled growth of monodisperse silica spheres in the micron size range," *Journal of Colloid and Interface Science*, vol. 26, no. 1, pp. 62–69, 1968.
- [8] M.-H. Oh, J.-S. Nho, S.-B. Cho, J.-S. Lee, and R. K. Singh, "Polishing behaviors of ceria abrasives on silicon dioxide and silicon nitride CMP," *Powder Technology*, vol. 206, no. 3, pp. 239–245, 2011.
- [9] Y.-J. Seo and W.-S. Lee, "Effects of different oxidizers on the W-CMP performance," *Materials Science and Engineering B: Solid-State Materials for Advanced Technology*, vol. 118, no. 1–3, pp. 281–284, 2005.
- [10] J. Larsen-Basse and H. Liang, "Probable role of abrasion in chemo-mechanical polishing of tungsten," *Wear*, vol. 233–235, pp. 647–654, 1999.
- [11] P. Zhang and H. Lei, "Preparation of alumina/silica core-shell abrasives and their CMP behavior," *Applied Surface Science*, vol. 253, no. 21, pp. 8754–8761, 2007.
- [12] N.-H. Kim, Y.-J. Seo, and W.-S. Lee, "Temperature effects of pad conditioning process on oxide CMP: polishing pad, slurry characteristics, and surface reactions," *Microelectronic Engineering*, vol. 83, no. 2, pp. 362–370, 2006.
- [13] Y. Xie and B. Bhushan, "Effects of particle size, polishing pad and contact pressure in free abrasive polishing," *Wear*, vol. 200, no. 1-2, pp. 281–295, 1996.
- [14] J. Luo and D. A. Dornfeld, "Effects of abrasive size distribution in chemical mechanical planarization: modeling and verification," *IEEE Transactions on Semiconductor Manufacturing*, vol. 16, no. 3, pp. 469–476, 2003.
- [15] G. B. Basim, J. J. Adler, U. Mahajan, R. K. Singh, and B. M. Moudgil, "Effect of particle size of chemical mechanical polishing slurries for enhanced polishing with minimal defects," *Journal of the Electrochemical Society*, vol. 147, no. 9, pp. 3523–3528, 2000.
- [16] L. Zhong, J. Yang, K. Holland et al., "A static model for scratches generated during aluminum chemical-mechanical polishing process: orbital technology," *Japanese Journal of Applied Physics*, vol. 38, no. 4, pp. 1932–1938, 1999.
- [17] T. Satoh, M. Akitaya, M. Konno, and S. Saito, "Particle size distributions produced by hydrolysis and condensation of tetraethylorthosilicate," *Journal of Chemical Engineering of Japan*, vol. 30, no. 4, pp. 759–762, 1997.
- [18] L. Zhao, J.-G. Yu, B. Cheng, and X.-J. Zhao, "Preparation and formation mechanisms of monodispersed silicon dioxide spherical particles," *Huaxue Xuebao*, vol. 61, no. 4, pp. 562–566, 2003.
- [19] H. Lei and J. Luo, "CMP of hard disk substrate using a colloidal SiO<sub>2</sub> slurry: preliminary experimental investigation," *Wear*, vol. 257, no. 5-6, pp. 461–470, 2004.
- [20] Y. Liu, K. Zhang, F. Wang, and W. Di, "Investigation on the final polishing slurry and technique of silicon substrate in ULSI," *Microelectronic Engineering*, vol. 66, no. 1–4, pp. 438–444, 2003.

## Research Article

# Novel Method for Floating Synthesizing Heavy Metal Particles as Floating Anode of Zinc-Air Fuel Cell

Chen Yang Wu,<sup>1</sup> Kuohsiu David Huang,<sup>1</sup> and Horng Yi Tang<sup>2</sup>

<sup>1</sup> Department of Vehicle Engineering, National Taipei University of Technology, Taipei 10608, Taiwan

<sup>2</sup> Department of Applied Chemistry, National Chi Nan University, Nantao 54561, Taiwan

Correspondence should be addressed to Chen Yang Wu; [calvintp@ms61.hinet.net](mailto:calvintp@ms61.hinet.net)

Received 16 September 2013; Revised 9 December 2013; Accepted 7 January 2014; Published 6 March 2014

Academic Editor: Ho Chang

Copyright © 2014 Chen Yang Wu et al. This is an open access article distributed under the Creative Commons Attribution License, which permits unrestricted use, distribution, and reproduction in any medium, provided the original work is properly cited.

In this study, centrally hollow microspheres of zinc were synthesized. The microspheres were then mixed with KOH electrolyte to form zinc sol, which was coagulated and precipitated. Afterward, we employed a novel technique to enable the permanent floating of zinc particles, which involved stirring zinc sol with air using a magnetic stirrer. This resulted in the formation of foam in which the zinc particles permanently floated. We then added 65 wt% of the electrolyte (KOH) to prepare 35 wt% of zinc sol. We tested the cell and found the values of current density, specific energy, and electric capacity to be 7.41 mA/cm<sup>2</sup>, 840.14 Wh/kg, and 3023 mAh, respectively.

## 1. Introduction

Currently, the technologies used for shale oil refining, methane clathrate mining, and oil excavation in the melting waters of the Arctic Ocean are being widely promoted. However, horizontal drilling and hydraulic fracturing could trigger earthquakes and pollute the groundwater. Also, the emissions resulting from burning oil, hydrocarbons, CO, CO<sub>2</sub>, and NO<sub>x</sub> pollute the environment and amplify the greenhouse effect, thereby increasing the likelihood of global disasters [1].

The zinc-air fuel cell could be a source of clean energy owing to its simplicity, high efficiency, high energy density, high power density, low operating temperature, low cost, and environment friendliness.

In this study, we began with feeding the fuel manually into the zinc-air fuel cell. However, we soon realized that if we wanted to feed the fuel continuously, the anode would have to be modified from a solid state to a fluid state. Therefore, it was necessary that the zinc particles float.

In 2001, Colborn and Smedley proposed the concept of a zinc-air fuel cell system and single fuel cell management [2]. In their single fuel cell, the zinc pellets were introduced on the top of the zinc electrode, and then circulated in the electrolyte using a pump. The air was blown using a blower into the electrolyte in a top-down manner (Figure 1).

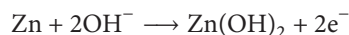
In our study, the zinc particles, which were mixed with the KOH electrolyte, were aggregated and precipitated. The aggregation increased with the increasing concentration of KOH.

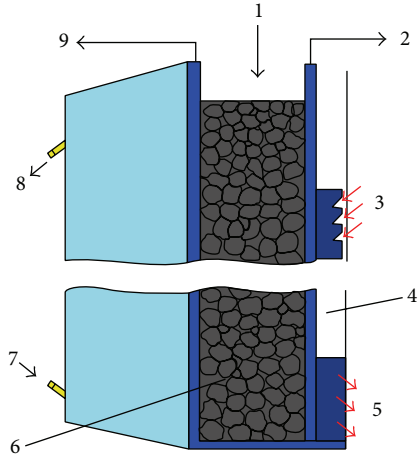
The micelle technology was used to generate chemical particles whose sizes were consistent with those of the polymer microspheres. Next, the chemical modification of the surface functional groups afforded the reduction and hence deposition of the silver and zinc particles on the surface of the microspheres.

We mixed the microspheres with the electrolyte to form zinc sol, which was then floated and flown through a porous current collector using an electrolyte circulation system, thus resulting in a fluid anode. By incorporating appropriate fuel fluidity and current collection, the design and performance of the zinc-air fuel cell were improved.

## 2. Working Principle

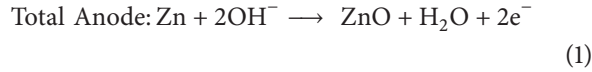
In the zinc-air fuel cell, the zinc metal is oxidized, releasing chemical energy in the form of electrical energy [3]. The anode reaction is as follows:





- |  |                                   |
|--|-----------------------------------|
| (1) Zinc pellets introduced into top of zinc electrode | (6) Zinc electrode (zinc pellets) |
| (2) Positive terminal                                  | (7) Electrolyte in                |
| (3) Air inlet from air blower                          | (8) Electrolyte out               |
| (4) Air electrode                                      | (9) Negative terminal             |
| (5) Air outlet   |                                   |

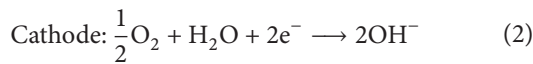
FIGURE 1: Metallic power company cell.



$$E^0 = 1.25 \text{ V.}$$

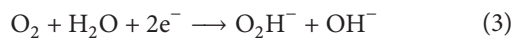
The existence of zincate species containing  $\text{Zn}^{2+}$  such as  $\text{ZnO}$ ,  $\text{Zn(OH)}_2$ ,  $\text{ZnO}_2^{2-}$ , and  $\text{Zn(OH)}_4^{2-}$  depends on the temperature and concentration of  $\text{OH}^-$  and supersaturation of zincate.

The oxygen can be reduced to hydroxyl ions according to the following reaction:

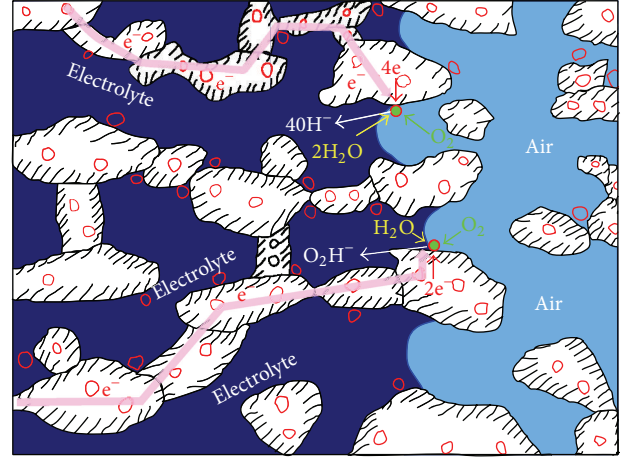


$$E^0 = 0.40 \text{ V.}$$

However, direct electrochemical (four-electron) reduction to hydroxide ions described in (2) will occur only in the presence of special catalysts. In the absence of such a catalyst (e.g., on the surface of carbon substrate), the electrochemical (two-electron) reduction to peroxide ions dominates as the cathodic reaction of the zinc-air battery, as shown in the following equation:



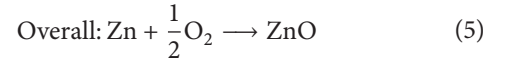
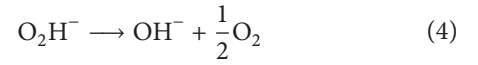
The resulting peroxide ions are generally unstable and get decomposed via the disproportionation reaction of oxygen to produce hydroxide ions and molecular oxygen, as shown



- |                        |                      |
|------------------------|----------------------|
| — Air/fuel             | ◇ Catalyst/activator |
| — Electrolyte/solution | ● 3-phase interface  |
| ▨ Carbon/conductor     |                      |

FIGURE 2: Three-phase interface within catalyst of zinc-air fuel cell.

in (4). The schematic of the catalytic reaction involving interactions with three phases is shown in Figure 2 [4],



$$E^0 = 1.65 \text{ V.}$$

The reaction schemes are shown in Figures 3 and 4.

The equation pertaining to the conversion of chemical energy to electrical energy is mentioned below:

$$E_r = \frac{-\Delta G}{nF}, \quad (6)$$

$$E = E^r - \eta_{\text{all}}$$

$E_r$ : voltage between anode and cathode,  $\Delta G$ : free energy change,  $n$ : electronic number,  $F$ : Faraday constant,  $E$ : discharge voltage, and  $\eta_{\text{all}}$ : overvoltage.

In general, in terms of the condition of overvoltage ( $\eta_{\text{all}}$ ), three phenomena are observed in zinc-air fuel cells: activation overvoltage, concentration overvoltage, and ohmic overvoltage. These three phenomena also serve as the best standards to determine the quality of cells (Table 1).

According to the IUPAC definition, a colloidal particle retains its properties within the range 1–1000 nm in the three-dimensional space.

The solution of colloidal particles (dispersed phase) dispersed in a solvent molecule (dispersion medium) is called a colloidal solution. A colloidal dispersion solution is depicted in Table 2 [5].

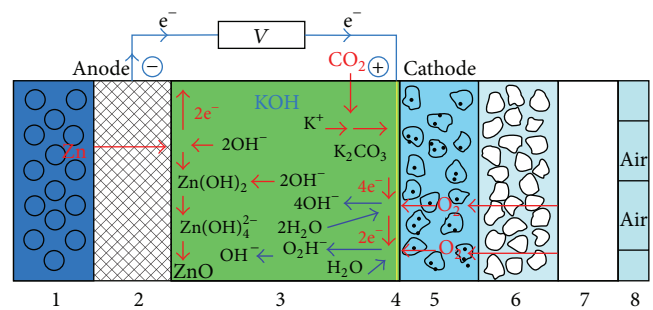
Sol phenomenon: collisions due to the thermal motion of the solvent molecules containing the particles result in an

TABLE 1: Causes of three types of overvoltage and their solutions.

	Cause	Solution
Activation overvoltage	If $\text{HO}_2^-$ ions are absorbed on the electrode surface, the reaction mechanism by which $\text{O}_2$ changed to $\text{OH}^-$ ions will slow down. This leads to activation polarization and results in activation overvoltage	Elevate the temperature of a cell, as well as the reaction speed of three-phase boundaries
Concentration overvoltage	Because of poor gas diffusion, $\text{O}_2$ supply in the reaction becomes too slow; as a result, $\text{O}_2$ concentration becomes insufficient. This causes concentration polarization and results in concentration overvoltage	Elevate the flow speed of $\text{O}_2$ at the anode and increase the $\text{O}_2$ concentration
Ohmic overvoltage	Because of improper design, poor conductivity of electrolytes or impurities in the electrodes increasing resistance to current flow, ohmic polarization may occur, resulting in ohmic overvoltage	Use electrode materials and electrolytes with higher conductivity

TABLE 2: Types of colloidal dispersion.

Dispersed phase	Dispersion medium	Name
Solid	Solid	Solid suspension
Solid	Liquid	Sol, colloidal suspension; paste (high solid concentration)
Solid	Gas	Solid aerosol
Liquid	Solid	Solid emulsion
Liquid	Liquid	Emulsion
Liquid	Gas	Liquid aerosol
Gas	Solid	Solid foam
Gas	Liquid	Foam



- (1) Zinc powder
- (2) Current collector net
- (3) KOH
- (4) U-type current collector slice
- (5) Catalyst layer
- (6) Diffusion layer
- (7) PTFE layer
- (8) Atmosphere

FIGURE 4: Reaction schematic of zinc-air fuel cell.

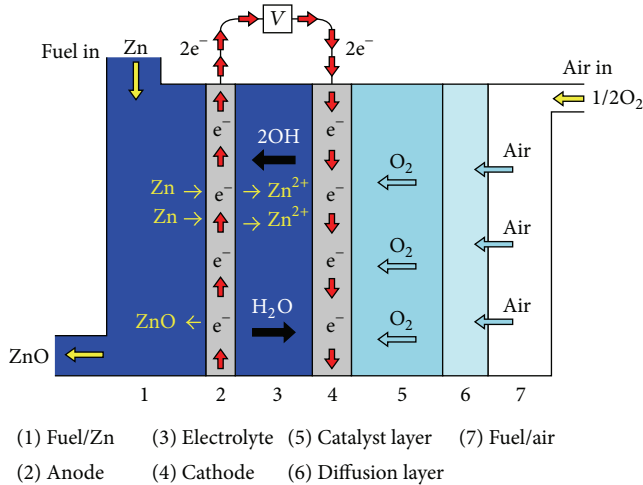


FIGURE 3: Working schematic of zinc-air fuel cell.

uneven force in all directions. Therefore, a Brownian movement is created, which results in the coagulation of colloids.

The colloidal particles in the electrolyte solution or such other polar solution undergo mechanisms such as ionization, ion adsorption, and ion dissolution to generate surface charges. This attracts the adjacent, oppositely charged ions (counter-ion) in the solution to the particle surface and repels

ions with the same charge (coion) away from the particle surface.

Therefore, the condition of charge distribution from the surface of the colloidal particles to the solution is called electric double layer.

Because of Brownian motion, colloidal particles undergo successive collisions with other particles.

- (1) If the repulsion between the particles is smaller than the force of gravity, the particles, after colliding with each other, will permanently integrate and form collectives. This phenomenon of precipitation of colloidal particles is called coagulation.
- (2) If the repulsion between the particles is larger than gravity, the particles, after colliding with each other, will remain dispersed in the solution in an individual state. Such colloidal particles remain suspended in the solution [6, 7].

When the particle diameter is  $<5 \mu\text{m}$ , it will be influenced by the Brownian motion.

Because charged colloidal particles in suspension repel each other through the electric double layer, they can stably float in solution without coagulation. If a salt-based electrolyte is added to the solution, it will destroy the electric

double layer and reduce the electric repulsion between the particles, thereby coagulating the colloidal particles [8–10].

The colloidal stability is determined by the electrostatic repulsion and van der Waals forces between the particles [11].

The van der Waals force  $F_v$ :

$$F_v = \frac{k_v r}{16\pi R^2} \quad (7)$$

$F_v$ : van der Waals force,  $k_v$ : van der Waals constant,  $r$ : particle radius, and  $R$ : distance between two particles.

### 3. Experimental

**3.1. Precipitation of Zinc Particles.** The critical barriers for establishing a fluid electrode include precipitation of zinc particles, cluster aggregation of the zinc paste, and congestion of the current collector.

We attempted to float the zinc particles using dispersants carboxymethyl cellulose (CMC), polyvinyl alcohol (PVA), and polyacrylic acid sodium (PAAS), but in vain.

- (1) When only zinc particles were mixed with water, the dispersion of zinc (fluid effect) was achieved. The flowing time was very short; for a short time interval, no stirring was carried out. As a result, although the precipitation of zinc started, it did not cascade to aggregation. On the other hand, when the zinc particles were added to water containing KOH, zinc particles showed significant aggregation and thus precipitation, which increased with the increasing concentration of KOH.
- (2) Then, 30 wt% zinc powder was mixed with 30 wt% KOH electrolyte; as a result, aggregation and precipitation occurred.
- (3) Next, 20 wt% KOH was mixed with 3 wt% CMC, followed by mixing with 30 wt% zinc; as a result, there was significant aggregation followed by precipitation.
- (4) Subsequently, 20 wt% KOH was mixed with 3 wt% PVA, followed by mixing with 30 wt% zinc; as a result, there was significant aggregation followed by precipitation.
- (5) Finally, 20 wt% KOH was mixed with 3 wt% PAAS and then added to 30 wt% zinc; as a result, there was neither aggregation nor precipitation. However, as the KOH concentration was increased to 30 wt%, the effect of zinc was completely lost because all the zinc particles settled at the bottom (sedimentation), and aggregation did not occur.

Floating test of centrally hollow zinc microspheres.

Surfactants are amphiphilic compounds. Their molecular structure mainly comprises hydrophilic groups (polar or ionic moieties) and hydrophobic groups (nonpolar hydrocarbon chains).

When the concentration of the surfactant in the solution is very low, it is usually present in the monomeric form. On the other hand, when the concentration of the surfactant is increased to saturation, the surfactant molecules aggregate

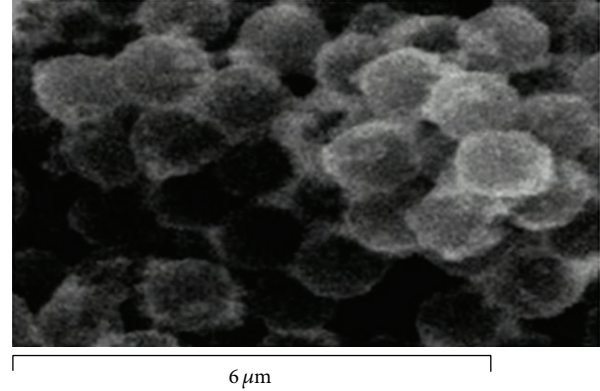


FIGURE 5: Scanning electron microscopy image of polystyrene/Ag microspheres.

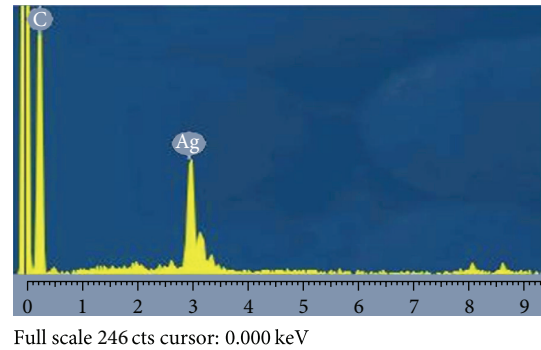


FIGURE 6: Energy-dispersive X-ray spectral analysis of polystyrene/Ag microspheres.

(tens to hundreds). The hydrophilic ends are in contact with the water molecules outwardly; such aggregates are referred to as “micelles.” When the micelles are formed, the concentration of the surfactant is called the “critical micelle concentration” (CMC).

When the surfactant was added to a water-oil system, the surface tension was reduced to about  $1 \text{ mNm}^{-1}$ , and the resulting micelle size was about  $100 \text{ \AA}$ . With such a dimension,  $\Delta S$  and  $\Delta A$  were large, but surface tension  $\gamma$  was small. However, the free energy was less than 0 ( $\Delta G < 0$ ). This indicated that the micelles were thermodynamically stable [12, 13]. By using the Gibbs free energy, we obtain the following relation:

$$\Delta G = \gamma \Delta A - T \Delta S \quad (8)$$

$T$ : temperature,  $A$ : area,  $S$ : entropy, and  $\gamma$ : surface tension.

We synthesized the centrally hollow zinc microspheres by employing the micelle technology on the zinc particles as follows [14]:

- (1) micelle emulsion microspheres  $\rightarrow$  nanopolymer microspheres;
- (2) surface modification using functional groups  $\rightarrow$  polystyrene microspheres;

TABLE 3: The experimental parameters and data of constant current electrolysis.

	Original weight (g)	After electrolysis weight (g)	Electrolysis voltage (V)	Electrolysis current (A)	Electrolysis time (min)	Stir (Y/N)	Current efficiency (%)
Sample 1	0.9323	0.9679	2.3	0.03	5	Y	0.3242
Sample 2	0.9441	0.9466	2.2	0.03	3	Y	0.0379
Sample 3	1.0618	1.0875	2.6	0.06	5	Y	0.1170
Sample 4	1.0257	1.0634	2.3	0.03	5	N	0.3434

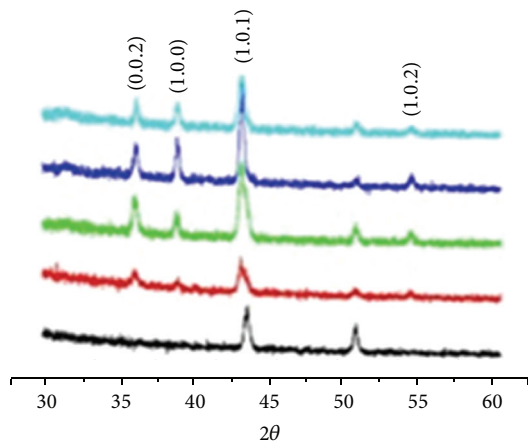


FIGURE 7: X-ray diffraction patterns of zinc metal precipitation by flow electrolysis. (a) Background, black. (b) Sample 1, red. (c) Sample 2, green. (d) Sample 3, blue. (e) Sample 4, light blue. (Unindexed peaks mean steel background signal.)

- (3) (i) current electrolysis → centrally hollow zinc metal microspheres,  
(ii) spray granulation → centrally hollow zinc metal microspheres.

The steps can be elucidated as follows.

*Step 1.* Synthesis of polystyrene (PS) microspheres using micelle technology.

*Step 2.* Surface modification by functional groups involving silver mirror reaction (PS + Ag) (Figures 5 and 6).

*Step 3.* (i) Current electrolytic zinc metal making centrally hollow zinc metal microspheres (PS + Ag + Zn) (Figures 7, 8, and 9).

The experimental parameters and data of constant current electrolysis are shown in Table 3.

(ii) Spray deposition of zinc metal making centrally hollow zinc metal microspheres (PS + Ag + Zn) (Figure 10).

#### 4. Results and Discussion

After forming the zinc particles using the micelle technology, we synthesized the centrally hollow zinc microspheres. These were then mixed with the KOH electrolyte to form the zinc sol, which coagulated and precipitated, at least initially. As the concentration of the electrolyte increased, the zinc particles became more prone to precipitation [15]. The results of the

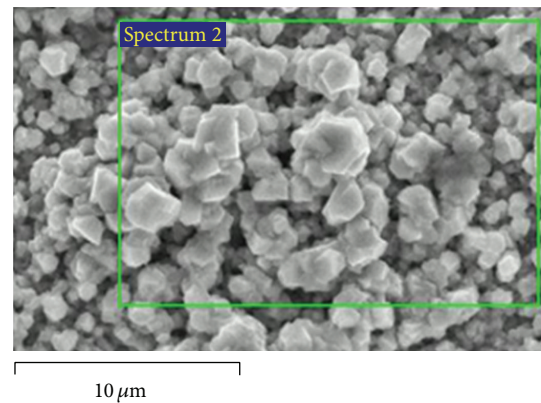


FIGURE 8: Scanning electron microscopy image of sample 1 plated layer.

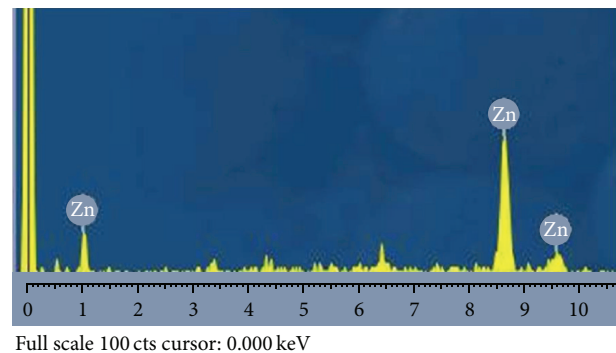


FIGURE 9: Energy-dispersive X-ray spectrum composition analysis of local region.

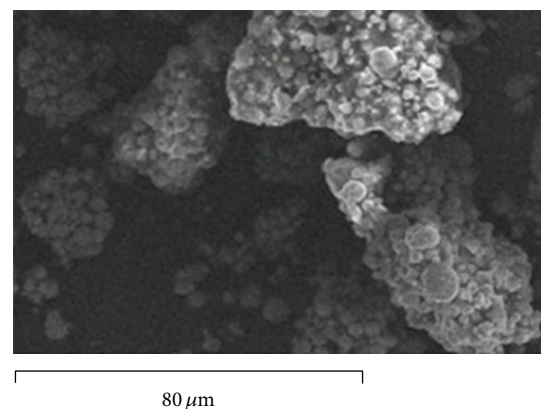


FIGURE 10: Scanning electron microscopy image with 750x magnification.

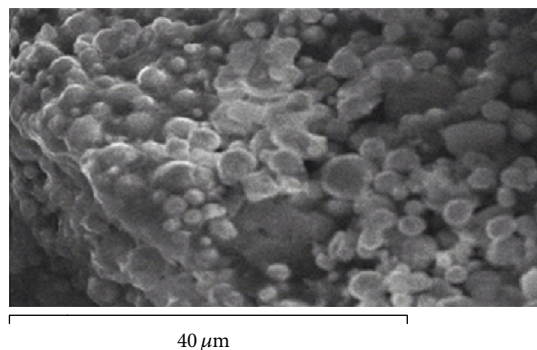


FIGURE 11: Scanning tunneling microscopy image of zinc sol.



FIGURE 12: Successful floating of zinc sol.

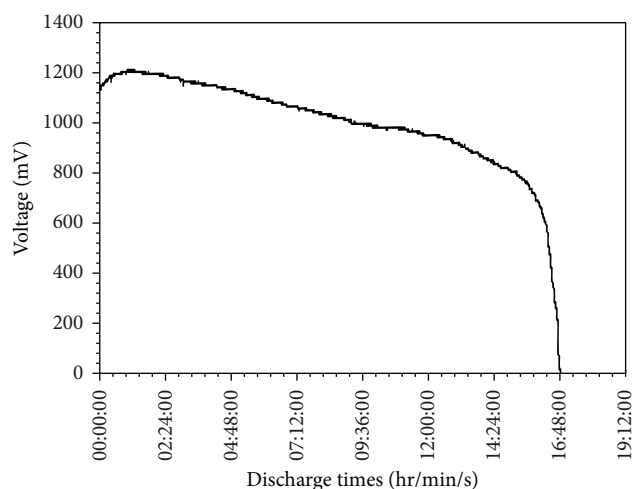


FIGURE 13: Voltage curve of 35 wt% zinc sol under a constant-current discharge at 200 mA.

scanning tunneling microscopy (STM) studies are shown in Figure 11.

Next, we added air into the zinc sol, and stirred the mixture using a magnetic bar. As a result, the zinc sol gradually foamed like a milkshake, thus enabling the permanent floating of the zinc particles [15, 16] (Figure 12).

We added 65 wt% of the electrolyte to prepare 35 wt% of the zinc sol. The cell, as Figure 13 shows, was tested under a constant-current discharge at 200 mA. The values of current density, specific energy, and electric capacity were found to be  $7.41 \text{ mA/cm}^2$ ,  $840.14 \text{ Wh/kg}$ , and  $3023 \text{ mAh}$ , respectively [15].

## 5. Conclusions

The critical barriers in the preparation of fluid electrodes are coagulation and precipitation of zinc particles, floating zinc particles, flowing of zinc particles, and congestion of the current collector. We addressed these challenges by employing micelle technology to prepare the centrally hollow zinc microspheres and then successfully floated the zinc sols by stirring with a magnetic bar. In this study, the zinc sol was allowed to flow through a porous current collector using an electrolyte circulation system. The results showed that the electrolyte circulation system correctly regulated the internal temperature of the cell, dynamically adjusted the concentration of KOH, and removed the impurities from the electrolyte to help maintain its optimal condition. Through the use of appropriate fuel fluidity and current collection, the design and performance of zinc-air fuel cells could be enhanced.

## Conflict of Interests

The authors declare that there is no conflict of interests regarding the publication of this paper.

## Acknowledgments

The financial support for this study was provided by the National Science Council of the Republic of China under the Project no. NSC-95-2218-E-260-001 NSC-95-2218-E-027-006. The authors thank the support of the Department of Applied Chemistry, National Chi Nan University, Taiwan.

## References

- [1] F. Simon, "Marketing green products in the trial," *Columbia Journal of World Business*, pp. 269–285, 1992.
- [2] J. Colborn and S. Smedley, "Ultra-long duration backup for telecommunications applications using zinc/air regenerative fuel cells," in *Proceedings of the 23rd International Telecommunications Energy Conference*, pp. 576–581, October 2001.
- [3] C. Chakkaravarthy, A. K. A. Waheed, and H. V. K. Udupa, "Zinc-air alkaline batteries—a review," *Journal of Power Sources*, vol. 6, no. 3, pp. 203–228, 1981.
- [4] H. Arai and M. Hayashi, "Primary batteries - aqueous system zinc-air," *Encyclopedia of Electrochemical Power Sources*, pp. 55–61, 2009.
- [5] D. J. Shaw, *Introduction to Colloid and Surface Chemistry*, Butterworth-Heinemann, 4th edition, 1992.
- [6] J. Gregory, "Rates of flocculation of latex particles by cationic polymers," *Journal of Colloid and Interface Science*, vol. 42, no. 2, pp. 448–456, 1973.
- [7] J. Gregory, "The effect of cationic polymers on the colloidal stability of latex particles," *Journal of Colloid and Interface Science*, vol. 55, no. 1, pp. 35–44, 1976.

- [8] N. Schamp and J. Huylebroeck, "Adsorption of polymers on clays," *Journal Polymer Science, Part C*, no. 42, pp. 553–562, 1974.
- [9] W. Stumm and J. J. Morgan, "Chemical aspects of coagulation," *Journal American Water Works Association*, vol. 54, no. 8, pp. 971–994, 1962.
- [10] J. Gregory, "Stability and flocculation of colloidal particles," *Effluent and Water Treatment Journal*, vol. 17, pp. 515–521, 1977.
- [11] E. J. W. Verwey and J. T. G. Overbeek, "Theory of the stability of lyophobic colloids," *Journal of Colloid Science*, vol. 10, no. 2, pp. 224–225, 1955.
- [12] W. H. Zhu, B. A. Poole, D. R. Cahela, and B. J. Tatarchuk, "New structures of thin air cathodes for zinc-air batteries," *Journal of Applied Electrochemistry*, vol. 33, no. 1, pp. 29–36, 2003.
- [13] G. Savaskan, T. Huh, and J. W. Evans, "Further studies of a zinc-air cell employing a packed bed anode part I: discharge," *Journal of Applied Electrochemistry*, vol. 22, no. 10, pp. 909–915, 1992.
- [14] H. Y. Tang, *Zinc-Air Fuel Cell Power Systems R & D—Research of Central-Hollow Zinc Powder and Current Collector*, National Science Council, the Republic of China, 2007.
- [15] K. D. Huang, C. Y. Wu, and J. S. Li, *Zinc-Air Fuel Cell Power Systems R & D—Air-Flow, Electrolyte and Thermal Management*, National Science Council, the Republic of China, 2007.
- [16] W. M. Lu, R. Q. Xu, and H. Z. Wu, *Technology of Liquid Stired*, Chemical Engineering, Gau Lih Book, 2008.

## Research Article

# Effect of Polarization Fatigue on Harvesting Energy Using Pyroelectric Materials

**Saber Mohammadi**

*Mechanical Department, Razi University, Kermanshah 6714967346, Iran*

Correspondence should be addressed to Saber Mohammadi; [saberm7@yahoo.com](mailto:saberm7@yahoo.com)

Received 13 May 2013; Accepted 11 January 2014; Published 25 February 2014

Academic Editor: Ching-Song Jwo

Copyright © 2014 Saber Mohammadi. This is an open access article distributed under the Creative Commons Attribution License, which permits unrestricted use, distribution, and reproduction in any medium, provided the original work is properly cited.

The phenomenon of polarization fatigue in ferroelectric materials is defined and the effect of this phenomenon on harvested energy using these materials has been studied. In order to illustrate this effect, the harvested energy using PZN-4.5PT single crystal was compared in two cases of fatigued and nonfatigued samples. The results have been calculated between two temperatures of 100 and 130°C using Ericsson thermodynamic cycle.

## 1. Introduction

Ferroelectrics have been the particular popular materials of research for several decades due to their excellent properties which offer potential for development of many modern technological devices, such as microactuators, sensors, and transducers [1–6]. But further studies are necessary to improve the long-time reliability of these devices. A limiting problem to extensive use of ferroelectrics is the suppression of switchable polarization, after certain number of AC drive cycles [5–8]. This is called the polarization fatigue and popularly observed by polarization-electric field (P-E) hysteresis loop measurements. Fatigue in the ferroelectric capacitor corresponds to a decrease of the switchable polarization as a result of bipolar electric field cycling and has been phenomenologically described by many authors [6, 9–12]. Indeed, polarization in a ferroelectric material is a function of the applied electric field cycle's numbers. Electric field cycling continuously reversing the polarity of the dipoles induces certain changes in a ferroelectric and alters the P-E hysteresis loop. The experimental results on the electrothermal and fatigue characterization of the lead-zirconate-titanate ceramic,  $\text{PbZr}_{0.53}\text{Ti}_{0.47}\text{O}_3$  (PZT-5H), for actuator applications have been presented in [13]. Also, fatigue effects due to unipolar cycling of a bulk lead-zirconate-titanate were demonstrated in [14]. Furthermore, polarization and strain hysteresis (P-E and S-E) measurements have been performed

simultaneously during fatigue tests under AC fields with a triangular wave form [15].

In the present work, the PZN-4.5PT single crystal that has remarkable pyroelectric properties has been used. Pyroelectric effect converts thermal energy into the electrical current or voltage [16]. This thermal energy can come from many different sources such as ambient temperature, human body temperature, solar energy, and other temperatures of environment. This material possesses several phase changes in the vast range of temperature variations [17]. When the phase change occurred, the sudden increase in current and consequently in polarization is observed. Khodayari et al. [17] show that the phase change increases the harvested energy. Also, it was shown that the results of modeled Ericsson cycle have compatibility with the experimental Ericsson cycle. They measured the value of  $216.5 \text{ mJ/cm}^3$  under phase transition using PZN-4.5PT material on the application of Ericsson thermodynamic cycle at 100 and 160°C. This energy has been calculated on the application of 2 KV/mm electric field. Guyomar et al. [18] studied the possibilities of harvesting energy from PVDF (polyvinylidene fluoride) film using pyroelectric effect. Materials with high pyroelectric activity or those exhibiting a transition can be used for energy harvesting by converting thermal energy into electrical energy. In this paper, the effect of polarization fatigue on the harvested energy will be studied using modeled thermodynamic Ericsson cycle.

## 2. Pyroelectric Thermodynamic Conversion

The constitutive equations to describe pyroelectric material are [19]

$$\begin{aligned} dD &= \epsilon dE + p dT, \\ d\Gamma &= p dE + \frac{\rho c}{T_0} dT, \\ p &= \left( \frac{dD}{dT} \right), \quad c = \left( \frac{dU}{dT} \right), \end{aligned} \quad (1)$$

where  $D$ ,  $E$ ,  $T$ ,  $\Gamma$ ,  $\rho$ ,  $p$ ,  $U$ ,  $\epsilon$ , and  $c$  are the electric displacement, electric field, temperature, entropy, mass density, pyroelectric coefficient, internal energy, dielectric coefficient, and thermal capacity, respectively. In order to harvest energy the Ericsson thermodynamic cycle has been used which consists of two constant electric fields and two isothermal processes. Harvested energy is equal to the enclosed area in the polarization-electric field curve as the following equation [20]:

$$W_{\text{harvested}} = \oint E dP. \quad (2)$$

The energy taken from the high temperature reservoir is as the following:

$$Q_{\text{hot}} = c(T_2 - T_1) + \int_0^{E_M} p T_2 dE, \quad (3)$$

where  $T_2$  and  $T_1$  are the temperatures at high and low reservoir, respectively, and  $E_M$  is the maximum electric field amplitude. The efficiency is calculated as the following:

$$\eta = \frac{W_{\text{harvested}}}{Q_{\text{hot}}}. \quad (4)$$

The electrocaloric effect is very small in the majority of ferroelectric materials, in comparison with thermal capacity multiplied with temperature variations [21], leading to the assumption which is

$$c(T_2 - T_1) \gg \int_0^{E_M} p T_2 dE. \quad (5)$$

Therefore, the efficiency can be written as the following:

$$\eta = \frac{W_{\text{harvested}}}{c(T_2 - T_1)}. \quad (6)$$

## 3. Results

Ozgul and his colleagues [22] present a schematic of the polarization decay in a ferroelectric material as a function of the number of applied electric field cycles. Also, they show that the remnant polarization decreases steadily with increase of the number of cycles. This phenomenon is the polarization fatigue process in the ferroelectric materials. The polarization hysteresis exhibits very slight decreases in the remnant polarization and continuously shifts to lower

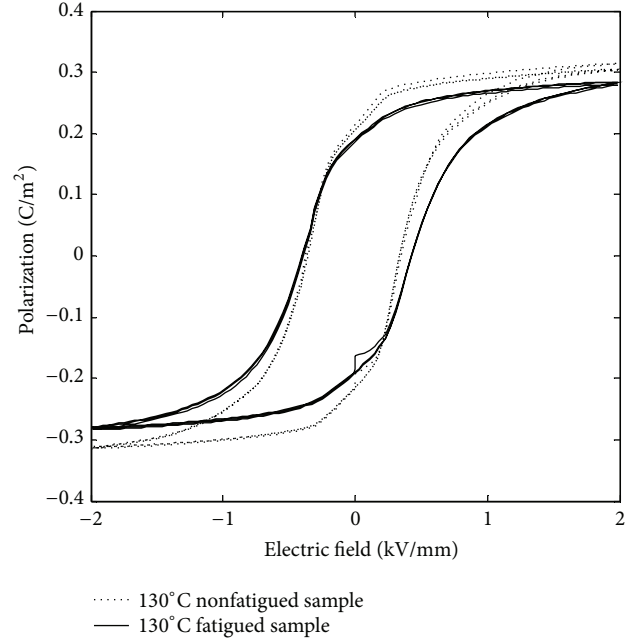


FIGURE 1: Comparison of dynamic hysteresis loops (polarization-electric field) before (pointed line) and after the fatigue occurrence (continuous line, 600th cycle).

polarization values. These shifts of hysteresis loops display an exponential dependence on the number of measurement cycles. Also, they show that the polarization fatigue is not very perceptible for applied small electric fields, but it began to decrease after about 100 cycles for high electric fields and the fatigue process occurred [22].

In the present work, the bipolar cyclic electric field is applied to the PZN-4.5PT single crystal with dimensions of  $8 \times 4 \times 1 \text{ mm}^3$  and  $8000 \text{ kg/m}^3$  density at  $130^\circ\text{C}$ . Two electrodes of the sample are electrically connected to the power supply and immersed in a bath of silicon oil in order to avoid arcing. This test was performed under application of bipolar triangular voltage waveform switching cycles with amplitude of  $2 \text{ kV/mm}$ . The cycling field was steadily increased from zero to the maximum field value within  $0.25 \text{ s}$ ; thereafter it was reduced to zero again within  $0.25 \text{ s}$ . Based on the Ozgul results [22], this field is high and fatigue should occur. Therefore, polarization starts to decrease quickly, approximately after 100 cycles. Figure 1 presents the polarization hysteresis loop versus the electric field for the considered sample, when the sample is not fatigued and then after 600 cycles when the fatigue occurred. The existence of fatigue is confirmed by the shift of polarization hysteresis loop to the lower polarization values as observed. The remnant polarization variations between two cases are about 10 percent.

A pyroelectric converter directly transforms heat energy into electrical energy. Along with the pyroelectric conversion a basic thermodynamic cycle (from the electrical energy producing point of view) will be helpful. The production of the electrical energy may be described in terms of the polarization-electric field behavior of a ferroelectric material.

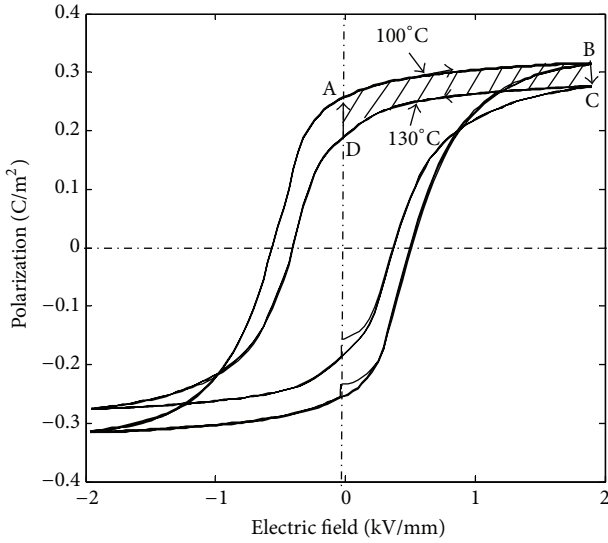


FIGURE 2: Polarization-electric field characteristics of PZT-4.5PT at two different temperatures of 100 and 130°C.

Figure 2 illustrates P-E (polarization versus applied electric field) behavior of a ferroelectric material which may be utilized for pyroelectric conversion. The area of each cyclic process on P-E diagram represents an electrical work (2). The direction of the path on the cycle (clockwise or counterclockwise) determines whether the electrical energy is produced or dissipated. Electrical energy production cycle may be realized by appropriate phase changes in temperature and applied electric field. Figure 2 is an overlay of the polarization-electric field characteristics of a ferroelectric (PZT-4.5PT) at two different temperatures. It also shows how the clockwise cycling may be achieved when operating is between two temperatures. Starting at point A at low electric field and low temperature (100°C) then at this temperature, the ferroelectric (FE) is recharged by increasing the externally applied electric field until point B. Then it is heated at constant electric field until a high temperature (130°C) (path BC). At this temperature, it is discharged by reducing applied electric field (path CD). Then it is cooled at low electric field (path DA). Therefore, the electrical cycle may be performed in a clockwise manner in which the produced electrical energy per cycle is equal to

$$W_{\text{harvested}} = \oint E dP = \text{Hatching area (ABCD)}. \quad (7)$$

The cycle is an electrical analogue of the Ericsson thermodynamic cycle.

In this paper, the aim is the effect of polarization fatigue on the harvested energy. Is the fatigue reducing the value of harvested energy? To respond to this question, the Ericsson thermodynamic cycle was modeled with measured polarization at 100 and 130°C for the cases in which fatigue occurred and did not occur. The experimental results have been presented in Figure 3. This cycle is an effective thermodynamic cycle and practically feasible [23–26]. It consists of two isothermal and two constant electric field processes. As

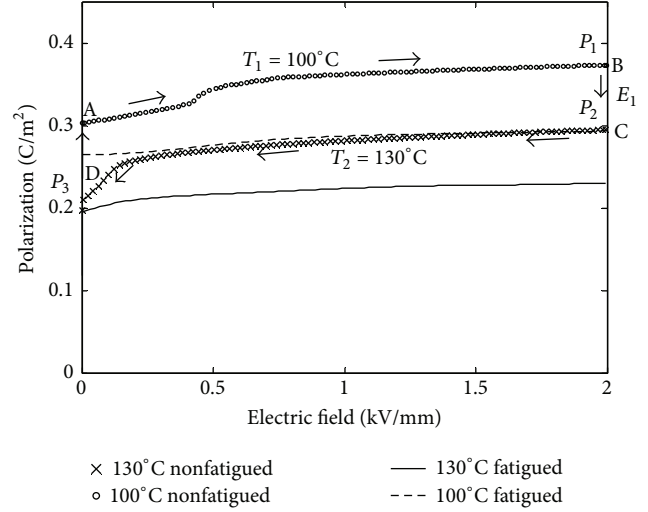


FIGURE 3: Normalized unipolar polarization Ericsson cycle for 2 samples of PZT-4.5PT, fatigued (after 600 cycles) and nonfatigued (after 30 cycles) between 100 and 130°C.

shown in Figure 3, Ericsson cycle starts at a temperature  $T_1$ , with the application of an increasing electric field until  $E_M$  ( $E_M = 2$  kV/mm) which increases the polarization to the value of  $P_1$  (path AB). Temperature is then increased to  $T_2$  under constant electric field  $E_M$  (path BC) and consequently polarization decreases to  $P_2$ . Then the applied electric field is decreased to 0 which causes a decrease of polarization to  $P_3$  (path CD). Finally, the temperature is decreased to its initial value at zero electric field (path DA). For more information about modeling of the Ericsson thermodynamic cycle please refer to [17].

The enclosed areas by Ericsson cycles (harvested energy) in two cases of fatigued and nonfatigued are approximately equal and their difference is less than 5%, although there is a remarkable difference in their curves of polarization-electric field (Figure 1). The harvested energies in the cases of nonfatigued and fatigued are equal to 20.53 mJ/g and 19.59 mJ/g, respectively. Furthermore, the phase change is not observed in the case of fatigued sample. These results indicate that dielectric behavior of ferroelectric materials is undergoing fatigue but their pyroelectric properties is not fatigued.

#### 4. Conclusions

The polarization fatigue was observed by polarization-electric field (P-E) hysteresis loop measurements. Fatigue in the ferroelectric capacitor corresponds to a decrease of the switchable polarization as a result of bipolar electric field cycling. Indeed, polarization in a ferroelectric material is a function of applied electric field cycle's number. Also, the effect of polarization fatigue on the value of harvested energy was studied under applied cyclic switching using modeled thermodynamic Ericsson cycle. According to the results, the polarization fatigue is not very perceptible for applied small electric fields. It is shown that the electrical energy

production can be described in terms of polarization-electric field behavior of a ferroelectric material. Although there is a remarkable difference between polarization-electric field curves in two cases of fatigued and nonfatigued samples, enclosed areas by Ericsson thermodynamic cycles (the value of harvested energy) in two cases are slightly different. Therefore, the polarization fatigue does not have a serious effect on the value of harvested energy.

### Conflict of Interests

The author declares that there is no conflict of interests regarding the publication of this paper.

### References

- [1] K. Uchino, *Piezoelectric Actuators and Ultrasonic Motors*, Kluwer Academic, Boston, Mass, USA, 1997.
- [2] D. L. Polla and L. F. Francis, "Ferroelectric thin films in microelectromechanical systems applications," *MRS Bulletin*, vol. 21, no. 7, pp. 59–65, 1996.
- [3] P. Muralt, A. Kholkin, M. Kohli, and T. Maeder, "Piezoelectric actuation of PZT thin-film diaphragms at static and resonant conditions," *Sensors and Actuators A*, vol. 53, no. 1–3, pp. 398–404, 1996.
- [4] Y. Yamashita, "Large electromechanical coupling factors in perovskite binary material system," *Japanese Journal of Applied Physics B*, vol. 33, no. 9, pp. 5328–5331, 1994.
- [5] J. F. Scott, C. A. Araujo, H. B. Meadows, L. D. McMillan, and A. Shawabkeh, "Radiation effects on ferroelectric thin-film memories: retention failure mechanisms," *Journal of Applied Physics*, vol. 66, no. 3, pp. 1444–1453, 1989.
- [6] J. F. Scott and C. A. Paz De Araujo, "Ferroelectric memories," *Science*, vol. 246, no. 4936, pp. 1400–1405, 1989.
- [7] W. L. Warren, B. A. Tuttle, and D. Dimos, "Ferroelectric fatigue in perovskite oxides," *Applied Physics Letters*, vol. 67, p. 1426, 1995.
- [8] A. K. Tagantsev, I. Stolichnov, E. L. Colla, and N. Setter, "Polarization fatigue in ferroelectric films: basic experimental findings, phenomenological scenarios, and microscopic features," *Journal of Applied Physics*, vol. 90, no. 3, pp. 1387–1402, 2001.
- [9] C. A. Paz de Araujo, J. D. Cuchlaro, L. D. McMillan, M. C. Scott, and J. F. Scott, "Fatigue-free ferroelectric capacitors with platinum electrodes," *Nature*, vol. 374, no. 6523, pp. 627–629, 1995.
- [10] W. L. Warren, D. Dimos, B. A. Tuttle, R. D. Nasby, and G. E. Pike, "Electronic domain pinning in Pb(Zr,Ti)O<sub>3</sub> thin films and its role in fatigue," *Applied Physics Letters*, vol. 65, no. 8, pp. 1018–1020, 1994.
- [11] W. C. Stewart and L. S. Cosentino, "Some optical and electrical switching characteristics of a lead zirconate titanate ferroelectric ceramic," *Ferroelectrics*, vol. 1, no. 1, pp. 149–167, 1970.
- [12] D. B. Fraser and J. R. Maldonado, "Improved aging and switching of lead zirconate-lead titanate ceramics with indium electrodes," *Journal of Applied Physics*, vol. 41, no. 5, pp. 2172–2176, 1970.
- [13] D. Wang, Y. Fotinich, and G. P. Carman, "Influence of temperature on the electromechanical and fatigue behavior of piezoelectric ceramics," *Journal of Applied Physics*, vol. 83, no. 10, pp. 5342–5350, 1998.
- [14] C. Verdier, D. C. Lupascu, and J. Rödel, "Unipolar fatigue of ferroelectric lead-zirconate-titanate," *Journal of the European Ceramic Society*, vol. 23, no. 9, pp. 1409–1415, 2003.
- [15] M. Ozgul, S. Trolier-Mckinstry, and C. A. Randall, "Fatigue induced effects on bipolar strain loops in PZN-PT piezoelectric single crystals," *Journal of Electroceramics*, vol. 20, no. 3–4, pp. 133–138, 2008.
- [16] W. H. Clingman and R. G. Moore Jr., "Application of ferroelectricity to energy conversion processes," *Journal of Applied Physics*, vol. 32, no. 4, pp. 675–681, 1961.
- [17] A. Khodayari, S. Pruvost, G. Sebald, D. Guyomar, and S. Mohammadi, "Nonlinear pyroelectric energy harvesting from relaxor single crystals," *IEEE Transactions on Ultrasonics, Ferroelectrics, and Frequency Control*, vol. 56, no. 4, pp. 693–698, 2009.
- [18] D. Guyomar, G. Sebald, E. Lefeuvre, and A. Khodayari, "Toward heat energy harvesting using pyroelectric material," *Journal of Intelligent Material Systems and Structures*, vol. 20, no. 3, pp. 265–271, 2009.
- [19] J. Grindlay, *An Introduction to the Phenomenological Theory of Ferroelectricity*, Pergamon Press, Oxford, UK, 1970.
- [20] D. Guyoniar, S. Pruvost, and G. Sebald, "Energy harvesting based on FE-FE transition in ferroelectric single crystals," *IEEE Transactions on Ultrasonics, Ferroelectrics, and Frequency Control*, vol. 55, no. 2, pp. 279–285, 2008.
- [21] G. Sebald, S. Pruvost, and D. Guyomar, "Energy harvesting based on Ericsson pyroelectric cycles in a relaxor ferroelectric ceramic," *Smart Materials and Structures*, vol. 17, no. 1, Article ID 015012, 2008.
- [22] M. Ozgul, K. Takemura, S. Trolier-McKinstry, and C. A. Randall, "Polarization fatigue in Pb(Zn<sub>1/3</sub>Nb<sub>2/3</sub>)O<sub>3</sub>-PbTiO<sub>3</sub> ferroelectric single crystals," *Journal of Applied Physics*, vol. 89, no. 9, pp. 5100–5106, 2001.
- [23] R. B. Olsen, D. A. Bruno, J. M. Briscoe, and E. W. Jacobs, "Pyroelectric conversion cycle of vinylidene fluoride-trifluoroethylene copolymer," *Journal of Applied Physics*, vol. 57, no. 11, pp. 5036–5042, 1985.
- [24] R. B. Olsen and D. Evans, "Pyroelectric energy conversion: hysteresis loss and temperature sensitivity of a ferroelectric material," *Journal of Applied Physics*, vol. 54, no. 10, pp. 5941–5944, 1983.
- [25] L. Kouchachvili and M. Ikura, "Pyroelectric conversion-Effects of P(VDF-TrFE) preconditioning on power conversion," *Journal of Electrostatics*, vol. 65, no. 3, pp. 182–188, 2007.
- [26] R. B. Olsen and D. D. Brown, "High efficiency direct conversion of heat to electrical energy related pyroelectric measurements," *Ferroelectrics*, vol. 40, no. 1, pp. 17–27, 1982.

## Research Article

# The Photocatalytic Reduction of Hexavalent Chromium by Controllable Mesoporous Anatase TiO<sub>2</sub> Nanoparticles

Vorrada Loryuenyong,<sup>1,2</sup> Natnapin Jarunsak,<sup>1</sup>  
Thirawich Chuangchai,<sup>1</sup> and Achanai Buasri<sup>1,2</sup>

<sup>1</sup> Department of Materials Science and Engineering, Faculty of Engineering and Industrial Technology,  
Silpakorn University, Nakhon Pathom 73000, Bangkok 10330, Thailand

<sup>2</sup> National Center of Excellence for Petroleum, Petrochemicals and Advanced Materials, Bangkok 10330, Thailand

Correspondence should be addressed to Vorrada Loryuenyong; [vorrada@gmail.com](mailto:vorrada@gmail.com)

Received 28 May 2013; Accepted 25 October 2013; Published 20 January 2014

Academic Editor: Ho Chang

Copyright © 2014 Vorrada Loryuenyong et al. This is an open access article distributed under the Creative Commons Attribution License, which permits unrestricted use, distribution, and reproduction in any medium, provided the original work is properly cited.

Titania (TiO<sub>2</sub>) nanoparticles with periodical mesopore size (up to 150 Å) have successfully been synthesized by sol-gel template method, using titanium(IV) tetraisopropoxide as a starting precursor and isopropanol as a solvent. Different quantities of activated carbon (0%, 5%, and 10% by weight) were used as templates to control the porosity and particle size of titania nanoparticles. The templates were completely removed during the calcination in air at 500 °C for 3 hr. The results showed that the specific surface area of titania is increased with increasing activated carbon content. The optical bandgap of synthesized titania exhibits a blue shift by 0.3–0.6 eV when compared to the reported value for the bulk anatase and rutile phases. The photocatalytic activity of porous titania is determined with its reduction efficiency of hexavalent chromium (Cr<sup>6+</sup>). The reduction efficiency is optimized under ultraviolet illumination.

## 1. Introduction

In general, chromium has two stable oxidation states, that is, Cr(VI) and Cr(III). The toxicity is mainly caused by hexavalent chromium, Cr(VI), which is virtually found in wastewater from industrial processes such as leather tanning, paint making, electroplating, and chromate production. This oxidation state has been classified as a carcinogen and mutagen not only to humans but also to other creatures. In many countries, as a consequence, the wastewater must be treated until the limit of Cr(VI) is below 0.05 mg/L before releasing to the water source [1]. One solution method is to convert it into Cr(III), which is considered as a nontoxic and essential trace metal in human nutrition. By chemical process, Cr(VI) is precipitated into Cr(III) as Cr(OH)<sub>3</sub> in neutral or alkaline solutions and removed as a solid waste [2, 3]. However, this process requires reducing agents such as ferrous sulfate, sodium hydrogen sulfite, sodium pyrosulfite, hydrazine hydrate, and sulfur dioxide, which are expensive

and dangerous with human skin and to release other unwanted chemicals [1].

Recently, there are many research works related to the use of semiconducting materials such as TiO<sub>2</sub> and ZnO as photocatalysts for various applications. This has many benefits including low cost, high efficiency, reusable performance, cleanliness, natural safety, and nontoxicity. The photocatalytic mechanism begins when a semiconducting material absorbs light with energy larger than its bandgap. As a consequence, electrons from the valence band would be excited to the conduction band, leaving holes behind. These electron-hole pairs could react with oxygen and water in air to produce free radicals such as hydroxyl radical, hydrogen peroxide, and superoxide anions. Such free radicals have an ability to destroy the structure of the bacteria, hold back the virus, and react with organic compound to become carbon dioxide and water. In addition, They can react with toxic gas and carcinogen such as acetaldehyde, benzene, and formaldehyde.

Due to an oxygen defect, titania ( $\text{TiO}_2$ ) exists naturally as an n-type semiconducting photocatalyst with an intrinsic bandgap of 3.0–3.2 eV. Among four major phases, anatase, rutile, brookite, and titania-B, anatase is generally the most photocatalytically active, owing to its wide bandgap, high specific surface area, and low recombination rates of electron-hole pairs [4–6]. On the other hand, rutile is a high-temperature stable phase and has high refractive index and weatherability. Nevertheless, many researchers have reported that the mixed phase of anatase and rutile has higher photocatalytic activity and better optical properties than pure anatase phase [7]. Despite phase, other important properties including well-controlled porosity and crystallinity are also desirable in photocatalytic applications [8].

In this research, activated carbon was used as a template for producing uniform mesoporous  $\text{TiO}_2$  with anatase phase by sol-gel method. The physical properties of synthesized  $\text{TiO}_2$  were studied. The reduction efficiency of Cr(VI) performance by synthesized  $\text{TiO}_2$  as a photocatalyst was determined. The effect of wavelength lighting source with photocatalytic performance was also discussed.

## 2. Materials and Methods

**2.1. Synthesis of  $\text{TiO}_2$  Nanoparticles.** The synthesis was carried out as reported in the literature [6, 7]. All reagents including titanium(IV) tetraisopropoxide (TIP) (Sigma-Aldrich, USA) as a Ti precursor, 37% HCl (Merck KGaA, Germany) as a sol-gel catalyst, isopropanol (Merck KGaA, Germany) as a solvent, and activated carbon (CGO-200, C. Gigantic Carbon) as a template were used without further purification.

5.5 mL TIP was dissolved in 71.8 mL isopropanol, and then, if applicable, 0.073 g (5% activated carbon by weight of synthesized  $\text{TiO}_2$ ) or 0.145 g activated carbon (10% by weight of synthesized  $\text{TiO}_2$ ) was added to the solution. The mixed solution of 19 mL water and 1.68 mL HCl was then added dropwise to titania-activated carbon suspensions under vigorous stirring at room temperature. The mixture was further stirred for 3 hr, and the obtained gel was centrifuged, washed to remove excess reactants and catalyst, and dried in the oven at 80°C for 24 hr. The dried samples were grinded and calcined at 500°C for 3 hr at the heating rate of 5°C/min. The samples would be labelled as 0% AC, 5% AC, and 10% AC for  $\text{TiO}_2$  synthesized with 0%, 5%, and 10% activated carbon, respectively.

**2.2. Characterization.** Thermogravimetric analysis (TGA) (TGA7, Perkin Elmer) was used to characterize the thermal stability of the samples by measuring the change in weight as a function of temperature. Fourier transform infrared spectroscopy (FTIR) (Vertex70, Bruker Optics) was used for studying the functional groups in the samples. X-ray diffraction (XRD) patterns were obtained on a Miniflex II, Rigaku diffractometer. Transmission electron microscope (TEM) (JEM-1230, JEOL) was employed to study the morphology of the synthesized samples. The specific surface area, the pore size distribution, and the average pore size of samples were evaluated by nitrogen adsorption and desorption as a function of relative pressure, using Brunauer-Emmett-Teller

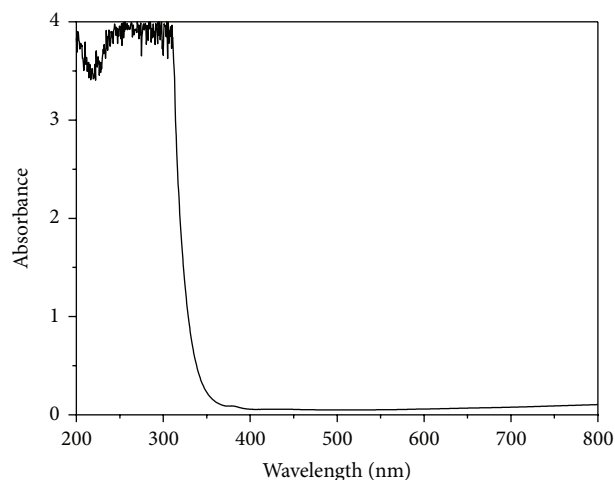


FIGURE 1: The absorbance spectrum of the filter.

(BET) and Barrett-Joyner-Halenda (BJH) methods. The % absorbance of samples was analyzed by UV-Vis spectrophotometer (UV-1800, Shimadzu).

**2.3. Reduction of Cr(VI).** In order to prepare 50 mg/L  $\text{K}_2\text{Cr}_2\text{O}_7$  aqueous solution, 50 mg  $\text{K}_2\text{Cr}_2\text{O}_7$  was added to a 1000 mL volumetric flask, and then the deionized water was poured until the solution level reached the 1000 mL mark on the neck of the flask. 0.02 g  $\text{TiO}_2$  (0%, 5%, or 10% AC) was then added to 20 mL  $\text{K}_2\text{Cr}_2\text{O}_7$  solution in separated 50 mL beakers. The suspensions were maintained at pH = 5 and vigorously stirred for 5 minutes before being illuminated by a light source. The illumination was performed at 150 watts and at a distance of 11 cm, measured from the tip of the lamp, using Newport's Oriel Solar simulator with actual spectral irradiance reported elsewhere (150 W low cost solar simulator, Newport Corporation). The absorbance of illuminated suspension was measured every 10 minutes for a total of 120 minutes. The effects of UV light illumination were conducted by the use of filter with light absorbance spectrum shown in Figure 1.

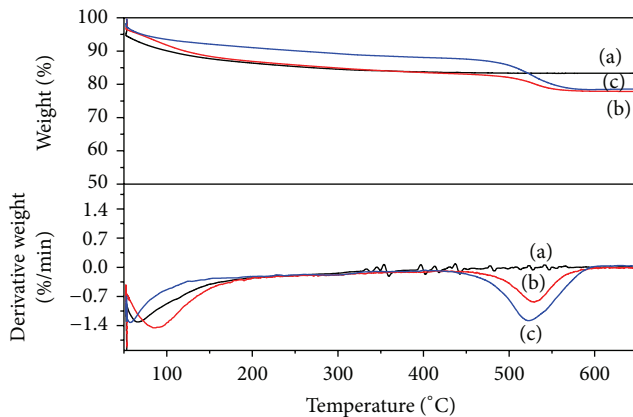
## 3. Results and Discussions

Figure 2 shows TGA and DTA graphs of synthesized  $\text{TiO}_2$  nanoparticles before calcination. The graph illustrates a weight loss at 100°C due to the release of the humidity and organic compounds. The samples synthesized with 5% and 10% activated carbon template, however, show two clearly defined steps of weight loss. Additional weight loss at the second step occurs at 500°C due to the decomposition of activated carbon. After calcination, as shown in Figure 3, it is found that the weight loss at 500°C disappears, confirming that activated carbon template is completely decomposed.

Figure 4 shows FTIR spectra of synthesized  $\text{TiO}_2$  nanoparticles before calcination. It is observed that all of the graphs have 3 main peaks: (1) O–H stretching at 3400  $\text{cm}^{-1}$ , (2) O–H bending at 1635  $\text{cm}^{-1}$ , and (3) Ti–O stretching at

TABLE I: Physical properties of P25 Aeroxide TiO<sub>2</sub> and synthesized TiO<sub>2</sub> nanoparticles.

Samples	Specific surface area (m <sup>2</sup> /g)	Pore diameter (nm)	Pore volume (cm <sup>3</sup> /g)	XRD particle size (Å)
0% AC	69.28	11.25	0.19	132
5% AC	94.34	7.92	0.19	105
10% AC	82.46	10.21	0.21	111
P25	61.00	67.3	1.03	180

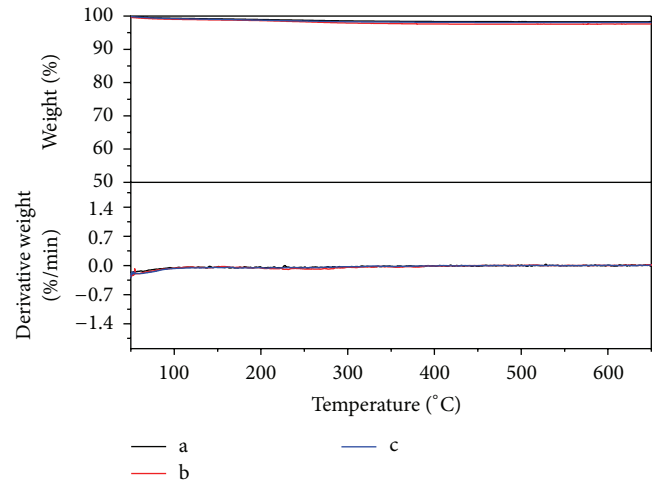
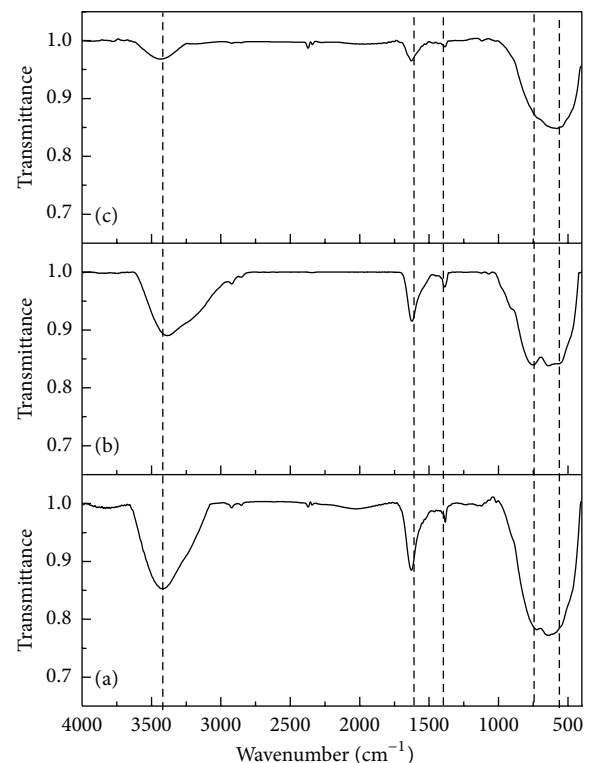
FIGURE 2: TGA-DTA of synthesized TiO<sub>2</sub> nanoparticles using an activated carbon template in different quantities and with no calcination: (a) 0%, (b) 5%, and (c) 10%.

700–400 cm<sup>-1</sup>. After calcination, however, the intensity of peaks at 3400 cm<sup>-1</sup> and 1635 cm<sup>-1</sup> is decreased due to the condensation of Ti–OH followed by the formation of a TiO<sub>2</sub> network structure (Figure 5). In addition, the intensity of the peak at 700–400 cm<sup>-1</sup> is evidently increased due to the stretching vibration of Ti–O–Ti in anatase phase.

Figure 6 shows the X-ray diffraction (XRD) patterns of TiO<sub>2</sub> nanoparticles. All the XRD peaks could be indexed as (101), (004), (200), (105), (211), (118), and (315) at 2-theta = 25, 38, 48, 53, 55, 63, and 75°, respectively, which corresponds to an anatase phase. The particle size of TiO<sub>2</sub> was calculated with the Scherrer formula using the XRD peak of anatase (101) plane as shown in Table I. Smaller particle size is observed with the use of activated carbon template. In comparison to P25 Aeroxide TiO<sub>2</sub> which contains anatase and rutile phases, the results show that pure anatase TiO<sub>2</sub> could be made via the hydration of titanium(IV) isopropoxide using a sol-gel technique and activated carbon template.

The morphologies of calcined TiO<sub>2</sub> are shown in Figure 7. It is found that TiO<sub>2</sub> nanoparticles are spherical in shape and do not agglomerate together. The particle size is similar to that predicted from XRD analysis. It could be predicted that the activated carbon as a template restrained the growth of TiO<sub>2</sub> particles, consistent with that reported previously [7].

Figures 8 and 9 show the N<sub>2</sub> adsorption/desorption isotherms and the corresponding BJH pore size distribution of titania nanoparticles, respectively. From the figure, it is observed that the isotherm of the synthesized TiO<sub>2</sub> can be ascribed to type IV. A summary of BET results is illustrated

FIGURE 3: TGA-DTA of synthesized TiO<sub>2</sub> nanoparticles using an activated carbon template in different quantities and with calcination at 500°C for 3 hr: (a) 0%, (b) 5%, and (c) 10%.FIGURE 4: FTIR graphs of synthesized TiO<sub>2</sub> nanoparticles using an activated carbon template in different quantities and with no calcination: (a) 0%, (b) 5%, and (c) 10%.

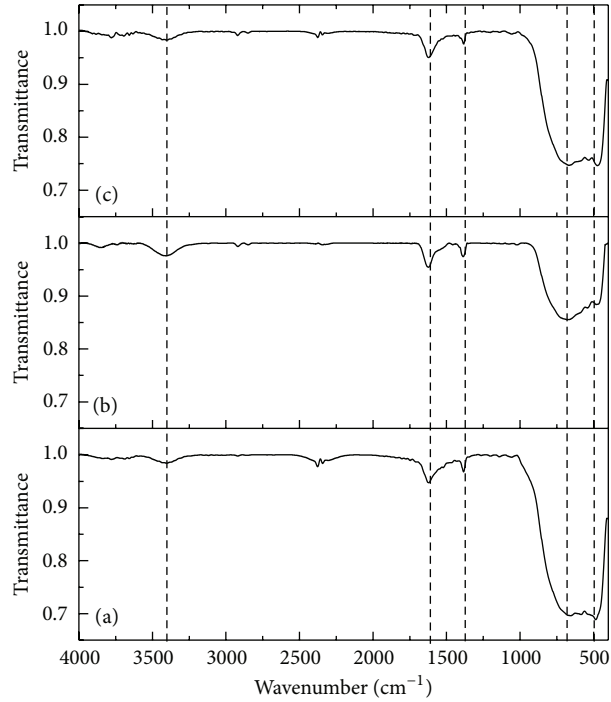


FIGURE 5: FTIR graphs of synthesized  $\text{TiO}_2$  nanoparticles using an activated carbon template in different quantities and with calcination at  $500^\circ\text{C}$  for 3 hr: (a) 0%, (b) 5%, and (c) 10%.

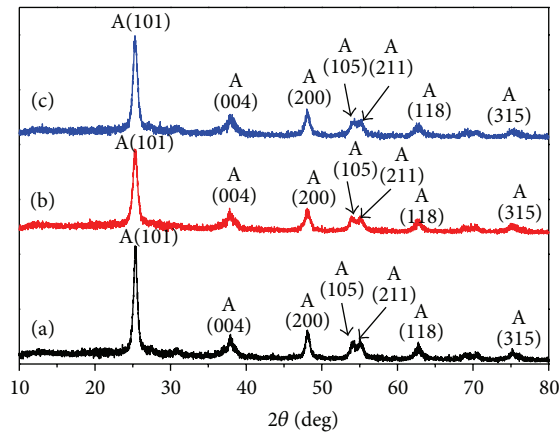


FIGURE 6: XRD pattern of synthesized  $\text{TiO}_2$  nanoparticles: (a) 0% AC, (b) 5% AC, and (c) 10% AC (A: anatase).

in Table 1, in comparison with those of commercial P25 Aeroxide  $\text{TiO}_2$  nanoparticles. As shown, activated carbon templates are likely to increase the specific surface area. All of the samples exhibit monodispersed mesopore size distribution up to  $150 \text{ \AA}$ . The specific surface area as high as  $94 \text{ m}^2/\text{g}$  could be obtained with the addition of 5% AC template and by a simple and inexpensive sol-gel method.

The optical bandgap of  $\text{TiO}_2$  nanoparticles has been determined from the absorption spectrum (Figure 10) using the following Tauc relation for a direct bandgap:  $\alpha h\nu = A(h\nu - E_g)^{1/2}$ , where  $\alpha$ ,  $t$ ,  $\nu$ ,  $A$ ,  $E_g$ , and  $n$  are the absorption coefficient, the thickness of the sample, frequency of the light, a constant, and the bandgap energy, respectively.

The average bandgap was then estimated from the intercept of linear portion of  $(\alpha h\nu)^2$  versus  $h\nu$ , as shown in Figure 7 [9]. From the figure, the bandgap energy of  $\text{TiO}_2$  prepared using activated carbon in the amount of 0%, 5%, and 10% by weight was 3.58, 3.48, and 3.59 eV, respectively. Generally, the particle size of the  $\text{TiO}_2$  has the bandgap energy between 3.0 and 3.2 eV. The observed large bandgap could be due to the effect of restricted movement of electrons, called “electron confinement.”

In this experiment, the efficiency of catalytic  $\text{TiO}_2$  was tested by using the reduction of potassium dichromate ( $\text{K}_2\text{Cr}_2\text{O}_7$ ) as the model compound (Figure 11). The absorbance peaks of  $\text{K}_2\text{Cr}_2\text{O}_7$  are found at 273 nm and

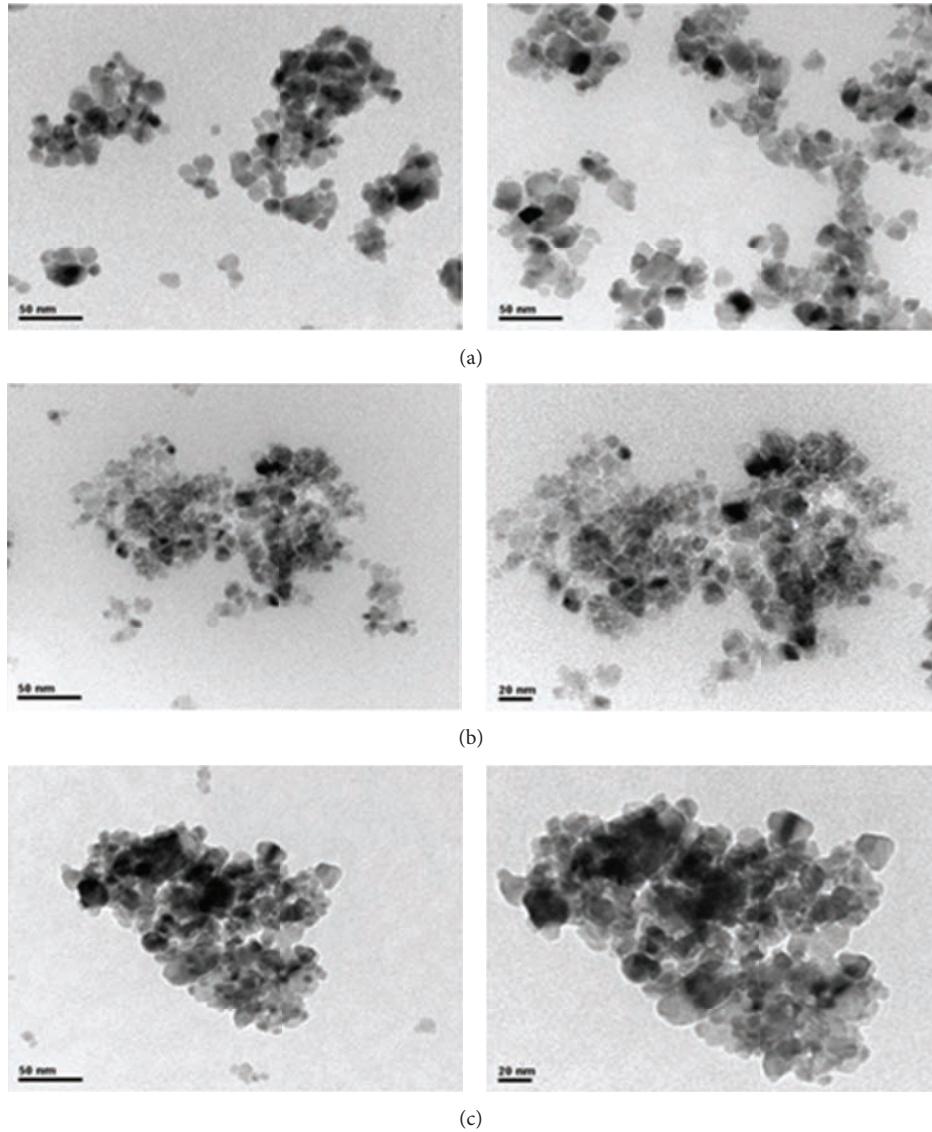


FIGURE 7: TEM images of synthesized TiO<sub>2</sub> nanoparticles: (a) 0% AC, (b) 5% AC, and (c) 10% AC.

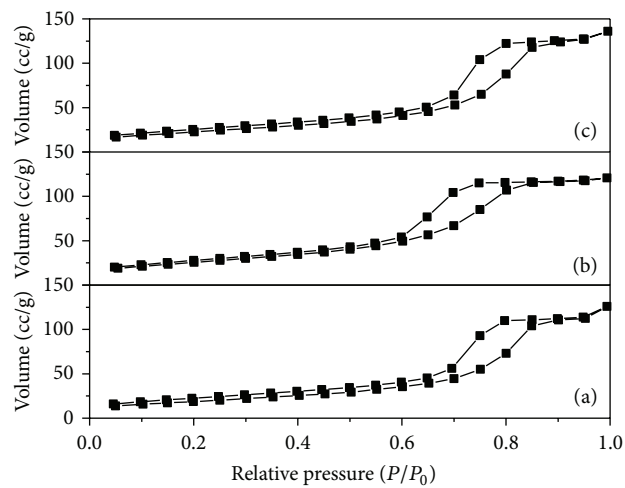


FIGURE 8: N<sub>2</sub> adsorption/desorption isotherms of synthesized TiO<sub>2</sub> nanoparticles: (a) 0% AC, (b) 5% AC, and (c) 10% AC.

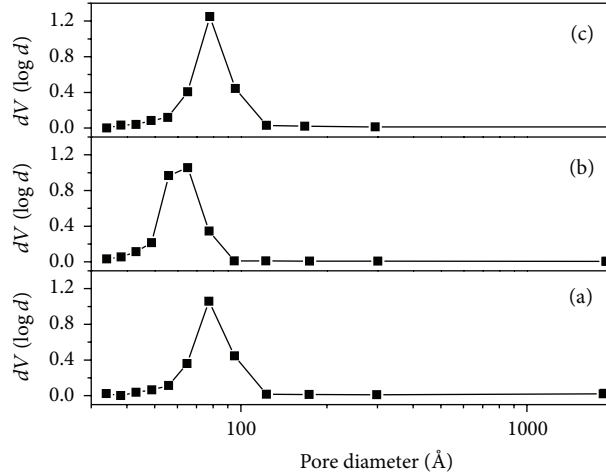


FIGURE 9: The BJH pore size distribution graphs of synthesized TiO<sub>2</sub> nanoparticles: (a) 0% AC, (b) 5% AC, and (c) 10% AC.

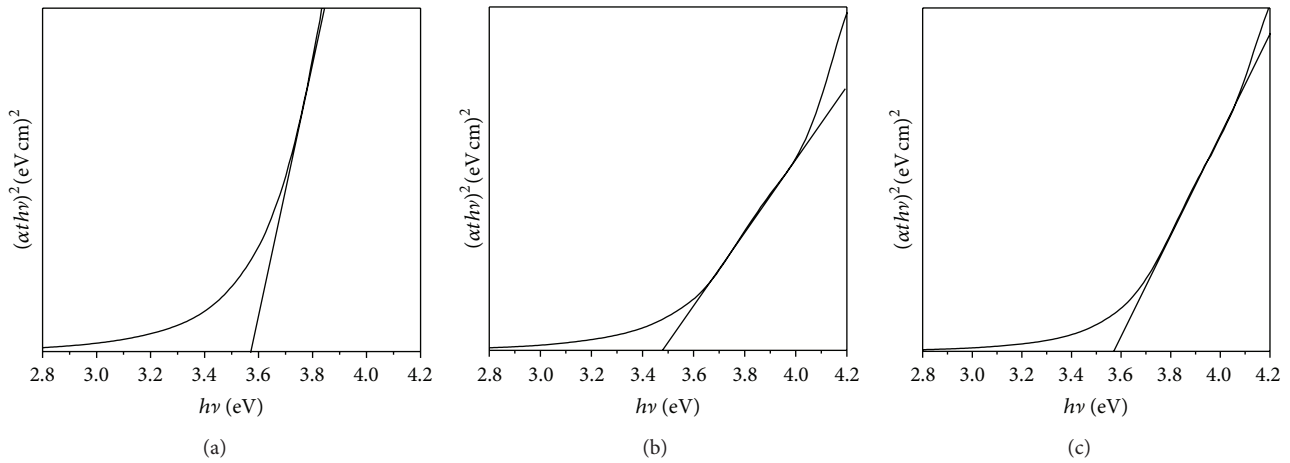
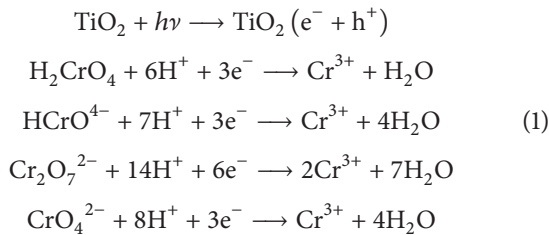


FIGURE 10: The relationship between  $(\alpha h\nu)^2$  and  $h\nu$  of synthesized TiO<sub>2</sub> nanoparticles: (a) 0% AC, (b) 5% AC, and (c) 10% AC.

350 nm. Without a photocatalyst, K<sub>2</sub>Cr<sub>2</sub>O<sub>7</sub> is not degradable under the light irradiation using solar simulator (not shown here). With TiO<sub>2</sub> as a photocatalyst, however, TiO<sub>2</sub> can absorb photons with energy higher than its bandgap, causing electrons to jump across the bandgap into conduction band. These free electrons involved in the reactions with the K<sub>2</sub>Cr<sub>2</sub>O<sub>7</sub> solution and Cr<sup>6+</sup> could be reduced to Cr<sup>3+</sup> in the form of Cr(OH)<sub>3</sub>, following the equations below [10, 11]:



As a result, the absorbance intensity decreased over exposure time.

In addition, it is found that the maximum peaks were red-shifted toward longer wavelength. This could be due to

the transformation from dichromate K<sub>2</sub>Cr<sub>2</sub>O<sub>7</sub> into chromate K<sub>2</sub>CrO<sub>4</sub> caused by hydroxyl groups on the surface of TiO<sub>2</sub> nanoparticles, following the equation



With optical filter, a decrease in absorbance intensity of K<sub>2</sub>Cr<sub>2</sub>O<sub>7</sub> aqueous solution is less than that without filter. This indicates that the reduction is less likely to take place due to less energy from the light to sufficiently excite electrons across the bandgap. Comparison of reduction capacities of synthesized TiO<sub>2</sub> (10% AC) with P25 Aeroxide TiO<sub>2</sub>, as shown in Figure 12, shows a higher photocatalytic activity. This suggests that the photocatalytic activity could be improved by changes in crystalline phase as well as specific surface area of photocatalytic materials.

#### 4. Conclusions

TiO<sub>2</sub> with controllable mesoporous anatase phase could be synthesized using sol-gel method and activated carbon

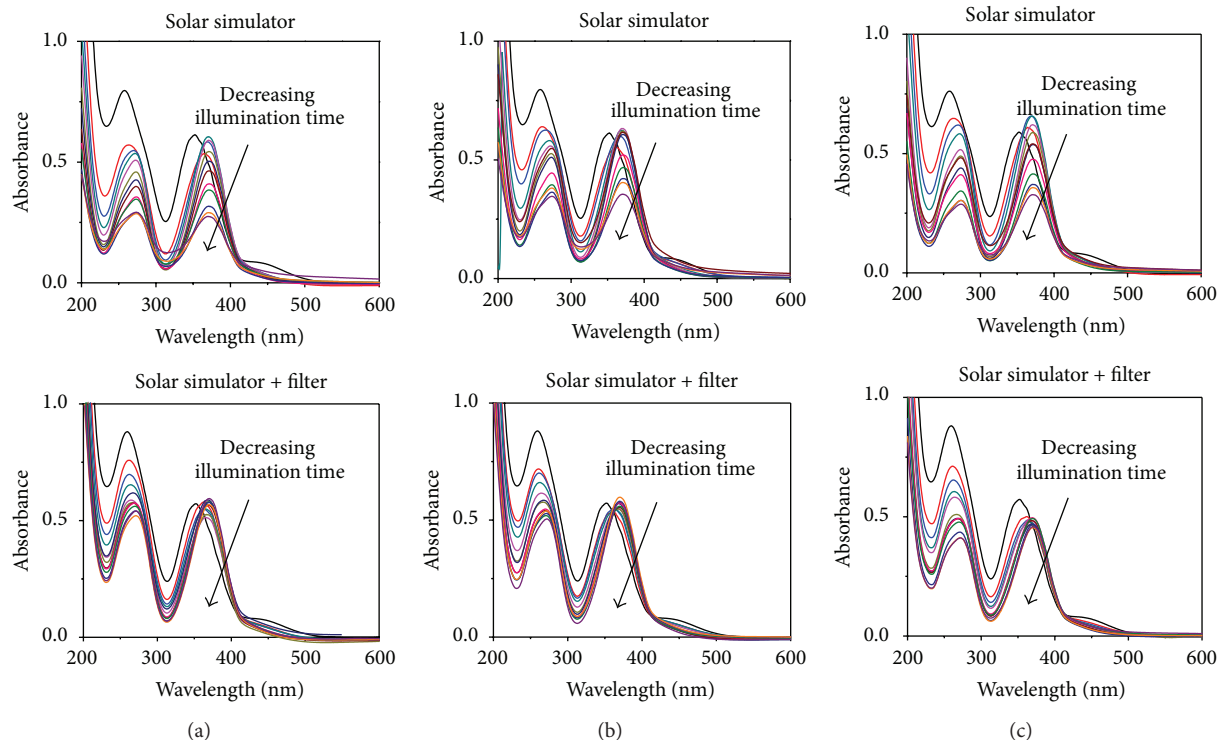


FIGURE 11: The absorbance spectrum of  $K_2Cr_2O_7$  aqueous solution with various  $TiO_2$  as photocatalysts as a function of illumination time: (a) 0% AC, (b) 5% AC, and (c) 10% AC. The solar simulator with xenon 150 W lamp with and without a filter was used as a light source.

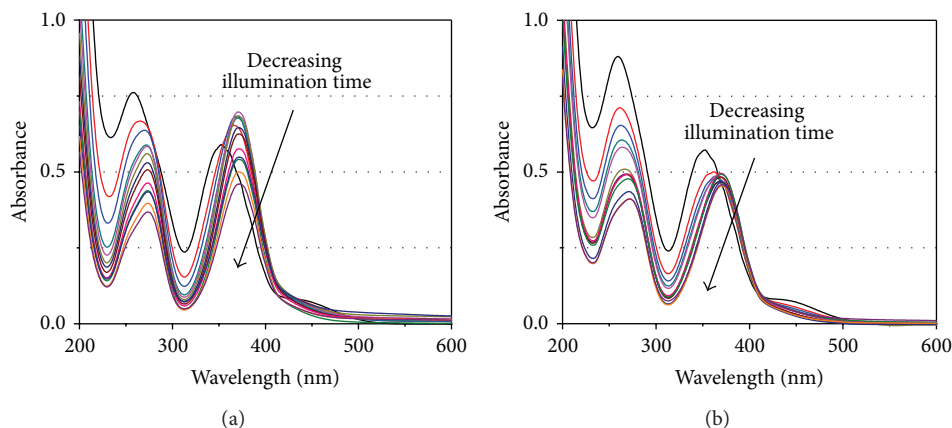


FIGURE 12: The absorbance spectrum of  $K_2Cr_2O_7$  aqueous solution with (a) P25 Aeroxide  $TiO_2$  and (b)  $TiO_2$  synthesized with 10% AC as photocatalysts as a function of illumination time. The solar simulator with xenon 150 W lamp with a filter was used as a light source.

template. The bandgap energy of synthesized  $TiO_2$  is 3.48–3.59 eV due to the effect of electron confinement. The performance of  $TiO_2$  as a photocatalyst gave a good result when using lighting source system in the UV region. Over irradiation time, the concentration was decreased, indicating an increase in reduction of  $Cr^{6+}$ . Furthermore, there was evidence that the two main absorption peaks were red-shifted to the right due to the transformation of dichromate  $Cr_2O_7^{2-}$  into chromate  $CrO_4^{2-}$  form by hydroxyl group on  $TiO_2$  surface.

## Conflict of Interests

The authors declare that there is no conflict of interests.

## Acknowledgments

The authors wish to thank the Department of Materials Science and Engineering, Faculty of Engineering and Industrial Technology, Silpakorn University, and the National Center of Excellence for Petroleum, Petrochemicals and Advanced

Materials for supporting and encouraging this investigation. This work was supported by the Higher Education Research Promotion (HERP), the Office of the Higher Education Commission.

## References

- [1] Y. C. Zhang, J. Li, M. Zhang, and D. D. Dionysiou, "Size-tunable hydrothermal synthesis of SnS<sub>2</sub> nanocrystals with high performance in visible light-driven photocatalytic reduction of aqueous Cr(VI)," *Environmental Science and Technology*, vol. 45, no. 21, pp. 9324–9331, 2011.
- [2] L. E. Eary and R. Dhanpat, "Chromate removal from aqueous wastes by reduction with ferrous ion," *Environmental Science and Technology*, vol. 22, no. 8, pp. 972–977, 1988.
- [3] T. K. Yurik and A. K. Pikaev, "Radiolysis of weakly acidic and neutral aqueous solutions of hexavalent chromium ions," *High Energy Chemistry*, vol. 33, no. 4, pp. 208–212, 1999.
- [4] M. Pal, J. G. Serrano, P. Santiago, and U. Pal, "Size-controlled synthesis of spherical TiO<sub>2</sub> nanoparticles: morphology, crystallization, and phase transition," *Journal of Physical Chemistry C*, vol. 111, no. 1, pp. 96–102, 2007.
- [5] G. Wang, "Hydrothermal synthesis and photocatalytic activity of nanocrystalline TiO<sub>2</sub> powders in ethanol-water mixed solutions," *Journal of Molecular Catalysis A*, vol. 274, no. 1-2, pp. 185–191, 2007.
- [6] V. Loryuenyong, K. Angamnuaysiri, J. Sukcharoenpong, and A. Suwannasri, "Sol-gel template synthesis and photocatalytic behavior of anatase titania nanoparticles," *ScienceAsia*, vol. 38, pp. 301–306, 2012.
- [7] V. Loryuenyong, A. Buasri, C. Srilachai, and H. Srimuang, "The synthesis of microporous and mesoporous titania with high specific surface area using sol-gel method and activated carbon templates," *Materials Letters*, vol. 87, pp. 47–50, 2012.
- [8] J. B. Joo, I. Lee, M. Dahl, G. F. Moon, F. Zaera, and Y. Yin, "Controllable synthesis of mesoporous TiO<sub>2</sub> hollow shells: toward an efficient photocatalyst," *Advanced Functional Materials*, vol. 23, no. 34, pp. 4246–4254, 2013.
- [9] B. M. Weckhuysen and R. A. Schoonheydt, "Recent progress in diffuse reflectance spectroscopy of supported metal oxide catalysts," *Catalysis Today*, vol. 49, no. 4, pp. 441–451, 1999.
- [10] S. Tuprakay and W. Liengcharernsit, "Lifetime and regeneration of immobilized titania for photocatalytic removal of aqueous hexavalent chromium," *Journal of Hazardous Materials*, vol. 124, no. 1–3, pp. 53–58, 2005.
- [11] C. E. Barrera-Díaz, V. Lugo-Lugo, and B. Bilyeu, "A review of chemical, electrochemical and biological methods for aqueous Cr(VI) reduction," *Journal of Hazardous Materials*, vol. 223–224, pp. 1–12, 2012.

## Research Article

# Performance Analysis of Al<sub>2</sub>O<sub>3</sub>/Water Nanofluid with Cationic Chitosan Dispersant

T. Y. Chen,<sup>1</sup> H. P. Cho,<sup>2</sup> C. S. Jwo,<sup>1</sup> and L. Y. Jeng<sup>3</sup>

<sup>1</sup> Department of Energy and Air-Conditioning Refrigeration Engineering, National Taipei University of Technology, Taipei City 10608, Taiwan

<sup>2</sup> Department of Mechanical Engineering, National Taiwan University, Taipei City 10617, Taiwan

<sup>3</sup> Graduate Institute of Mechanical and Electrical Engineering, National Taipei University of Technology, Taipei City 10608, Taiwan

Correspondence should be addressed to T. Y. Chen; [t100459002@ntut.edu.tw](mailto:t100459002@ntut.edu.tw)

Received 15 September 2013; Accepted 23 October 2013

Academic Editor: Ho Chang

Copyright © 2013 T. Y. Chen et al. This is an open access article distributed under the Creative Commons Attribution License, which permits unrestricted use, distribution, and reproduction in any medium, provided the original work is properly cited.

This study aimed to investigate the effect of the cationic chitosan dispersant on the thermal conductivity, dispersion, and the suspension of 15 nm Al<sub>2</sub>O<sub>3</sub>/water nanofluid. The study employed two-step method to mix the Al<sub>2</sub>O<sub>3</sub> powder, deionized water, and dispersant to conduct an experiment of the settling properties and thermal conductivity of nanofluid in a stable environment, analyzing the adhesion of nanofluid to copper pipe walls in practical operations. The results indicated that 1.0 wt.% Al<sub>2</sub>O<sub>3</sub>/water nanofluid with 0.05 wt.% cationic chitosan dispersant increased its thermal conductivity up to 4.1% and 12.6% compared with nanofluid with deionized water at the temperature of 15°C and 55°C. At the flow ratio of 2 L/min, the overall heat conductivity improved by 8.3% and 17.4%, respectively, under 60 W and 150 W heating power. The solution performed better in dispersion and suspension than that in the original sample with no cationic chitosan dispersant. The cationic chitosan dispersant, as a result, was proved to improve the dispersion and suspension of nanofluid. It also helped to reduce the frequency of nanoparticles sticking to the pipe wall, increasing the practicability of nanofluid.

## 1. Introduction

The application of nanofluid, such as application in heat pipe, heat exchanger, practical utilization of solar energy, and water cooling system, is gradually expanding [1–5]. Previous studies had already suggested adding nanoparticles to the substrate solution to increase its thermal conductivity [6–18]. However, thermal conductivity of nanofluid may not be influenced other than the particle size, agglomeration, and precipitation [12, 14, 15, 19–21]. On the other hand, the millimeter-sized and micron-sized particles added to the working fluid may lead to pipe blockage and abrasion [22]. To improve the suspension and settling properties of nanofluid and to prevent blockage possibilities of pipelines resulting from nanofluid have become important issues [23].

In 2009, Zhu et al. [24] studied the effect of the suspension behavior of Al<sub>2</sub>O<sub>3</sub>/water nanofluid on different pH values and different concentrations of sodium dodecylbenzene sulfonate (SDBS) dispersant on thermal conductivity.

The result indicated that the stability and thermal conductivity of Al<sub>2</sub>O<sub>3</sub>/water nanofluid had a significant correlation with different pH values and different concentrations of SDBS dispersant. The thermal conductivity increased by 10.1% when the weight concentration of Al<sub>2</sub>O<sub>3</sub> nanoparticle reached 0.0015.

Wusiman et al. [25] applied the SDBS and sodium dodecyl sulfate (SDS) dispersant to the carbon nanotube solution in 2012. These two surface-active agents enabled better dispersion and long-time stability of the fluid.

In 2012, Hung et al. [1] proposed the Al<sub>2</sub>O<sub>3</sub>/water nanofluid and applied the nanofluid with cationic chitosan dispersant to heat pipe operation. Such an application increased the working efficiency by 22.7%–56.3% more than the substrate solution. Dispersant helped to increase the suspension and stability of fluids; however, it also reduced the heat conductivity ratio of the fluid [1, 25].

This study employed a series of experiments in precipitation, adhesion on the metal surface, and thermal conductivity

of the fluids to discuss the influence of dispersant on the nanofluid and its practicability.

## 2. Interrelated Theories

**2.1. Agglomeration.** Agglomeration refers to a phenomenon in which single particles agglomerate with each other to reduce the surface energy in each particle. The smaller the particle is, the higher the surface energy is. Agglomeration can be divided into hard agglomeration and soft agglomeration in terms of different cohesion of particles. The chemical bonds among particles in hard agglomeration make them uneasy to disperse. There are, however, no chemical bonds among particles in soft agglomeration, resulting in looser structure than those among particles in hard agglomeration. Particles in soft agglomeration, consequently, may easily disperse into single particles [26, 27].

**2.2. Dispersion Technology.** There are three methods in fluid dispersion technology as follows: mechanical control, medium control, and agent control. Mechanical control applies disintegrator, ultrasonic oscillator, and electromagnetic stirring to particle dispersion. Medium control applies different mediums to different particles in terms of surface properties and like polarity to reach better dispersion effects. Agent control applies different dispersants to different particles in terms of the physical and chemical conditions of the medium to improve the rejection among particles [26, 27].

**2.3. Zeta Potential.** Zeta potential is an important parameter of particle suspension behavior. Due to surface energy, the well-dispersed suspended particles may agglomerate with each other, leading to precipitation. The repulsive energy of suspended nanoparticles in a solution is small, generally speaking. Agglomeration may occur when the attracting energy among particles is larger than the repulsive energy. The repulsive energy, therefore, should be improved to prevent agglomeration. As a result, a relatively high zeta potential will confer stability of nanofluid [26, 28].

**2.4. Settling Rate.** The experiment was designed to investigate the correlating process of changes between density and time on the fluid added with the 15 nm  $\text{Al}_2\text{O}_3$  nanoparticles and dispersant. The density changes, based on the same fluid sample, were measured initial and final in experimental. Therefore, the ratio of the pre- and postmeasurement as well as the initial density measurement was utilized to represent the settling rate of the fluid. It is shown in

$$r_s = \frac{\rho_{\text{final}} - \rho_{\text{initial}}}{\rho_{\text{initial}}}, \quad (1)$$

where  $\rho_{\text{initial}}$  is the initial measurement density and  $\rho_{\text{final}}$  is the final measurement density.

**2.5. The Overall Heat Transfer Capacity Ratio.** This study employed water and 15 nm  $\text{Al}_2\text{O}_3$  nanoparticles as the substrate solution to compare the overall heat transfer capacity

ratio of solution with dispersant and solution without dispersant. The experiment was designed to calculate the differences in thermal conductivities of nanofluid and water with the same control variables and heat exchanger. The overall heat transfer capacity ratio ( $r_{\text{OHTC}}$ ) in the heat exchanger can be implied by the following:

$$r_{\text{OHTC}} = \frac{U_{\text{nanofluid}}}{U_{\text{water}}} = \frac{(T_{\text{wall}} - T_m)_{\text{water}}}{(T_{\text{wall}} - T_m)_{\text{nanofluid}}}, \quad (2)$$

where  $T_{\text{wall}}$  is the mean temperature of the base plate and  $T_m$  is the average temperature of liquid traversing the heat exchange,  $T_m = (T_{\text{liq.in}} + T_{\text{liq.out}})/2$ .

## 3. Experimental

**3.1. Experimental Apparatus and Procedure.** The study employed the 15 nm  $\text{Al}_2\text{O}_3$ /water nanofluid with cationic chitosan dispersant to analyze the properties of nanofluid, among which the powder concentrations of the solution were 0.5 wt.% and 1.0 wt.%, and the dispersant concentrations were 0.0 wt.%, 0.05 wt.%, 0.1 wt.%, 0.3 wt.%, and 0.5 wt.%. All the samples were concocted in light of the two-level allegation. The pending experimental samples were made by operating through ultrasonic cleaner (TOHAMA, DC400, Taiwan) and electromagnetic stirrer (PC-420D, CORNING, Taiwan) 3 times each and the interval of each operation was 1 hour. Basic procedures of the experiment were listed as follows. (1) Zeta potentials of the fluid samples at the same temperature were measured by Zetasizer (Nano ZS90, MALVERN, United Kingdom). All the measured samples were selected at the fixed distance under the same fluid level and then tested in the measuring containers. (2) The fluid samples were selected from 15 cm below the fluid level every 24 hours and the density changes were measured by densitometer (DA-130N, KEM, Japan) in the consecutive 20 days. The experimental samples were placed in the environmental temperature of 25°C during the testing period. (3) The heat conductivity ratio of the fluid samples at the same temperature and fluid level was measured by thermal property analyzer (KD2, DECAGON, United States). The temperature was controlled by setting a desired temperature onto the thermostatic sink (B403L, FIRSTEK, Taiwan) and the experimental samples were then placed in it to wait until the temperature became stabilized before reaching the desired temperature. The thermostatic sink was temporarily shut down to reduce the impact of vibration on the properties during the experimental period. (4) Components of the copper pipe wall that had direct contact with nanofluid were analyzed by energy dispersive spectrometer (7852, OXFORD Instruments, UK). The copper patch was placed in the inner layer of the beaker in which the fluid sample was filled and then taken out to be examined and measured after 40-hour operation by electromagnetic heating stirrer (PC-420D, CORNING, Taiwan) under the condition of 35°C and 200 rev/min. The study aimed to investigate the disparity, suspension, thermal conductivity capacity, and applications of the nanofluid by means of the basic experimental procedures.

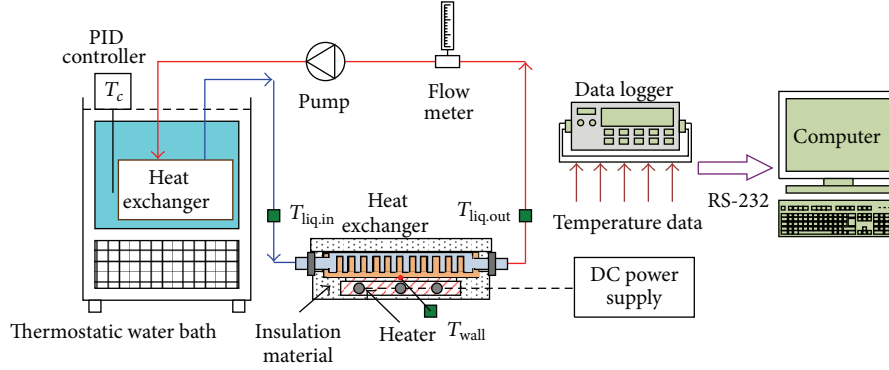


FIGURE 1: Layout of device in heat exchange experiment.

TABLE 1: Parameters in heat exchange experiment.

Items	Parameters
Volume of the fluid sample	750 mL
Inlet water temperature of heat exchanger	20°C, 40°C
Sample of fluid	Solution without dispersant: 0.5 wt.% and 1.0 wt.% Al <sub>2</sub> O <sub>3</sub> /water Solution with 0.05 wt.% cationic chitosan dispersant: 0.5 wt.% and 1.0 wt. % Al <sub>2</sub> O <sub>3</sub> /water
Heating power	60 W, 90 W, 120 W, and 150 W
Flow ratio	1 L/min and 2 L/min
Temperature	25 ± 2°C

Experiment on the overall heat transfer capacity ratio was employed by water circulating system, as shown in Figure 1, to analyze the thermal exchange capacity of the nanofluid with dispersant. Thermostatic sink was in place to supply stable inlet water temperature of heat exchanger, DC water pump (MCP-655, SWIFTECH, USA) was equipped with the flow meter to enable a constant flow ratio, and heater combined with power supply (GPC-3030DQ, GW INSTEK, Taiwan) was applied to provide stable heating power. The data was obtained and analyzed through data logger. Parameters of the experiment are shown in Table 1.

**3.2. Uncertainty Analysis.** The uncertainty of the experimental result was determined by the bias of experimental measurement parameters. The density was measured by the densitometer and the steel ruler was used to measure the distance from that below fluid level in the precipitation experiment. The thermal property analyzer was applied to measure thermal conductivity coefficient and T-type thermocouple was to measure fluid temperature in the thermal conductivity coefficient experiment. In the overall thermal exchange experiment, the flow was measured by flow meter and T-type thermocouple was used to measure inlet and outlet water temperatures of the fluid heat exchanger and mean temperature of the base plate. Power supply was there to provide stable heating power. The uncertainty of settling

rate, heat conductivity rate, and overall heat transfer capacity ratio was displayed as follows:

$$u_{r_s} = \left( \frac{\Delta\rho_{\text{initial}}}{\rho_{\text{initial}}} + \frac{\Delta\rho_{\text{final}}}{\rho_{\text{final}}} + \frac{\Delta L}{L} + \frac{\Delta T_{\text{ambient}}}{T_{\text{ambient}}} \right)^{1/2}, \quad (3)$$

$$u_{k_{\text{nf}}/k_{\text{bf}}} = \left( \frac{\Delta k_{\text{nf}}}{k_{\text{nf}}} + \frac{\Delta k_{\text{bf}}}{k_{\text{bf}}} + \frac{\Delta T_{\text{liq.}}}{T_{\text{liq.}}} \right)^{1/2}, \quad (4)$$

$$u_{r_{\text{OHTC}}} = \left( \left[ \frac{\Delta\dot{Q}}{\dot{Q}} + \frac{\Delta T_{\text{wall}}}{T_{\text{wall}}} + \frac{\Delta T_{\text{liq.in}}}{T_{\text{liq.in}}} + \frac{\Delta T_{\text{liq.out}}}{T_{\text{liq.out}}} + \frac{\Delta W}{W} \right]_{\text{water}} + \left[ \frac{\Delta\dot{Q}}{\dot{Q}} + \frac{\Delta T_{\text{wall}}}{T_{\text{wall}}} + \frac{\Delta T_{\text{liq.in}}}{T_{\text{liq.in}}} + \frac{\Delta T_{\text{liq.out}}}{T_{\text{liq.out}}} + \frac{\Delta W}{W} \right]_{\text{nanofluid}} \right)^{1/2}. \quad (5)$$

The accuracy of density, steel ruler, power supply, and flow meter was ±0.001 g/cm<sup>3</sup>, ±1 mm, ±0.1 W, and ±0.02 L/min, respectively. The maximal value of the uncertainty of experimental conditions of settling rate, heat conductivity rate, and overall heat transfer capacity ratio was ±12.6%, ±16.3% and ±28.9%, respectively, on the basis of forgoing formulas (2)–(4). Thus, the uncertainty of the experiment can be controlled at lower than ±12.6%, ±16.3%, and ±28.9%, respectively.

## 4. Results and Discussion

Figure 2 shows the behavior change of zeta potential of the cationic chitosan dispersant in different concentrations. The figure indicated that cationic chitosan dispersant did increase the zeta potential of nanofluid up to 24%–30%. However, the relationship between the additive amount of dispersant and zeta potential was not proportional; redundant dispersant might depress the zeta potential. The experimental result of the zeta potential suggested that dispersant did improve the dispersion of nanoparticles in fluids, whereas, particle suspension was also influential to the application of nanofluid, in which better dispersion and suspension would increase

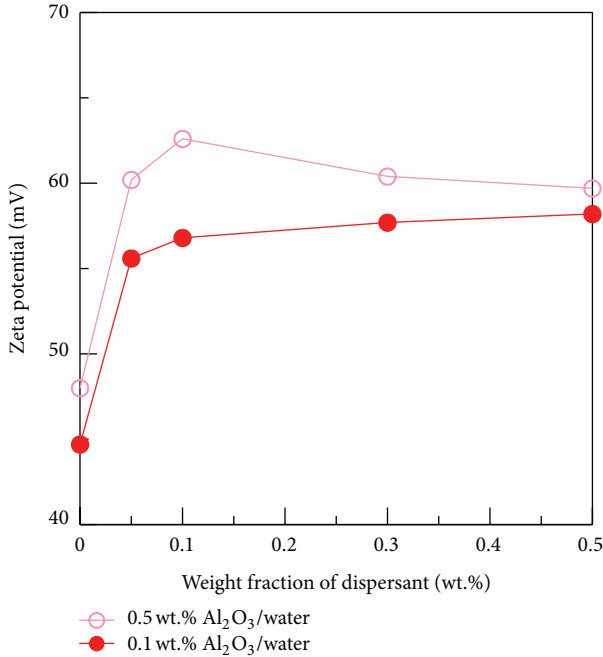


FIGURE 2: Correlation between zeta potential and weight fraction of dispersant.

the stability and heat conductivity of nanofluid. Figures 3 and 4, respectively, indicate the precipitation of 0.5 wt.% and 1.0 wt.% Al<sub>2</sub>O<sub>3</sub>/water nanofluid in different dispersant concentrations in 20 days. The figures show that the sample with 0.5 wt.% dispersant had the most severe precipitation, while the sample with 0.05 wt.% dispersant reached better suspension; the maximum settling rates were, respectively, 0.21% and 0.26%. Considering agglomeration and precipitation, Al<sub>2</sub>O<sub>3</sub>/water nanofluid with 0.05 wt.% cationic chitosan dispersant was selected as the working fluid for the following procedures.

Figure 5 indicates the increment of heat conductivity ratio at different temperatures. Nanofluid with no dispersant had the most increment of heat conductivity at the same temperature and powder concentration; dispersant may drop the heat conductivity ratio and block the increment of heat conductivity by adding the nanoparticles to the fluid. 1.0 wt.% Al<sub>2</sub>O<sub>3</sub>/water nanofluid with no dispersant and 1.0 wt.% Al<sub>2</sub>O<sub>3</sub>/water nanofluid with cationic chitosan dispersant, respectively, reached 14.2% and 12.6% of conductivity increment compared with the deionized water at the temperature of 55°C. The nanofluids, respectively, reached 4.8% and 4.1% of conductivity increment at the temperature of 15°C.

Dispersion of and suspension of nanoparticles and pipe blockage may be influential to the practical application of nanofluid. Table 2 is the component analysis and surface distribution on the copper surface after 40 hours of relative operation with the nanofluid with no dispersant and with the nanofluid with 0.05 wt% cationic chitosan dispersant. Powder particles on the surface of copper pipe could be clearly seen after operating the nanofluid with no dispersant. Fluid with higher powder concentration had more significant

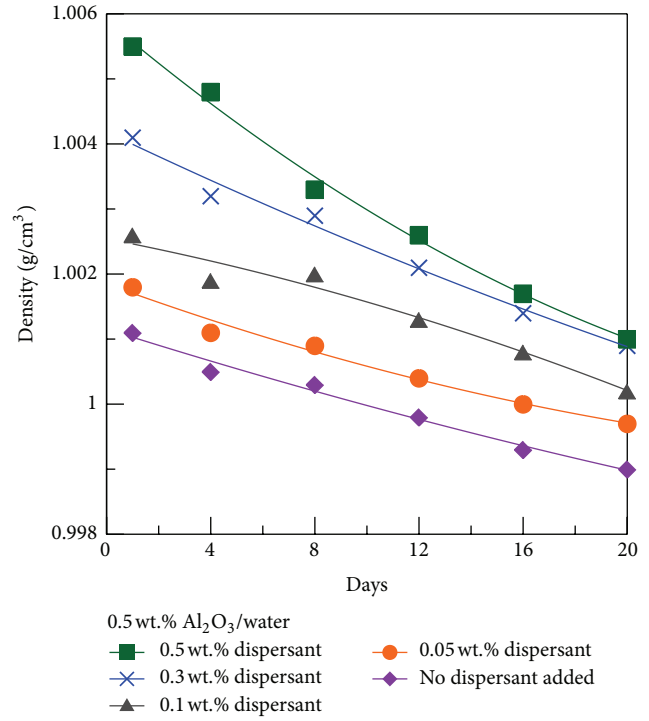


FIGURE 3: Correlation between weight concentration and precipitation behavior (0.5 wt.% Al<sub>2</sub>O<sub>3</sub>/water).

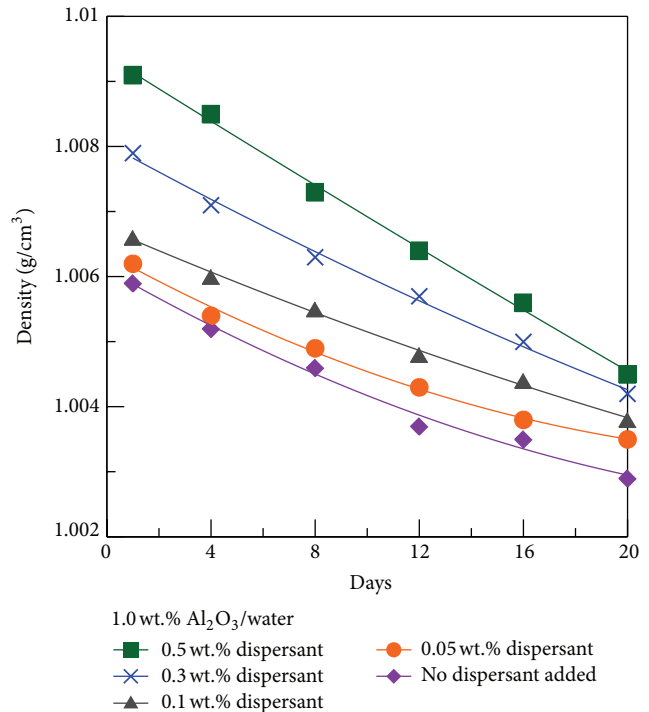
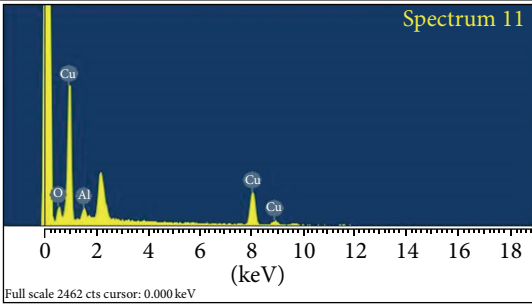
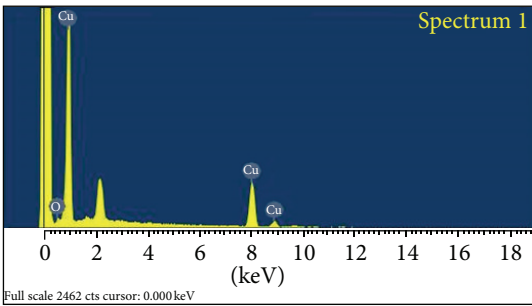
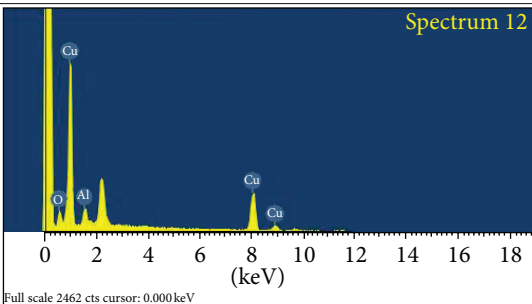
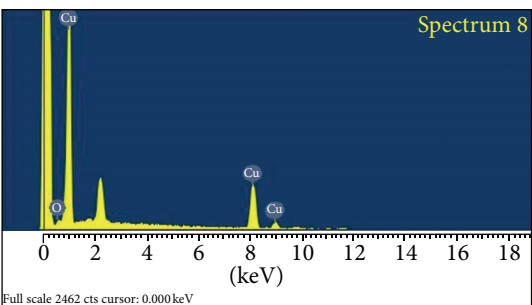


FIGURE 4: Correlation between weight concentration and precipitation behavior (1.0 wt.% Al<sub>2</sub>O<sub>3</sub>/water).

TABLE 2: Analysis of the component of copper surface in operation.

Concentration of nanofluid	Dispersant added	Surface distribution	Component analysis
0.5 wt.% Al <sub>2</sub> O <sub>3</sub> /water	No dispersant added		
	0.05 wt.% cationic chitosan dispersant added		
1.0 wt.% Al <sub>2</sub> O <sub>3</sub> /water	No dispersant added		
	0.05 wt.% cationic chitosan dispersant added		

trend of particle adhesion on the surface. The surface of copper pipe had no significant powder particle adhesion after operating the nanofluid with dispersant. The study employed energy dispersive spectrometer to analyze the surface of copper, showing that nondispersant fluid sample resulted in the aluminum adhering to the surface of copper, but fluid with cationic chitosan dispersant prevented the aluminum from adhering to the surface of copper. The results suggested that nanofluid with cationic chitosan dispersant effectively reduced the possibility of nanoparticles adhering to the surface of copper and copper wall. This result also estimated that nanofluid with cationic chitosan dispersant reduced agglomeration in the pipeline in practical system operation.

Figures 6, 7, 8, and 9, respectively, indicate the increasing trend of the overall heat transfer capacity ratio of nanofluid at different flow rates and heating power. The results suggested that the increasing trend of the overall heat transfer capacity ratio resembled the heat conductivity ratio. Deionized nanofluid without dispersant showed higher increasing trend than deionized nanofluid with cationic chitosan dispersant under all operating conditions, but difference in trends of the overall heat transfer capacity ratio was less significant in the same power concentration than in trends of thermal conductivity ratio analysis. The dispersant improved the agglomeration and suspension of nanofluid, so the contact area and convection of heat exchange were promoted. The

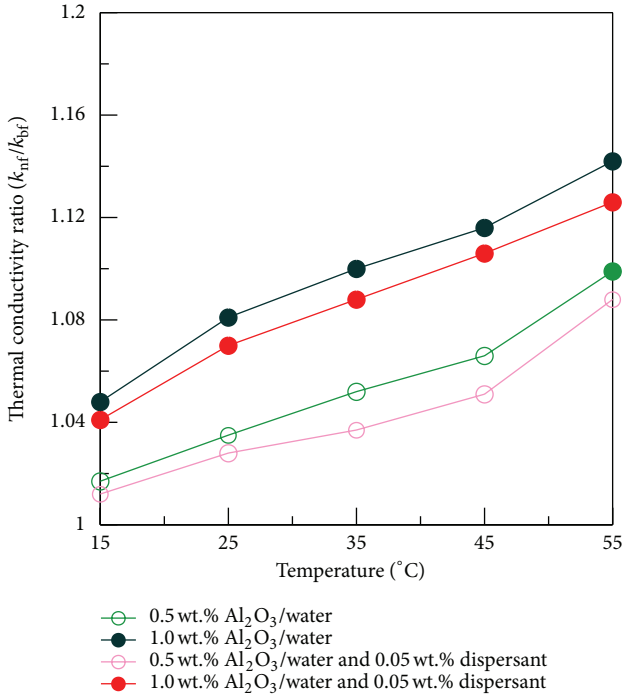


FIGURE 5: Correlations between temperature and thermal conductivity.

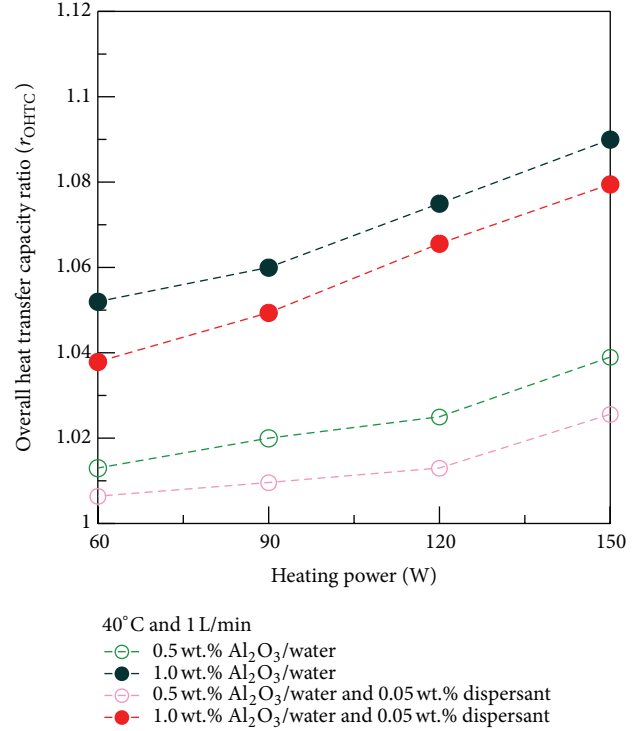


FIGURE 7: Increment of overall heat transfer capacity (40°C and 1L/min).

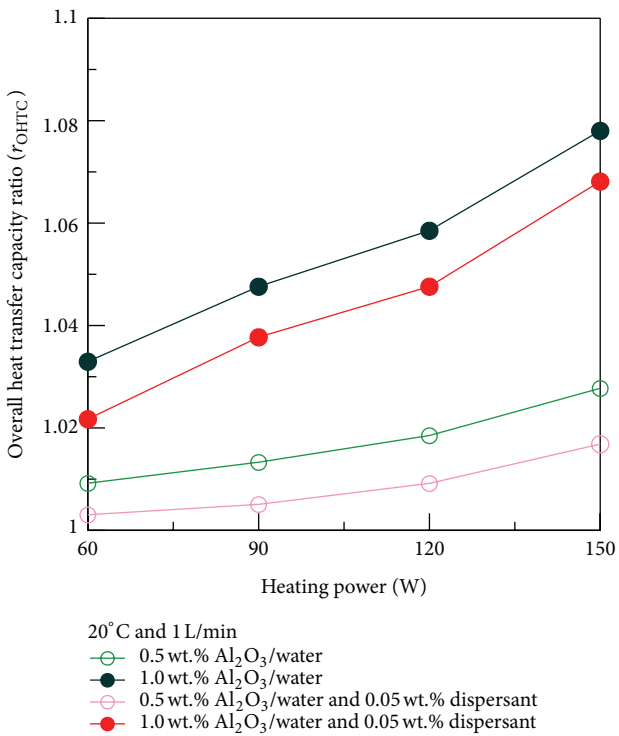


FIGURE 6: Increment of overall heat transfer capacity (20°C and 1L/min).

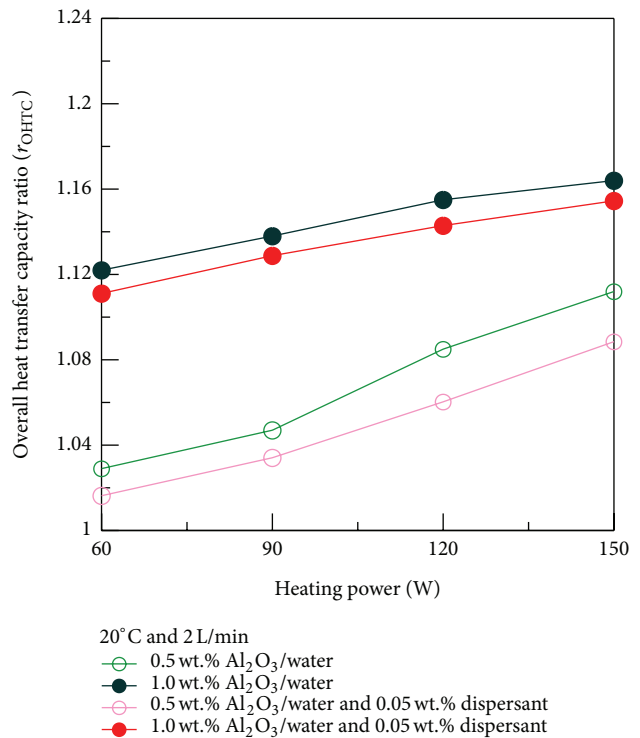


FIGURE 8: Increment of overall heat transfer capacity (20°C and 2L/min).

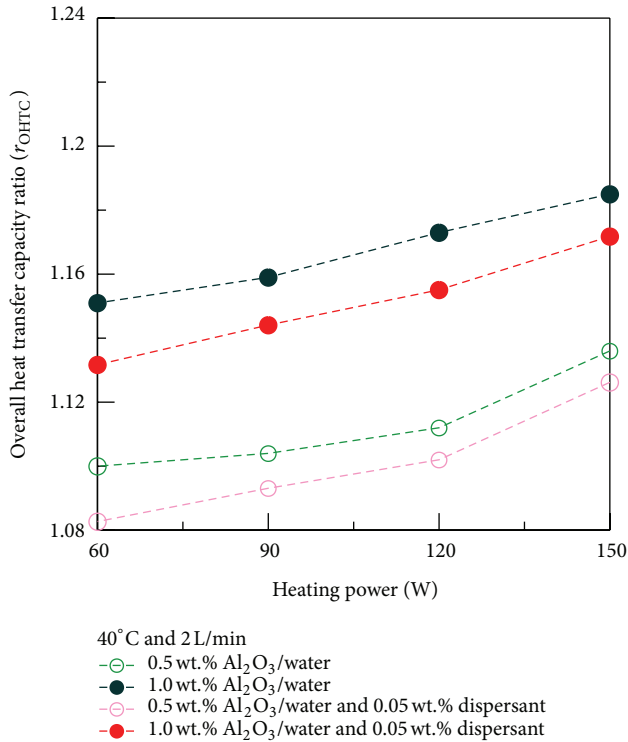


FIGURE 9: Increment of overall heat transfer capacity (40°C and 2 L/min).

overall heat transfer capacity ratio of 1.0 wt.% Al<sub>2</sub>O<sub>3</sub>/water nanofluid with 0.05 wt.% cationic chitosan dispersant was 17.4% at the flow ratio of 2 L/min heated by 150 W power and 8.3% heated by 60 W power.

## 5. Conclusions

Adding appropriate amount of cationic chitosan dispersant to the Al<sub>2</sub>O<sub>3</sub>/water nanofluid yielded the following results.

- (1) It improved the agglomeration and precipitation of nanofluid by elevating the dispersion and suspension of nanofluid.
- (2) It effectively reduced the risks of pipe blockage resulting from nanoparticles adhering to the pipe wall in the process of operation.
- (3) Comparing with deionized water, the 1.0 wt.% Al<sub>2</sub>O<sub>3</sub>/water nanofluid had, respectively, 4.1% and 12.6% thermal conductivity at the temperature of 15°C and 55°C. At the flow ratio of 2 L/min, increment of overall heat transfer capacity, respectively, reached 8.3% and 17.4% when the nanofluid was heated by 60 W power and 150 W power.

## Acknowledgment

This project is financially sponsored by the National Science Council under Grant NSC-98-2221-E-027-088-MY3.

## References

- [1] Y. H. Hung, T. P. Teng, and B. G. Lin, "Evaluation of the thermal performance of a heat pipe using alumina nanofluids," *Experimental Thermal and Fluid Science*, vol. 44, pp. 504–511, 2013.
- [2] T. Yousefi, F. Veysi, E. Shojaeizadeh, and S. Zinadini, "An experimental investigation on the effect of Al<sub>2</sub>O<sub>3</sub>/H<sub>2</sub>O nanofluid on the efficiency of flat-plate solar collectors," *Renewable Energy*, vol. 39, no. 1, pp. 293–298, 2012.
- [3] D. P. Kulkarni, R. S. Vajjha, D. K. Das, and D. Oliva, "Application of aluminum oxide nanofluids in diesel electric generator as jacket water coolant," *Applied Thermal Engineering*, vol. 28, no. 14–15, pp. 1774–1781, 2008.
- [4] C.-S. Jwo, L.-Y. Jeng, T.-P. Teng, and C.-C. Chen, "Performance of overall heat transfer in multi-channel heat exchanger by alumina nanofluid," *Journal of Alloys and Compounds*, vol. 504, pp. S385–S388, 2010.
- [5] G. Huminic and A. Huminic, "Application of nanofluids in heat exchangers: a review," *Renewable and Sustainable Energy Reviews*, vol. 16, pp. 5625–5638, 2012.
- [6] Y.-H. Hung, T.-P. Teng, T.-C. Teng, and J.-H. Chen, "Assessment of heat dissipation performance for nanofluid," *Applied Thermal Engineering*, vol. 32, no. 1, pp. 132–140, 2012.
- [7] S. U. S. Choi and J. A. Eastman, "Enhancing thermal conductivity of fluids with nanoparticles," in *Proceedings of the International Mechanical Engineering Congress and Exhibition*, San Francisco, Calif, USA, 1995.
- [8] J. A. Eastman, U. S. Choi, S. Li, L. J. Thompson, and S. Lee, "Enhanced thermal conductivity through the development of nanofluids," *Materials Research Society Symposium*, vol. 457, pp. 9–10, 1997.
- [9] S. Lee, S. U.-S. Choi, S. Li, and J. A. Eastman, "Measuring thermal conductivity of fluids containing oxide nanoparticles," *Journal of Heat Transfer*, vol. 121, no. 2, pp. 280–288, 1999.
- [10] X. Wang, X. Xu, and S. U. S. Choi, "Thermal conductivity of nanoparticle—fluid mixture," *Journal of Thermophysics and Heat Transfer*, vol. 13, no. 4, pp. 474–480, 1999.
- [11] Y. Xuan and Q. Li, "Heat transfer enhancement of nanofluids," *International Journal of Heat and Fluid Flow*, vol. 21, no. 1, pp. 58–64, 2000.
- [12] J. A. Eastman, S. U. S. Choi, S. Li, W. Yu, and L. J. Thompson, "Anomalous increased effective thermal conductivities of ethylene glycol-based nanofluids containing copper nanoparticles," *Applied Physics Letters*, vol. 78, no. 6, pp. 718–720, 2001.
- [13] C. H. Li and G. P. Peterson, "Experimental investigation of temperature and volume fraction variations on the effective thermal conductivity of nanoparticle suspensions (nanofluids)," *Journal of Applied Physics*, vol. 99, no. 8, Article ID 084314, 2006.
- [14] D.-H. Yoo, K. S. Hong, and H.-S. Yang, "Study of thermal conductivity of nanofluids for the application of heat transfer fluids," *Thermochimica Acta*, vol. 455, no. 1–2, pp. 66–69, 2007.
- [15] C. H. Li and G. P. Peterson, "The effect of particle size on the effective thermal conductivity of Al<sub>2</sub>O<sub>3</sub>-water nanofluids," *Journal of Applied Physics*, vol. 101, no. 4, Article ID 044312, 2007.
- [16] K.-F. V. Wong and T. Kurma, "Transport properties of alumina nanofluids," *Nanotechnology*, vol. 19, no. 34, Article ID 345702, 2008.
- [17] S. E. B. Maiga, C. T. Nguyen, N. Galanis, and G. Roy, "Heat transfer behaviours of nanofluids in a uniformly heated tube," *Superlattices and Microstructures*, vol. 35, no. 3–6, pp. 543–557, 2004.

- [18] S. E. B. Maiga, S. J. Palm, C. T. Nguyen, G. Roy, and N. Galanis, "Heat transfer enhancement by using nanofluids in forced convection flows," *International Journal of Heat and Fluid Flow*, vol. 26, no. 4, pp. 530–546, 2005.
- [19] S. K. Das, N. Putra, P. Thiesen, and W. Roetzel, "Temperature dependence of thermal conductivity enhancement for nanofluids," *Journal of Heat Transfer*, vol. 125, no. 4, pp. 567–574, 2003.
- [20] C. H. Chon and K. D. Kihm, "Empirical correlation finding the role of temperature and particle size for nanofluid ( $\text{Al}_2\text{O}_3$ ) thermal conductivity enhancement," *Applied Physics Letters*, vol. 87, no. 15, Article ID 153107, pp. 1–3, 2005.
- [21] C. Kang, M. Okada, A. Hattori, and K. Oyama, "Natural convection of water-fine particle suspension in a rectangular vessel heated and cooled from opposing vertical walls (classification of the natural convection in the case of suspension with a narrow-size distribution)," *International Journal of Heat and Mass Transfer*, vol. 44, no. 15, pp. 2973–2982, 2001.
- [22] X.-J. Wang, O.-S. Zhu, and S. Yang, "Investigation of pH and SDBS on enhancement of thermal conductivity in nanofluids," *Chemical Physics Letters*, vol. 470, no. 1–3, pp. 107–111, 2009.
- [23] W. Yu and H. Xie, "A review on nanofluids: preparation, stability mechanisms, and applications," *Journal of Nanomaterials*, vol. 2012, Article ID 435873, 17 pages, 2012.
- [24] D. S. Zhu, X. F. Li, N. Wang, X. J. Wang, J. W. Gao, and H. Li, "Dispersion behavior and thermal conductivity characteristics of  $\text{Al}_2\text{O}_3$ - $\text{H}_2\text{O}$  nanofluids," *Current Applied Physics*, vol. 9, no. 1, pp. 131–139, 2009.
- [25] K. Wusiman, H. Jeong, K. Tulugan, H. Afrianto, and H. Chung, "Thermal performance of multi-walled carbon nanotubes (MWCNTs) in aqueous suspensions with surfactants SDBS and SDS," *International Communications in Heat and Mass Transfer*, vol. 41, pp. 28–33, 2013.
- [26] R. Mondragon, J. E. Julia, A. Barba, and J. C. Jarque, "Characterization of silica-water nanofluids dispersed with an ultrasound probe: a study of their physical properties and stability," *Powder Technology*, vol. 224, pp. 138–146, 2012.
- [27] D. D. Ebbing and S. D. Gammon, *General Chemistry*, Cengage, 2013.
- [28] S. K. Das, S. U. S. Choi, W. Yu, and T. Pradeep, *Nanofluids Science and Technology*, John Wiley & Sons, 2008.

## Research Article

# Pool Boiling of Micro-/Nanoparticles Modified Aluminum Surface

**Chin-Ting Yang and Chia-Cheng Yu**

*St. John's University 499, Section 4, Tam King Road Tamsui, New Taipei City 25135, Taiwan*

Correspondence should be addressed to Chin-Ting Yang; [ctyang@mail.sju.edu.tw](mailto:ctyang@mail.sju.edu.tw)

Received 15 September 2013; Accepted 9 November 2013

Academic Editor: Ching-Song Jwo

Copyright © 2013 C.-T. Yang and C.-C. Yu. This is an open access article distributed under the Creative Commons Attribution License, which permits unrestricted use, distribution, and reproduction in any medium, provided the original work is properly cited.

The purpose is to investigate the boiling heat transfer affected by different wettability aluminum surfaces. The hydrophobic and hydrophilic surfaces were modified from regular surfaces by sol-gel method. The water contact angles of sample surfaces are 150, 75, and 5 degrees. All the samples were tested by a carefully designed thermal system. The experimental results revealed that, at the same wall superheat condition, the hydrophilic surface had higher boiling heat flux and hydrophobic surface possessed the lowest. The boiling bubble generation images suggested that bubble formation rate and shape strongly affected the values of heat flux. The lower contact angle surface generated fewer bubbles at high heat flux state such that liquid could contact with larger part of solid interface and transfer more heat than other kinds of surfaces. For the high contact angle surface, at very high heat flux condition, the bubbles even collapsed into vapor film. Part of heat transferred to liquid was blocked by the film and caused the wall superheat to increase dramatically and finally damaged the sample. This heat flux limitation was called critical heat flux. The hydrophilic surface that possessed higher critical heat flux was also measured in this study.

## 1. Introduction

A lot of heat could be transferred to liquid through the heating surface during pool boiling heat transfer. The temperature of fluid remained saturated and the superheat of heating surface changed with the heat flux [1]. The maximum heat flux of boiling curve where wall superheat was going to increase dramatically was called critical heat flux (CHF). And the heating surface wettability is one of the important factors that affect CHF [2]. Also bubbles generated from heating surface were easily observed during pool boiling heat transfer. The number and size of bubbles affect heat flux significantly. Since to enhance the pool boiling heat transfer is an important issue for high power density cooling system, there are many researchers focusing on studying the relationship between CHF and wettability. But most of them concentrated on the copper surfaces [3]. However, considering the lighter density and easy manufacturing of aluminum material, there are also many cooling systems harnessing those characteristics to solve the heat dissipation problems, for example, heat pipe, vapor chamber, and evaporator heat exchanger.

Jo et al. [4] used E-Beam to deposit platinum thin film as heater on one side of water and the other side modified as sample surface. The sample surfaces included regular water surface whose water contact angle was 54° and also was called hydrophilic. And the other sample surface was modified by MEMS processes to coat hydrophobic material, Teflon, with patterned structures. The contact angle was 123° (called as hydrophobic). They concluded that under very low heat flux transfer condition, the hydrophobic surface offered better nucleate boiling heat transfer. Also, a heterogeneous wettability surface provided better nucleate boiling heat transfer than that of the homogeneous ones. Hsu et al. [3] modified the copper surfaces to be with homogeneous or interlaced wettability by nanoparticles self-assembly method. Experimented with home-made setup, they observed the CHF of heating surfaces from high to low were interlaced, iso-hydrophilic, regular, and iso-hydrophobic surfaces. Phan et al. [5] also used nanocoating techniques to modify the regular steel surfaces to form different wettability. The surface contact angles varied from 20° to 110°. Due to the disagreement of results with classic model, they proposed macro-and micro contact angle

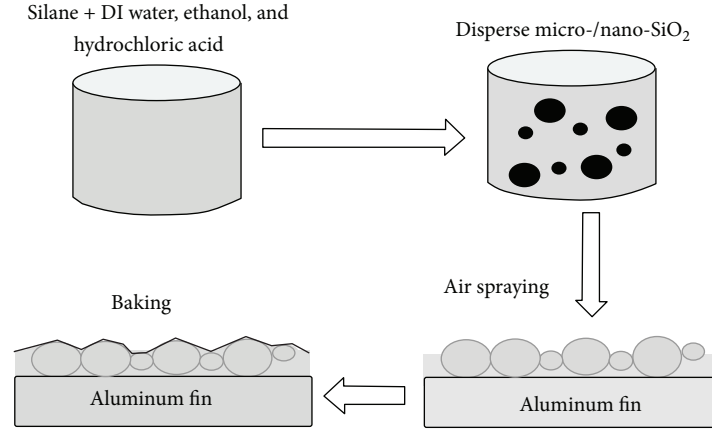


FIGURE 1: Illustration of surface modification processes.

model to explain the observed phenomenon. In this study, regular aluminum surfaces were modified to be hydrophobic or hydrophilic by self-assembly method. In order to improve the uniformity and the adhesion of particles, dipping process was replaced by air spraying. After surfaces modification, the samples were attached to the thermal test system and measured the boiling heat transfer flux against heating surface superheat. The temperature data and bubbles generation or vapor film formation images were taken for discussion.

## 2. Materials and Methods

**2.1. Aluminum Surface Modification.** The different wettability aluminum surfaces were modified by the self-assembly method. The rough structures were formed on surface with particles of dual sizes of diameters and silane acting as coupler. In the modification processes the dipping was replaced by air spraying in order to form firm structure on surface. The hydrophobic surface of rough structure in micro-/nanoscales was first reported by Barthlott and Neinhuis [6]. But the theory was proposed much earlier. Young [7] stated that when a liquid drops on a flat homogeneous solid surface, the contact angle was decided by the balance of surface tension forces which are between the solid, liquid, and vapor. The relation was expressed as

$$\cos \theta = \frac{\gamma_{SV} - \gamma_{SL}}{\gamma_{LV}}, \quad (1)$$

where  $\theta$  is contact angle in degree;  $\gamma_{SV}$  is surface tension, and the subscripts S, L, and V represent solid, liquid, and vapor respectively. If the surface was with roughness rather than plan, Cassie and Baxter [8] modified Young's expression as

$$\cos \theta_C = f_1 \cos \theta_1 + f_2 \cos \theta_2, \quad (2)$$

where  $\theta_C$  is contact angle predicted by Cassie-Baxter model  $f_1$  and  $f_2$  are fractions of solid and air inside an interval length of roughness.  $\theta_1$  is contact angle predicted by Young's model. When a water drop is in air,  $\theta_2$  is  $180^\circ$ . As predicted by Cassie-Baxter model, different wettability surfaces could be obtained by forming rough-structure on surfaces

and controlling the ratio of micro- and nanoparticles. The modification processes were illustrated in Figure 1. The first step was to mix methyltrimethoxysilane (METMS), distilled (DI) water, ethanol, and some Hydrochloric Acid, to form solution, and then uniformly dispersed (by ultrasonic vibrator) micro-/nano silica dioxide particles into the solution. The following procedure was to clean to and airspray the gel-like solution onto the aluminum surface. The final step was to put the sample into oven to bake it with some pre-set temperature cycles. The water contact angles of modified surfaces were measured by contact angle goniometer (model 100SL, Sindatek, Taiwan). With the analysis of the provided software, the measurement accuracy could be within 1 degree. The contact angles showed in this paper were the average of nine measurements at different locations for each sample.

**2.2. Thermal System.** The heating system used to measure the heat transfer flux of aluminum surfaces is shown schematically in Figure 2. There are three-nominal power of 200 W heaters inside the heating copper cylinder. The diameter of heating cylinder is 60 mm. The AC line is connected to voltage regulator and the output current flows through power meter and finally into heaters. Such that power supplied from power control unit could be controlled by regulating the voltage and read from the power meter panel. The heating surface is on the top of neck cylinder which is the same block of heating cylinder. The diameter of neck cylinder is 19 mm, but the length is only 10 mm. And two K-type thermocouples (0.079 mm of wire diameter, TPK-0.1-40G, TECPEL, Taiwan) were placed inside this cylinder. The distance between the two thermocouples was 4 mm. The temperature reading collected by the data logger (DTM319, TECPEL, Taiwan) was transferred to PC for analysis. According to the Fourier law and under one-dimensional assumption,  $q$  the heat flux to heating surface could be calculated as

$$q = k \frac{T_1 - T_2}{\Delta z}, \quad (3)$$

where  $k = 402 \text{ W/m}^\circ\text{C}$  is thermal conductivity of copper,  $T_1$  and  $T_2$  are the temperatures measured by the two thermocouples, and  $\Delta z$  is the distance between two thermocouples.

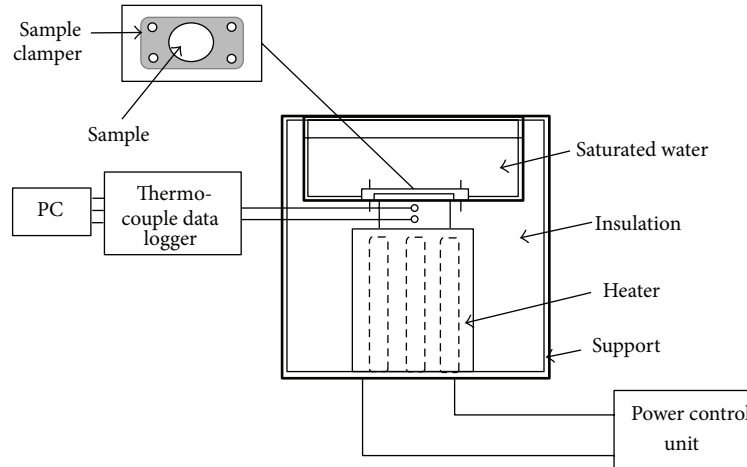


FIGURE 2: Schematic picture of heating system.



FIGURE 3: Aluminum surfaces of different wettability.

The top part of cylinder neck was brazed to a water container and the heating surface (top surface of neck cylinder) had the same level with bottom plate of container. Two other thermocouples were used (not shown in figure) to monitor the temperatures of water and interface between heating surface and water which both were kept at the saturated state during experiment. In order to minimize the thermal contact resistance, a copper cover plate with a hole of 19 mm diameter was used to fix the aluminum sample. The cover plate was fastened to the bottom plate by four screws. Also, thermal grease was applied between heating surface and sample. The temperature of sample surface was extrapolated by  $T_1$  and  $T_2$  with actual distances from surface. Insulating material was fully filled between water container and support box to reduce heat transfer to the surrounding area. One extra thermometer was attached to the surface of box to monitor the temperature change. By doing the energy balance analysis, the heat loss through insulation was proportional to heat transfer flux. The maximum heat loss was 3.1% of the power supplied.

### 3. Discussion and Result

**3.1. Hydrophobic and Hydrophilic Samples.** As predicted by Cassie and Baxter's model, formation of roughness structure on aluminum surface really did improve the water contact angle which meant to be more hydrophobic. In our modifications, METMS silane solution with addition of 9.6 wt% of silica oxide particles formed the best hydrophobic surface. The silica oxide particles included 80% of nanoparticles (99.5% diameter between 10 and 20 nm, Sigma-Aldrich, USA) and the rest of microparticles (80% diameter between 1 to 5  $\mu\text{m}$ ,

Sigma-Aldrich, USA). The contact angle changed from 75° to 150°, as shown in the left part of Figure 3. The SEM images shown in Figure 4 could reveal the microstructure dispersed on the modified aluminum surface and the higher resolution image also could show the nanostructure around the microparticles which was very similar to the lotus leaf structure [5]. The contact angle of regular plain aluminum surface is 75° which was also reported in many papers. The hydrophilic surface modification procedures were the same as those of the hydrophobic one, except one more high temperature baking. The bond attraction of METMS silane to water molecule is higher than to silica particles. The water drop laid flatly on the surface. The water contact angle was only 5°. Since the particles were deposited to the surface by air spraying, the adhesive force was stronger than the dipping method. Also the surface wettability could be kept longer for at least more than 1 year.

**3.2. Boiling Heat Flux of Copper Surface.** The heating cylinder was made of copper and the heating surface also can be as one sample surface. Without attaching any sample to the heating surface, the boiling heat transfer flux of copper surface could be tested. Water with temperature of near 100°C was added to the container. Power consumed by heaters was controlled by voltage regulator. Two temperatures inside the cylinder neck and two inside the water container were recorded by PC. The temperature curves were shown in Figure 5. After a period of time, the two temperatures, top and bottom liquid temperatures, inside the water container were approaching 100°C. And the other two temperatures were approaching two steady values which were  $T_1$  and  $T_2$  in (3). The one far

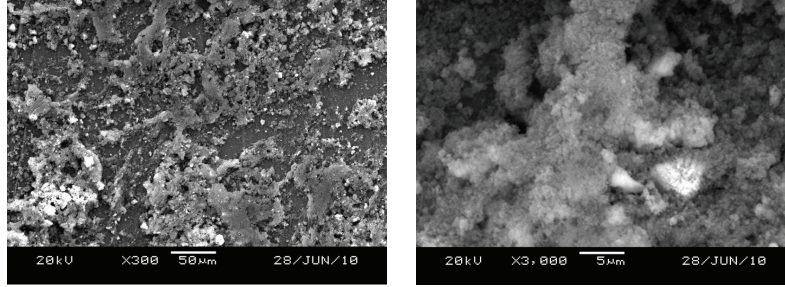


FIGURE 4: Low and high resolution SEM images of structure on surface (CA = 150°).

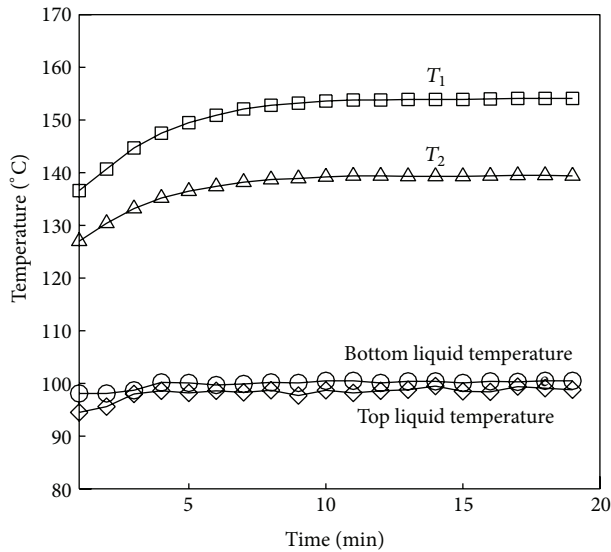


FIGURE 5: Temperature curves for one heat flux experiment.

away heating surface was called  $T_1$ , such that the heat flux transferred to heating surface could be calculated by (3). However, the calculated heat flux was smaller than that of direct reading from power meter, because part of the heat still could dissipate to the surrounding through the insulation material. But the calculated heat flux must be very close to the heat flux through heating surface for the short length design of cylinder neck. For all test cases, the maximum heat flux dissipated to surrounding was 3.1%. The heat flux in this study was all calculated from (3). The heating surface temperatures employed similar equation to extrapolate. At the interface of heating surface and water, the temperature was kept the same as liquid. This was the reason why it was not easy to measure the wall temperature directly. However, assuming the heat flux was conservative in short length cylinder, it was much easier to extrapolate the wall temperature and calculate the wall superheat. If any test sample plate was attached to the heating surface, the thermal conductivity in (3) should be modified as composite material. Figure 6 was the comparison of copper surface boiling heat flux curve with Hsu et al. [3]. The trend was very similar. The contact angle of our regular copper surface was 85°, but it was 73° for Chen's sample. For our system, if the heat flux was too low, the voltage regulator

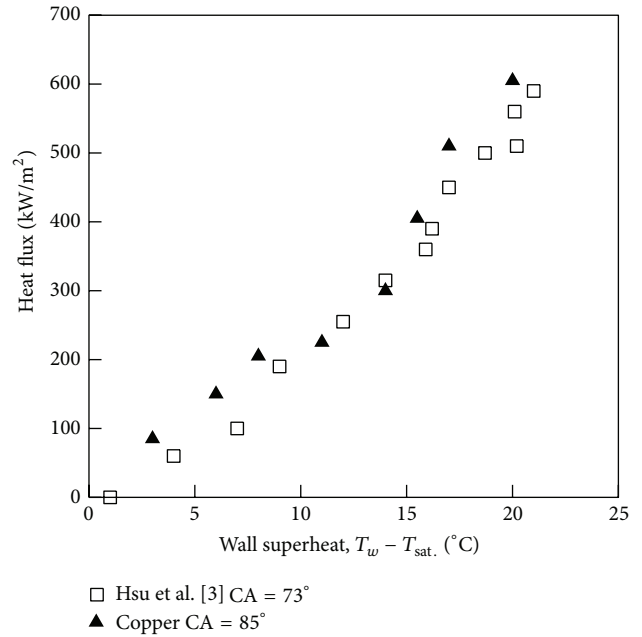


FIGURE 6: Comparison of copper surface boiling heat flux curve with Hsu et al. [3].

was hard to control. The two temperatures  $T_1$  and  $T_2$  were close and hard to determine. So there was a lower limitation to measure the heat flux.

**3.3. Boiling Curves of Aluminum Surfaces.** The aluminum surface's heat flux against wall superheat plots were shown in Figure 7. The opened circle symbol line represented boiling curve of hydrophobic surface. In comparison with copper surface (Figure 6), if both are at the same heat flux the wall superheats of aluminum surfaces are much higher. The reason was that the thermal conductivity of aluminum was smaller than that of copper. For aluminum surface, according to (3), the smaller thermal conductivity needs higher temperature gradient to keep the same heat flux. From the plot, CHF of hydrophobic surface was 603 kW/m<sup>2</sup> when the surface superheat was 163°C. The solid square symbol line was the heat flux curve for regular aluminum surface. Being close to the hydrophobic curve, when the wall superheat reached 186°C the boiling heat flux rise was

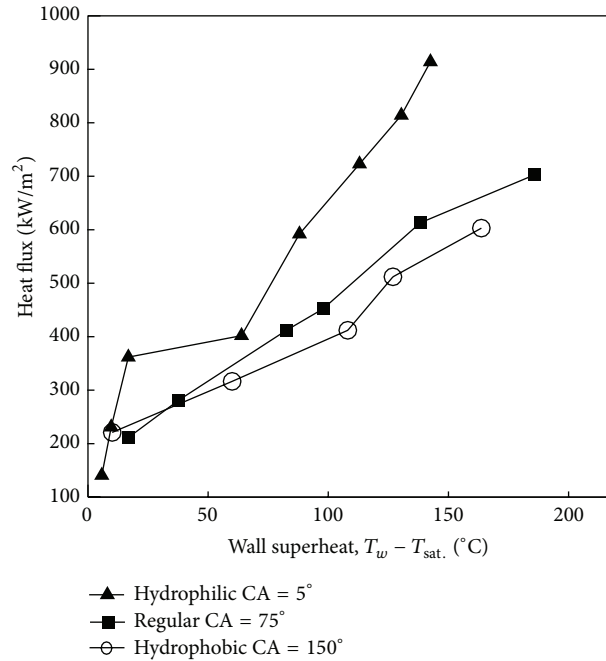


FIGURE 7: Wall superheat and heat flux plots for different wettability surfaces.

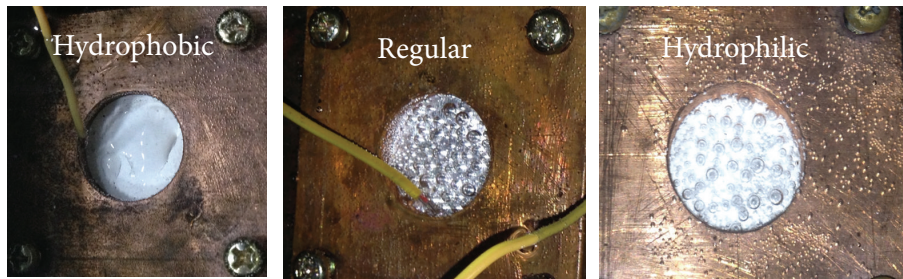


FIGURE 8: Film or bubbles formed during boiling heat transfer for different wettability surfaces.

as high as 703 kW/m<sup>2</sup>. Larger than this wall superheat, the boiling condition turned into being unstable gradually. If only the heat flux slightly increased, the wall superheat then would have been increasing very quickly. On the surface, part of the bubbles collapsed into vapor film and blocked the heat transfer into the liquid. Then, most of energy would heat up the aluminum sample and cause the wall superheat increase out of control. Finally, the temperature was over the limitation of material and damaged the sample. The solid delta symbol line represented the hydrophilic surface's boiling curve. At lower wall superheat, the boiling curve was steeper than others. There were few bubbles generated during this stage. If the wall superheats were between 17 and 64°C, the wall superheats increased dramatically with only a little increasing of heat flux. Higher bubbles generated rate was observed in this period of time. The CHF of the hydrophilic surface could reach as high as 914 kW/m<sup>2</sup> and the corresponding wall superheat was 143°C. Figure 8 showed the pictures which were taken at the boiling heat flux around 600 kW/m<sup>2</sup>. When the surface was hydrophilic, bubbles were

not as many as others. The saturated liquid still could contact with major part of heating area directly and transfer energy. The wall superheat was the lowest at this heat flux. For the regular aluminum surface, the contact angle was 75° and bubbles were generated easily. Most of the heating area was covered with small size bubbles. The bubbles prevented heat dissipation from surface into liquid and then increase the wall superheat. Compare to the hydrophilic surface, the wall superheat increased about 50°C at the same heat flux. When the surface was hydrophobic, very different phenomena were observed. The modified micro-/nanostructure trapped a lot of air to form hydrophobic characteristic. This kind of structure generated bubbles easily during boiling heat transfer. For higher heat flux case, even some bubbles collapsed into film and increased the wall superheat very much.

#### 4. Summary

Concluding the discussion, the sol-gel method successfully modified the regular aluminum surfaces to be hydrophobic

or hydrophilic. In this study the contact angles were  $150^\circ$  and  $5^\circ$ , respectively. The bubble number and size were smaller for the hydrophilic surface which let the saturated liquid contact with heating surface easily. This was a benefit to boiling heat transfer. Such that the boiling heat flux and CHF depended on the wettability of the surfaces. For regular aluminum the CHF was  $703 \text{ kW/m}^2$ , but for the hydrophilic surface the CHF could be as high as  $914 \text{ kW/m}^2$  and only was  $603 \text{ kW/m}^2$  of the hydrophobic surface.

## Acknowledgment

The authors would like to acknowledge the financial support provided by the National Science Council of Taiwan, under Contract no. NSC 101-2221-E-129-009.

## References

- [1] S. Nukiyama, "The maximum and minimum values of heat  $Q$  transmitted from metal to boiling water under atmospheric pressure," *Journal of the Japan Society of Mechanical Engineers*, vol. 37, pp. 367–374, 1934.
- [2] M. Maracy and R. H. S. Winterton, "Hysteresis and contact angle effects in transition pool boiling of water," *International Journal of Heat and Mass Transfer*, vol. 31, no. 7, pp. 1443–1449, 1988.
- [3] C. C. Hsu, T. W. Su, and P. H. Chen, "Pool boiling of nanoparticle-modified surface with interlaced wettability," *Nanoscale Research Letters*, vol. 7, pp. 259–266, 2012.
- [4] H. Jo, H. S. Ahn, S. Kang, and M. H. Kim, "A study of nucleate boiling heat transfer on hydrophilic, hydrophobic and heterogeneous wetting surfaces," *International Journal of Heat and Mass Transfer*, vol. 54, no. 25–26, pp. 5643–5652, 2011.
- [5] H. T. Phan, N. Caney, P. Marty, S. Colasson, and J. Gavillet, "How does surface wettability influence nucleate boiling?" *Comptes Rendus Mecanique*, vol. 337, no. 5, pp. 251–259, 2009.
- [6] W. Barthlott and C. Neinhuis, "Purity of the sacred lotus, or escape from contamination in biological surfaces," *Planta*, vol. 202, no. 1, pp. 1–8, 1997.
- [7] T. Young, "An essay on the cohesion of fluids," *Philosophical Transactions of the Royal Society of London*, vol. 95, pp. 65–87, 1805.
- [8] A. B. D. Cassie and S. Baxter, "Wettability of porous surfaces," *Transactions of the Faraday Society*, vol. 40, pp. 546–551, 1944.

## Research Article

# Multifunction of Ni/Ag Nanocompound Fluid

**Mu-Jung Kao**

*Department of Vehicle Engineering, National Taipei University of Technology, Taipei 10608, Taiwan*

Correspondence should be addressed to Mu-Jung Kao; [mjkao@ntut.edu.tw](mailto:mjkao@ntut.edu.tw)

Received 10 September 2013; Accepted 4 November 2013

Academic Editor: Ho Chang

Copyright © 2013 Mu-Jung Kao. This is an open access article distributed under the Creative Commons Attribution License, which permits unrestricted use, distribution, and reproduction in any medium, provided the original work is properly cited.

An arc-submerged nanoparticle synthesis system (ASNSS) is proposed and developed for fabricating Ni/Ag nanocompound fluid. In the development process, the positive and negative electrodes in the system are Ni and Ag, respectively. Applied electrical energy then produces heating source by generating an adequate arc with a high temperature that can melt and vaporize the two electrodes. The nanocompound fluid that is generated by the synthesis system is analyzed by morphological analysis, Zeta potential analysis, heat conductivity analysis, magnetic characteristic analysis, and UV-Vis absorption spectra analysis. Experimental results show that increasing the concentration of added particles and the higher temperature can be helpful to the enhancement of thermal conductivity. The Ni/Ag nanofluid not only preserves the magnetic character of the nickel and the ability of silver to absorb visible light but also enhances the thermal conductivity. The absorption occurs at 406 nm wavelength (redshift from 396 nm to 406 nm), which means that, under the excitement of visible light range (400~700 nm), it can let more easy electrons jump to the conductivity zone from the valence electron zone.

## 1. Introduction

Ni nanofluid is ferromagnetism and can be used to target drug to treat localized disease. The applications of nanomagnetic particles have recently been expanded to such fields as biomedicine, ferrofluids, data storage, and others. Clinically, drugs against cancer can be desorbed from [1]. Nickel, a magnetic material, is also widely used, in electrical generators, adaptors, tape recorders, and other devices [2, 3].

Considering metallic silver (Ag) as a multifunctional material, the antimicrobial effects of Ag ion or salts are well known; the National Aeronautics and Space Administration used silver containers to preserve the purity of drinking water on spacecraft in the 1970s. Silver foil was used to protect wounds from infection during World War I [4, 5].

In the fabrication process, the positive electrode uses an Ag rod and the negative electrode uses a Ni rod, and the two electrodes are processed in the dielectric liquid to form Ni/Ag nanofluid [5, 6]. Nanocomposite fluid is analyzed by morphological analysis, heat transfer analysis, and magnetic analysis. Nanocomposite fluid had a small size of a nanomaterial, and the number of atoms on its surface increases with its volume and the surface potential also increases and an increase in

the concentration of the added particles and temperature rise can be helpful to the enhancement of thermal conductivity [7, 8]. Furthermore, when the wavelength of illumination light is in the range of 410 nm~800 nm, the produced Ni/Ag nanocomposite fluid has stronger light absorbance.

## 2. Materials and Methods

Low-pressure control methods for ASNSS were proposed and developed for the Ni/Ag nanofluid, which is a suspension of nanoparticles in deionized water [6]. Figure 1 shows the schematic of fabrication system. The pressure control system uses the pressure differential created between the chamber bodies of the working chamber and collection chamber to induce the particles that become nucleus after vaporization into the collection chamber from the working chamber. The nanofluid collection system and cooling circulation system precondense the dielectric liquid to maintain a low temperature during the collection of nanofluid and further suppress the overgrowing and clustering of the particles.

The particles suspended in the loading solution will lower its reactivity in a low temperature environment and they will

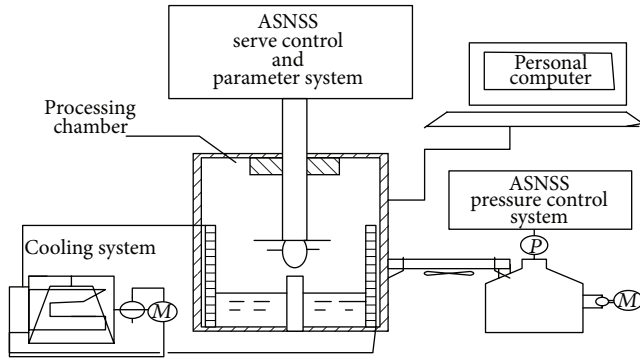


FIGURE 1: Schematic of fabrication system.

steadily become nuclei because of their difficulty in continuous growth, acquiring smaller nanoparticles. Finally, the collected Ni/Ag nanocomposite fluid is extracted for relative examination of its material properties.

The high energy produced by an electrical arc will vaporize the metal into vapor. The theory of droplet nucleus generated by vapor can be used to approximate the crystalline nucleus generated by balanced gas phase. Supersaturated vapor would generate cluster of molecular agglutination. Nucleation requires a considerable amount of undercooling to grow into a crystal. There are two kinds of free energy changes that must be considered: (1) the surface energy required to form the new solid surfaces and (2) the volume free energy released by the liquid-to-solid transformation. The free energy change,  $\Delta G$ , of the generated globe with radius of  $r$  during the process of clustering can be expressed as the following equation:

$$\Delta G = 4\pi r^2 \sigma + \frac{4}{3}\pi r^3 \Delta G_v \quad (1)$$

in which  $\sigma$  is the interfacial tension and  $\Delta G_v$  is the free energy change during the generation of unit dimensional liquid by the vapor. The process parameters of this device can be controlled by different working currents. A nanofluid collection system and cooling circulation system are used to precondense the deionized water so as to maintain a low temperature during the collection of nanofluid and further suppress the overgrowing and clustering of the particles. X-ray diffraction (MAC-MXP18) is used to obtain the pattern of nanoparticles. Through XRD analysis, the related XRD pattern of the nanocompound fluid under analysis is shown in Figure 2.

FE-SEM (EM0039) and a Decagon KD2 measure meter also are used to obtain the nanoparticles' images and the thermal conductivity. To analyze their magnetic properties, a Superconducting Quantum Interference Device Magnetometer (MPMS7) is used with magnetic field intensity set from  $-10^5$  to  $+10^5$  Gauss at  $25^\circ\text{C}$ . Meanwhile, Zeta meter is used to analyze the produced nanoparticle suspension and through UV-vis light absorption spectrum meter the absorbency can be tested.

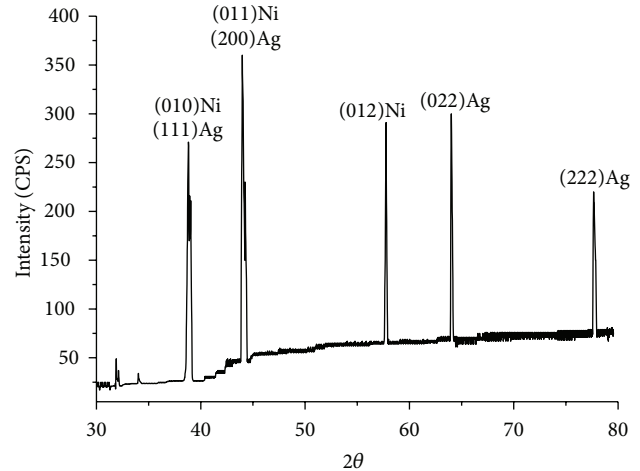


FIGURE 2: XRD pattern of nanocompound fluid.

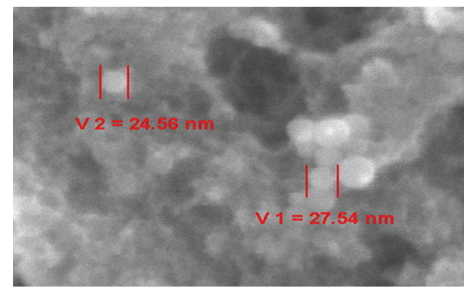


FIGURE 3: FE-SEM image showing the Ni approach to sphere.

### 3. Results and Discussion

Comparing the peaks generated in Figure 2, the compound fluid is associated with Ni and Ag. EDS and FEG-SEM are used to check the further identification and confirmation can check the fluid particle's components and appearance. Figure 3 shows that the Ni particles are in ionic state and will form metallic oxides after reacting with oxygen ions in water, which would form a more spherical shape. In Figure 4, the FEG-SEM shows the figure of nonoxidized Ag.

The Zeta potentials of mixed Ni/Ag nanocomposite fluids with different pH values are measured. The results in Figure 5 reveal that when the pH value of the produced nanofluid is about 9.6 and the Zeta potential carried on the particles is zero, this is called the isoelectric point (IEP). As the surface potential becomes farther from the IEP, the suspension becomes more stable.

When the pH value is greater than 9.6, the surfaces of the particles carry negative charge. Figure 6 plots the ratio of coefficient of thermal conductivity. A higher Ni/Ag nanofluid concentration is associated with higher thermal conductivity, clearly verifying that adding nanoparticles improves the coefficient of thermal conductivity of the working fluid. The effect of temperature can be evaluated as follows. When the temperature of the working fluid is  $10^\circ\text{C}$ , the curves of concentration (wt%) versus thermal conductivity coefficients

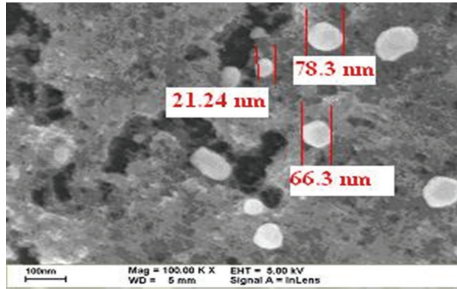


FIGURE 4: FE-SEM image showing the almost spherical Ag approach.

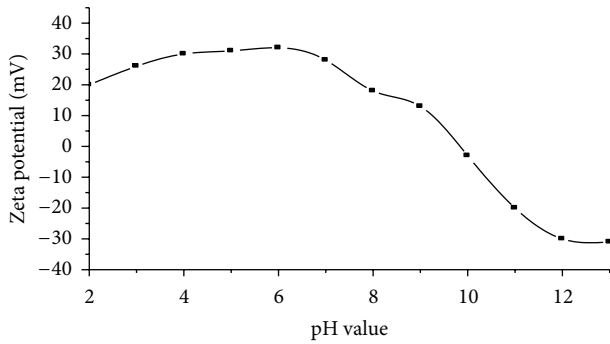


FIGURE 5: Zeta potential and the pH value.

approach linearity. At 30°C, the curve is similar to that at 40–60°C but with a steeper slope. When the temperature reaches 60°C, the curve’s slope becomes negative for 0.4% weight concentration. The weight concentration between 0.3 and 0.4% is in negative slope. It seems to the nanoparticle’s cluster due to temperature rising, especially in temperature at 60°C. The temperature dependence of the thermal conductivity enhancement is considered to be attributed to the variation of Brownian motion velocity for the particles. As the cluster is decreased, the effect of random motion becomes dominant. The experiment reveals that when the temperature exceeds 30°C and concentration (wt%) is over 0.3%, particles in the nanocompound fluid would aggregate to form sediment at a certain ratio, which will reduce the thermal conductivity of nanofluid. Overall, this experiment has shown that both temperature and concentration will have substantial influence on the thermal conductivity coefficient of a nanofluid. By comparing the rates of temperature rise and concentration (wt%) rise, the influence of thermal conductivity coefficient ratio to the rate of temperature rise is clear.

Figure 7 presents the UV-Vis absorption spectra of a suspension of silver nanoparticles and reveals that their absorbance is maximal at around 396 nm; this result has been confirmed elsewhere. The UV-Vis absorption spectrum of Ni/Ag nanofluid is redshifted and its absorbance is maximal at about 406 nm so it has greater ability to absorb visible light.

Figure 8 displays that the Ni/Ag nanofluid’s saturated magnetized amount at 0.895 emu/g is smaller than Ni nanofluid’s saturated magnetized amount at 0.905 emu/g and saturated strength is 1250 Oe. The hysteresis slopes are very close

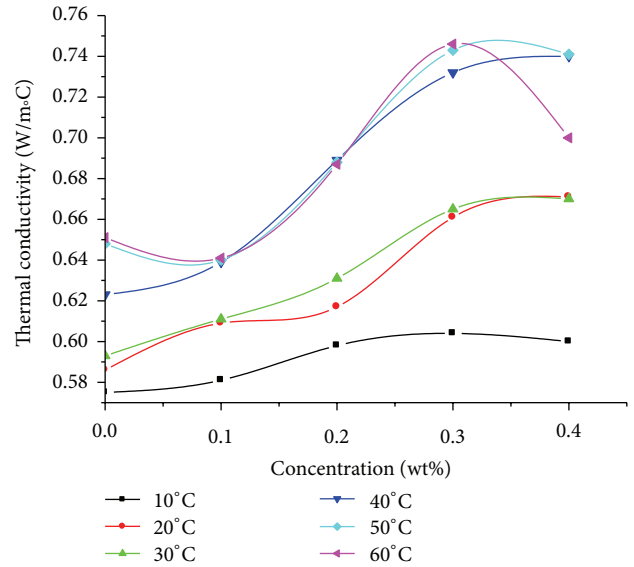


FIGURE 6: Weight concentration (wt%) versus thermal conductivity.

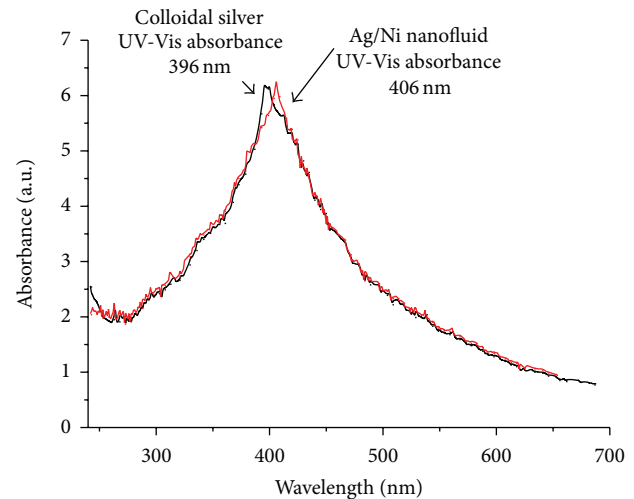


FIGURE 7: UV-Vis absorption spectra of colloidal silver and Ni/Ag nanofluid.

to each other. The residual magnetism and coercive force are close to zero, confirming that the magnetic particles are superparamagnetic particles. For 0.4% Ni/Ag weight concentration in this work, it is too small for saturated magnetized amount to change. That is, the reason for adding Ag in Ni did not improve the properties of Ni.

#### 4. Conclusions

Based on above results and analyses, we propose the following three conclusions concerning the Ni/Ag nanocompound fluid.

- (1) The thermal conductivity experiment confirmed that a higher Ni/Ag nanofluid concentration is associated

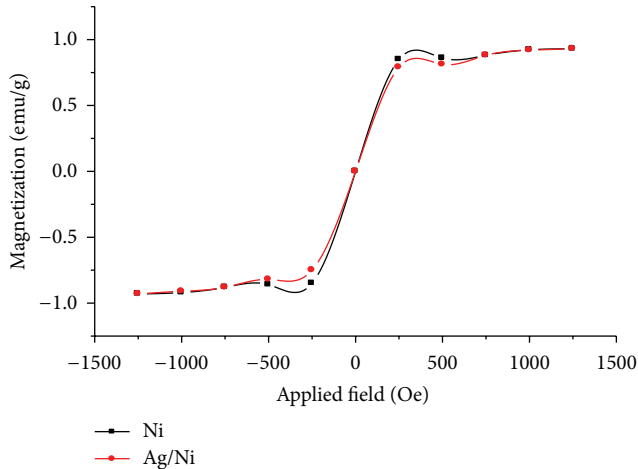


FIGURE 8: Hysteresis curve of Ni and Ni/Ag nanofluid.

with higher thermal conductivity and therefore better heat transfer.

- (2) Ni/Ag nanocompound fluid absorbs at 406 nm wavelength (redshifted from 396 nm to 406 nm), so it can be excited under visible light (400~700 nm).
- (3) Ni/Ag nanofluid has a residual magnetism and coercive force close to 0, confirming that its particles are superparamagnetic particles. The Ni/Ag nanofluid not only preserves the magnetic character of the nickel and the ability of silver to absorb visible light but also enhances the thermal conductivity.

## References

- [1] H. Chang, M. J. Kao, C. S. Jwo, C. G. Kuo, Y. H. Yeh, and W. C. Tzeng, "Preparation of Co/Ag nanocompound fluid using ASNSS with aid of ultrasonic orthogonal vibration," *Journal of Alloys and Compounds*, vol. 504, supplement 1, pp. S376–S379, 2010.
- [2] H. Chang and H. T. Su, "Synthesis and magnetic properties of Ni nanoparticles," *Reviews on Advanced Materials Science*, vol. 18, no. 7, pp. 667–675, 2008.
- [3] S. R. Norrby, C. E. Nord, and R. Finch, "Lack of development of new antimicrobial drugs: a potential serious threat to public health," *The Lancet Infectious Diseases*, vol. 5, no. 2, pp. 115–119, 2005.
- [4] D. C. Tien, K. H. Tseng, C. Y. Liao, and T. T. Tsung, "Identification and quantification of ionic silver from colloidal silver prepared by electric spark discharge system and its antimicrobial potency study," *Journal of Alloys and Compounds*, vol. 473, no. 1-2, pp. 298–302, 2009.
- [5] T. Tang, J. W. Zheng, B. Chen et al., "Effects of targeting magnetic drug nanoparticles on human cholangiocarcinoma xenografts in nude mice," *Hepatobiliary & Pancreatic Diseases International*, vol. 6, no. 3, pp. 303–307, 2007.
- [6] T. T. Tsung, H. Chang, L. C. Chen, M. K. Liu, and H. M. Lin, "Process development of a novel arc spray nanoparticle synthesis system (ASNSS) for preparation of a TiO<sub>2</sub> nanoparticle suspension," *The International Journal of Advanced Manufacturing Technology*, vol. 24, no. 11-12, pp. 879–885, 2004.

- [7] L. H. Bennett, L. Takacs, L. J. Swartzendruber, J. Weissmüller, L. A. Bendersky, and A. J. Shapiro, "Magnetic properties of mechanically alloyed Fe-Ni-Ag," *Scripta Metallurgica et Materiala*, vol. 33, no. 10-11, pp. 1717–1724, 1995.
- [8] P. Keblinski, S. R. Phillpot, S. U. S. Choi, and J. A. Eastman, "Mechanisms of heat flow in suspensions of nano-sized particles (nanofluids)," *The International Journal of Heat and Mass Transfer*, vol. 45, no. 4, pp. 855–863, 2002.

## Research Article

# Defect Study of MgO-CaO Material Doped with CeO<sub>2</sub>

Han Zhang, Huizhong Zhao, Jinfeng Chen, Jingjie Li, Jun Yu, and Jianhua Nie

The Hubei Province Key Laboratory of Ceramics and Refractories, Wuhan University of Science and Technology, 947 Heping Road, Wuhan 430081, China

Correspondence should be addressed to Han Zhang; wustzh@163.com

Received 2 May 2013; Accepted 19 August 2013

Academic Editor: Ho Chang

Copyright © 2013 Han Zhang et al. This is an open access article distributed under the Creative Commons Attribution License, which permits unrestricted use, distribution, and reproduction in any medium, provided the original work is properly cited.

MgO-CaO refractories were prepared using analytical reagent chemicals of Ca(OH)<sub>2</sub> and Mg(OH)<sub>2</sub> as starting materials and CeO<sub>2</sub> as dopant, then sintered at 1650°C for 3 h. The effect of CeO<sub>2</sub> powders on the defect of MgO-CaO refractories was investigated. The sample characterizations were analyzed by the techniques of XRD and SEM. According to the results, with the addition of CeO<sub>2</sub>, the lattice constant of CaO increased, and the bulk density of the samples increased while apparent porosity decreased. The densification of MgO-CaO refractories was promoted obviously. In the sintering process, MgO grains grew faster than CaO, pores at the MgO-CaO grain boundaries decreased while pores in the MgO grains increased gradually, and no pores were observed in the CaO grains. The nature of the CeO<sub>2</sub> promoting densification lies in the substitution and solution with CaO. Ce<sup>4+</sup> approaches into CaO lattices, which enlarges the vacancy concentration of Ca<sup>2+</sup> and accelerates the diffusion of Ca<sup>2+</sup>.

## 1. Introduction

MgO-CaO refractories have been widely used in metallurgy industry [1] and cement rotary kilns [2] owing to their excellent properties such as high melting points, excellent thermal shock resistance, and slag corrosion resistance [3]. They have also been considered as one type of chrome-free refractories that are suitable for substituting the MgO-Cr<sub>2</sub>O<sub>3</sub> refractories [4]. Furthermore, MgO-CaO refractories are beneficial to removing inclusions from molten steels; thus, they have been considered to be one of the effective refractory types for processing clean steel products [5, 6]. In recent years, with the increasing demands of molten steel purity, the awareness of environmental protection and resource shortage grows [7], and MgO-CaO materials have become one of the attractive steelmaking refractories because of their low cost and high ore reserves [8].

However, the application of MgO-CaO refractories has been limited by their poor hydration resistance [9, 10]. MgO-CaO materials are susceptible to hydration because the free lime in them can react easily with water, volume expansion of the resultant can cause severe damage to the materials.

The hydration resistance of free lime materials can be improved by treating them in a CO<sub>2</sub> atmosphere [11] which leads to the formation of a dense maskant on the surface

of CaO. Further improvement may be made by adding metal oxides such as CuO [12], Fe<sub>2</sub>O<sub>3</sub> [13], and SiO<sub>2</sub> [14] to react with lime to form a low-melting point phase or by adding ZrO<sub>2</sub> [15–17] to form high-melting stable compounds with CaO. However, the improvements made by using these methods are at the expense of reducing the free lime content, which deteriorates the high-temperature property of MgO-CaO refractories. It has been reported that the addition of rare earth oxides can appreciably improve the properties of the MgO-CaO refractories. However, the mechanisms for the improvements, especially the role played in the improvements by the lattice defects generated as a result of the doping of this type of oxides have not been adequately understood. In the present work, the effect of CeO<sub>2</sub> addition on the sintering and microstructure of the MgO-CaO refractories are investigated with an aim to delineate the effects of the lattice defects on improving the sintering and hydration resistance of MgO-CaO refractories.

## 2. Experimental Procedures

**2.1. Raw Materials.** In all the experiments, analytical reagent chemicals of Mg(OH)<sub>2</sub>, Ca(OH)<sub>2</sub>, and CeO<sub>2</sub> are used as raw materials. Powders of appropriate amounts of Mg(OH)<sub>2</sub> and

$\text{Ca(OH)}_2$  were weighed ( $m_{\text{MgO}} : m_{\text{CaO}} = 8 : 2$ ) into a ceramic pot, then mixed in a planetary ball mill for 2 h at a speed of 180 r/min; the ball-to-powder weight ratio used was 3 : 1. The mixtures obtained were then light-roasted in a muffle furnace at 800°C for 30 min to obtain the MgO-CaO powders. 0-1 wt% of the  $\text{CeO}_2$  powder was then dry-mixed with the light-roasted MgO-CaO powder. The mixture was then pressed to cylindrical samples of 20 mm in diameter and 20 mm in length under a pressure of 150 MPa. The samples were heated in an electric furnace at a rate of 3°C/min to 1650°C and kept for 3 h, followed by cooling to room temperature in the furnace.

**2.2. Characterization of MgO-CaO Materials.** The sintered samples were characterized by bulk density and apparent porosity measurements, microstructure, and phase composition analyses. The bulk density and apparent porosity were measured by Archimedes' principle using kerosene as an immersion medium under vacuum. The microstructure was analyzed by scanning electron microscopy (SEM, 20 kv). Phase compositions were determined by X-Ray powder diffraction (XRD, Cu target, 40 kv and 40 mA).

### 3. Results and Discussion

**3.1. Densification.** Figure 1 shows the effect of  $\text{CeO}_2$  addition on bulk density and apparent porosity of the samples sintered at 1650°C for 3 h. It is observed that the bulk density increased gradually and the apparent porosity decreased with the addition of  $\text{CeO}_2$ . The bulk density increased to 3.35 g/cm<sup>3</sup> when the amount of  $\text{CeO}_2$  added increased to 0.75 wt%. With further addition of  $\text{CeO}_2$ , however, the bulk density slightly decreased. These results indicate that adding small amounts of  $\text{CeO}_2$  promoted the sintering and densification of MgO-CaO materials, but this enhancing effect reaches a maximum and starts to decrease when the amount of  $\text{CeO}_2$  exceeds a certain level.

**3.2. XRD Analysis.** Figure 2 shows the XRD patterns of samples with and without  $\text{CeO}_2$  additions. Periclase and lime were the main crystalline phases in all the samples. However, the intensity of diffraction peaks was higher for the samples with  $\text{CeO}_2$  additions than for the sample without  $\text{CeO}_2$  addition, indicating that  $\text{CeO}_2$  promoted the growth of MgO and CaO grains, especially for the sample with 0.5 wt%  $\text{CeO}_2$  added. The position of the diffraction peaks attributable to the CaO (2 2 2) crystallographic was shifted as a result of adding  $\text{CeO}_2$ , suggesting that  $\text{Ce}^{4+}$  entered into the CaO lattice, changing the lattice parameter of CaO. However, no apparent change in the positions of MgO diffraction peaks was detected.

The CaO lattice constant of the samples was determined (Table 1) by comparing the peak positions ( $2\theta$ ) of the XRD patterns using the least square method.

The lattice constant of CaO in the samples without  $\text{CeO}_2$  addition was found to be 4.7978 Å, which was in accordance with the lattice constants of pure CaO. Adding  $\text{CeO}_2$  increased the lattice constant of CaO. When the amount of

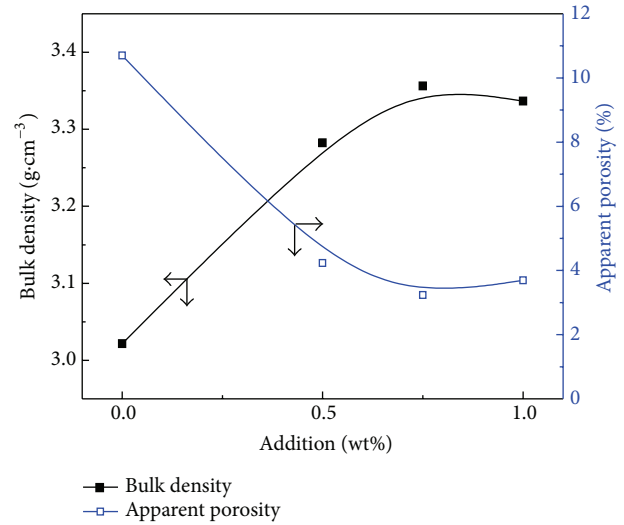


FIGURE 1: Effect of  $\text{CeO}_2$  addition on bulk density and apparent porosity of samples.

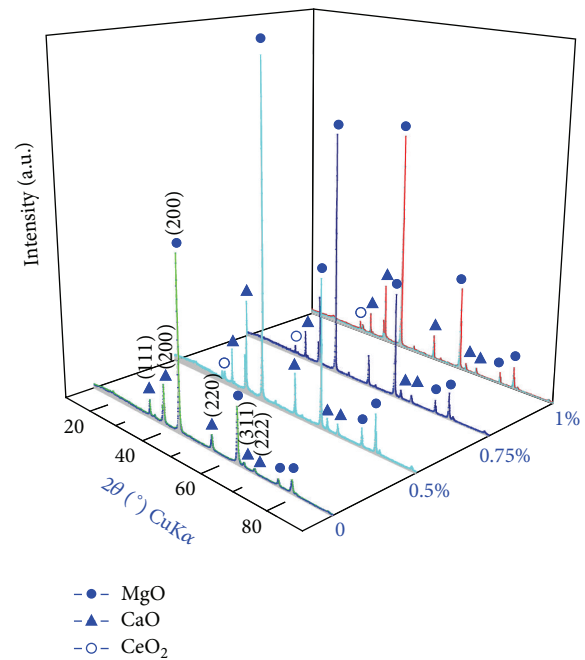


FIGURE 2: XRD patterns of pure and doped MgO-CaO samples.

$\text{CeO}_2$  added was 0.5 wt%, the lattice constant of CaO reached the highest point at  $a_{\text{CaO}} = 4.8232$  Å. The lattice constants of CaO decreased with the further increase in  $\text{CeO}_2$  content, but they were never below the value of the samples without  $\text{CeO}_2$  addition.

Generally, the solid solution of metal oxides forms mainly by the replacement of positive ions in the solvent. Radius of positive ions directly affects the binding energy of positive and negative ions in ionic crystals and hence influences the solid solubility. When the difference in the radius of positive ions is less than 15%, it is easy to form a solid solution; when the difference is larger than 30%, it is not possible to form a

TABLE 1: Calculated lattice constant for sintered samples.

Sample	Parameters	$(h\ k\ l)$					$a$ (Å)
		(1 1 1)	(2 0 0)	(2 2 0)	(3 1 1)	(2 2 2)	
0% CeO <sub>2</sub>	$2\theta$ (°)	32.33	37.51	54.09	64.35	67.70	4.7978
	$d$ (Å)	2.7681	2.3981	1.6960	1.4471	1.3853	
0.5 wt% CeO <sub>2</sub>	$2\theta$ (°)	32.34	37.50	54.04	64.36	67.54	4.8232
	$d$ (Å)	2.7661	2.3966	1.6961	1.4468	1.3854	
0.75 wt% CeO <sub>2</sub>	$2\theta$ (°)	32.37	37.52	54.07	64.36	67.60	4.8223
	$d$ (Å)	2.7630	2.3942	1.6953	1.4463	1.3850	
1 wt% CeO <sub>2</sub>	$2\theta$ (°)	32.34	37.52	54.05	64.34	67.62	4.8161
	$d$ (Å)	2.7655	2.3961	1.6960	1.4468	1.3852	

solid solution. In this study, the difference in radius between Ca<sup>2+</sup> (0.099 nm) and Ce<sup>4+</sup> (0.097 nm) was about 2.0%, but the difference in radius between Mg<sup>2+</sup> (0.072 nm) and Ce<sup>4+</sup> was nearly 26%. Therefore, CeO<sub>2</sub> is expected to dissolve easily in CaO but not in MgO, which is confirmed by the results of XRD analysis.

**3.3. SEM Analysis.** Figure 3 shows the typical microstructure of the fracture surfaces of samples containing various amounts of CeO<sub>2</sub>.

The sintered sample without CeO<sub>2</sub> addition has more pores and the grains in it were smaller in size compared with the samples with CeO<sub>2</sub> additions. Hence, adding CeO<sub>2</sub> increased the degree of sintering and densification and facilitated grain growth. MgO (dark gray) grains grew more rapidly than CaO (light gray) grains due to the fact that the periclase was the continuous phase surrounding lime and as such the growth of the isolated grains of CaO was hindered by the difficulty for Ca<sup>2+</sup> to diffuse across the matrix during the sintering process. It can be seen that the number of pores decreased progressively as the CeO<sub>2</sub> content was increased to 0.75 wt%, but the number increased with further increase in CeO<sub>2</sub> content to 1 wt%, which is consistent with the results of Figure 1.

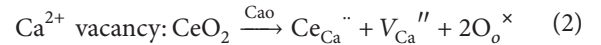
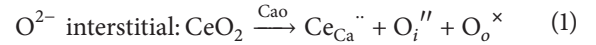
It can be also noted that pores were present at the boundaries between MgO and CaO grains or within the MgO grains; in all the samples no pores were observed within the CaO grains.

The number of pores at grain boundaries will decrease during the sintering process as a result of grain boundary migration, leading to the formation of bigger pores on crystal surface, which may be eliminated as the sintering process progresses. But with the introduction of CeO<sub>2</sub>, the number and size of pores in the MgO grains gradually increased, as the amount of CeO<sub>2</sub> doping was increased. This cannot be attributed to the pore evolution in grains, but it may be due to the formation of Schottky lattice defects, which increased the oxygen vacancy concentration in the high-temperature sintering process. With the increasing of additions, the concentration of lattice defects increases and the vacancy formation energy decreases. As a consequence, the oxygen vacancies diffuse, accumulate, and condense to form pores in the grains in the crystal boundary-migration process [18]. Since the pores in the grains can only be eliminated by lattice

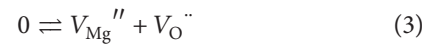
migration, which is much slower than the crystal boundary migration, it is difficult to eliminate the pores in MgO grains.

**3.4. Effect of Defect Reaction by CeO<sub>2</sub> Doping.** CaO and MgO belong to the cubic system, as it is shown in Figure 4(a).

Figure 4(b) shows the crystal structure doped with CeO<sub>2</sub>. When CeO<sub>2</sub> dissolved into CaO, as the valence of Ce<sup>4+</sup> is higher than that of Ca<sup>2+</sup> it may cause two kinds of defect reactions as follows:



Solid solution reactions in (1) and (2) comply with the law of conservation of mass and charge. The number of negative ions brought in by CeO<sub>2</sub> doping (O<sup>2-</sup> : Ce<sup>4+</sup> = 2 : 1) is more than that of CaO (O<sup>2-</sup> : Ca<sup>2+</sup> = 1 : 1) causing the surplus of negative ions and the shortage of positive ions. In order to maintain the electroneutrality, additional cation vacancy must be generated when Ce<sup>4+</sup> dissolves in the CaO phase. Hence, Ca<sup>2+</sup> vacancy in (2) is the prior modality of charge compensation while defects in MgO grains mainly come from heat-activation Schottky lattice defects as follows:



Generally, vacancies in the grains are surrounded by atoms, but atoms are not necessarily surrounded by vacancies. As a result, it is easy for vacancies to diffuse but it is difficult for atoms to diffuse. MgO-CaO materials doped with CeO<sub>2</sub> enlarge the vacancy concentration of Ca<sup>2+</sup>. Owing to high symmetry of CaO crystal structure, the migration energy of Ca<sup>2+</sup> vacancy is the same in the six neighboring directions (Figure 4(c)) and migration towards any direction may occur, which contributes to the Ca<sup>2+</sup> diffusion. According to the defect reaction, prior modality of charge compensation in CaO lattice is the vacancy of positive ions, so, no pores occur in the sintering CaO grains while O<sup>2-</sup> vacancy in MgO grains forms pores in grains.

## 4. Conclusions

- (1) The lattice constant of CaO in MgO-CaO materials increases with the addition of CeO<sub>2</sub>, when the amount

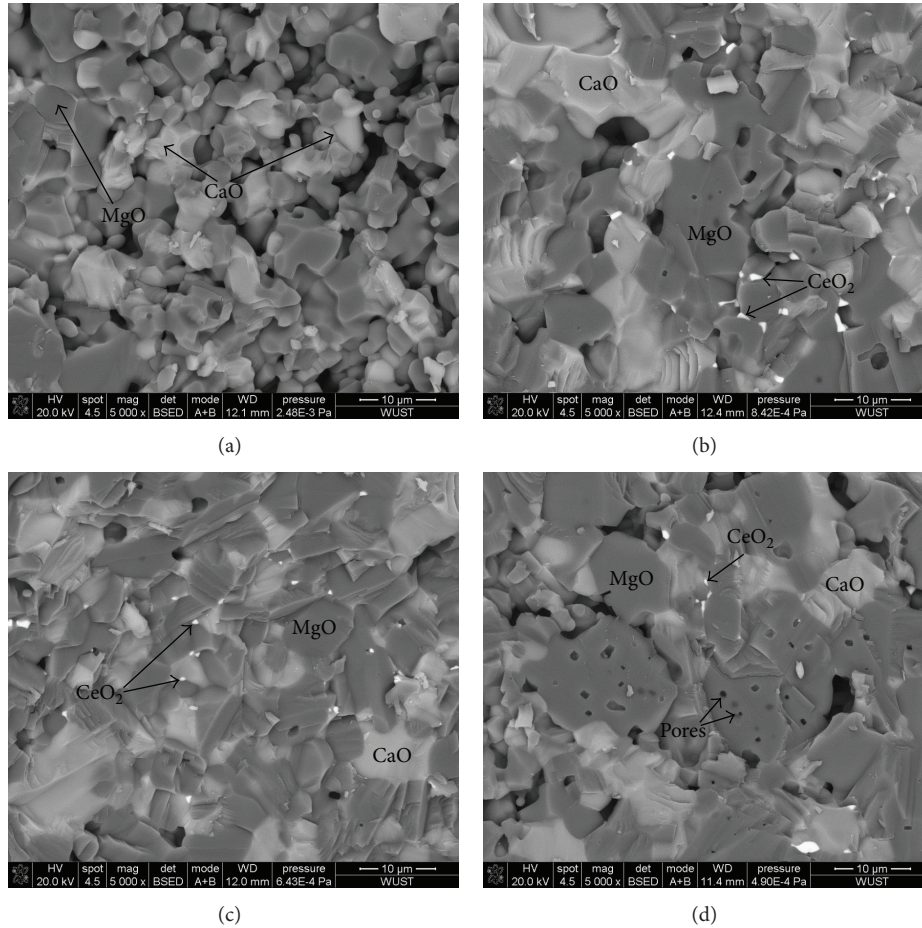


FIGURE 3: SEM images of samples: (a) 0%, (b) 0.5 wt%, (c) 0.75 wt%, and (d) 1 wt%.

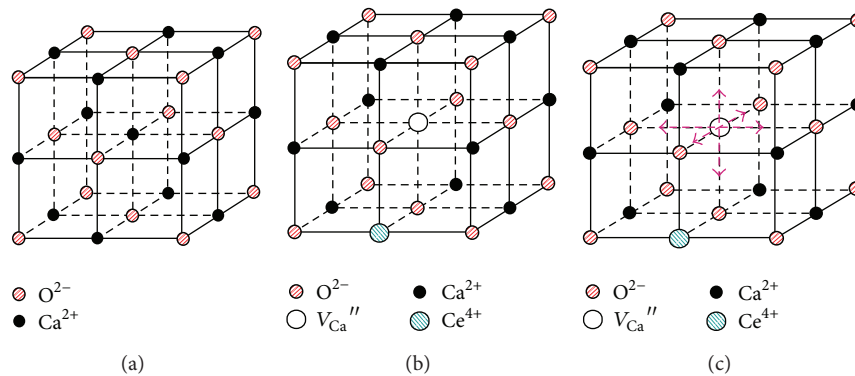


FIGURE 4: Schematic diagram for Crystal structure of CaO. (a) Crystal structure of CaO, (b) crystal structure of CaO doped with CeO<sub>2</sub>, and (c) schematic diagram for vacancy migration of Ca<sup>2+</sup>.

of addition exceeds 0.5 wt%, the lattice constant starts to decrease.

- (2) The addition of CeO<sub>2</sub> increases the vacancy concentration of Ca<sup>2+</sup> and accelerates the diffusion of Ca<sup>2+</sup>, contributing to the sintering densification of materials. Many pores are formed in the grains of MgO, which mainly originated from the Schottky lattice

defects and oxygen vacancy aggregation when the grain boundaries migrate during high-temperature sintering.

### Acknowledgment

This work was supported by the Natural Science Foundation of China (Grant no. 50774057).

## References

- [1] W. E. Lee and R. E. Moore, "Evolution of in situ refractories in the 20th century," *Journal of the American Ceramic Society*, vol. 81, no. 6, pp. 1385–1410, 1998.
- [2] Z. Q. Guo, S. Palco, and M. Rigaud, "Bonding of cement clinker onto dolomite-based refractories," *Journal of the American Ceramic Society*, vol. 88, no. 6, pp. 1481–1487, 2005.
- [3] Z. Li, S. Zhang, and W. E. Lee, "Improving the hydration resistance of lime-based refractory materials," *International Materials Reviews*, vol. 53, no. 1, pp. 1–20, 2008.
- [4] M. Rabah and E. M. M. Ewais, "Multi-impregnating pitch-bonded Egyptian dolomite refractory brick for application in ladle furnaces," *Ceramics International*, vol. 35, no. 2, pp. 813–819, 2009.
- [5] Y. W. Wei and N. Li, "Refractories for clean steel making," *American Ceramic Society Bulletin*, vol. 81, no. 5, pp. 32–35, 2002.
- [6] X. Zhong, "Looking ahead-a new generation of high performance refractory ceramics," *Naihuo Cailiao*, vol. 37, no. 1, pp. 1–10, 2003.
- [7] L. N. Zhong, B. L. Wu, J. G. Song et al., "Recycling refractory waste," *Journal of Functional Materials*, vol. 35, supplement, pp. 2615–2618, 2004.
- [8] W. Meyer, A. Franchi, G. Buchebner, and M. Willingshofer, "The use of dolomite-carbon-lined ladles for the production of superclean steels," *Veitsch-Radex Rundschau*, vol. 1998, no. 2, pp. 32–44, 1998.
- [9] N. M. Ghoneim, M. A. Mandour, and M. A. Serry, "Phase composition, microstructure and properties of sintered  $\text{La}_2\text{O}_3$ -doped lime and dolomite grains," *Ceramics International*, vol. 16, no. 4, pp. 215–223, 1990.
- [10] A. Ghosh and H. S. Tripathi, "Sintering behaviour and hydration resistance of reactive dolomite," *Ceramics International*, vol. 38, no. 2, pp. 1315–1318, 2012.
- [11] M. Chen, N. Wang, J. Yu, and A. Yamaguchi, "Effect of porosity on carbonation and hydration resistance of CaO materials," *Journal of the European Ceramic Society*, vol. 27, no. 4, pp. 1953–1959, 2007.
- [12] A. Ghosh, T. K. Bhattacharya, B. Mukherjee, and S. K. Das, "Effect of CuO addition on the sintering of lime," *Ceramics International*, vol. 27, no. 2, pp. 201–204, 2001.
- [13] H. A. Yeprem, "Effect of iron oxide addition on the hydration resistance and bulk density of dolomite," *Journal of the European Ceramic Society*, vol. 27, no. 2-3, pp. 1651–1655, 2007.
- [14] É. Makó, "The effect of quartz content on the mechanical activation of dolomite," *Journal of the European Ceramic Society*, vol. 27, no. 2-3, pp. 535–540, 2007.
- [15] J. L. Rodríguez, M. A. Rodríguez, S. De Aza, and P. Pena, "Reaction sintering of zircon-dolomite mixtures," *Journal of the European Ceramic Society*, vol. 21, no. 3, pp. 343–354, 2001.
- [16] J. Xue, J. H. Tinkler, and R. Dieckmann, "Influence of impurities on the oxygen activity-dependent variation of the oxygen content of a commercial, CaO-doped  $\text{ZrO}_2$ ," *Solid State Ionics*, vol. 166, no. 1-2, pp. 199–205, 2004.
- [17] M. Chen, C. Lu, and J. Yu, "Improvement in performance of MgO-CaO refractories by addition of nano-sized  $\text{ZrO}_2$ ," *Journal of the European Ceramic Society*, vol. 27, no. 16, pp. 4633–4638, 2007.
- [18] J.-K. Yan, G.-Y. Gan, J. Yuan, J.-H. Du, and J.-H. Yi, "Defect chemistry and formation mechanism of pores in undoped  $\text{TiO}_2$  ceramics," *Chinese Journal of Nonferrous Metals*, vol. 21, no. 6, pp. 1380–1388, 2011.